

Xiahui Zeng

Modeling hardening and softening due to high-angle grain boundaries in crystalline solids

(Zur Modellierung von Härtung und Entfestigung durch Großwinkelkorngrenzen in kristallinen Stoffen)



CUVILLIER VERLAG

Xiaohui Zeng

Modeling hardening and softening due to high-angle grain
boundaries in crystalline solids

(Zur Modellierung von Härtung und Entfestigung durch
Großwinkelkorn Grenzen in kristallinen Stoffen)



Cuvillier Verlag Göttingen

Bibliografische Information Der Deutschen Bibliothek

Die Deutsche Bibliothek verzeichnet diese Publikation in der Deutschen Nationalbibliografie; detaillierte bibliografische Daten sind im Internet über <http://dnb.ddb.de> abrufbar.

1. Aufl. - Göttingen : Cuvillier, 2007

Zugl.: (TU) Erlangen-Nürnberg, Univ., Diss., 2007

978-3-86727-XXX-X

© CUVILLIER VERLAG, Göttingen 2007

Nonnenstieg 8, 37075 Göttingen

Telefon: 0551-54724-0

Telefax: 0551-54724-21

www.cuvillier.de

Alle Rechte vorbehalten. Ohne ausdrückliche Genehmigung des Verlages ist es nicht gestattet, das Buch oder Teile daraus auf fotomechanischem Weg (Fotokopie, Mikrokopie) zu vervielfältigen.

1. Auflage, 2007

Gedruckt auf säurefreiem Papier

978-3-86727-XXX-X

**Modeling hardening and softening due to high-angle grain
boundaries in crystalline solids**
(Zur Modellierung von Härtung und Entfestigung durch
Großwinkelkorngrenzen in kristallinen Stoffen)

Der Technischen Fakultät der
Universität Erlangen-Nürnberg

zur Erlangung des Grades

DOKTOR-INGENIEUR

vorgelegt von

Xiaohui Zeng

Erlangen - 2007

Als Dissertation genehmigt von
der Technischen Fakultät der
Universität Erlangen-Nürnberg

Tag der Einreichung: 18. September 2006
Tag der Promotion: 13. Februar 2007
Dekan: Prof. Dr.-Ing. A. Leipertz
Berichterstatter: Prof. Dr.-Ing. W. Blum
Prof. Dr.-Ing. H.J. Maier

Contents

symbols	v
Einführung	ix
1 Introduction	1
1.1 Phenomena of grain boundary hardening and softening	2
1.1.1 Grain boundary hardening at low homologous temperature	3
1.1.2 Grain boundary softening at elevated homologous temperature	3
1.2 Review on deformation mechanisms for grain boundary hardening and softening	4
1.2.1 Hall-Petch relation and explanation	5
1.2.2 Grain boundary softening and explanation	7
1.3 Scope of the current work	8
2 Model	11
2.1 Basic considerations	12
2.1.1 Microstructure of coarse-grained and ultrafine-grained material	12
2.1.2 Assumptions and microstructure parametrization	13
2.2 Evolution of microstructure	20
2.2.1 Generation of dislocations	20
2.2.2 Annihilation of dislocations	26
2.3 Kinetics of dislocation glide	31
2.3.1 Mobile dislocation density	31
2.3.2 Average glide velocity	31
2.4 Numerical implementation	32
3 Results	35
3.1 Parameter set and initial microstructural state	36
3.1.1 Material and model parameters	36
3.1.2 Integration conditions	37
3.2 Evolution of deformation resistance and microstructure with strain	37
3.3 Steady state deformation resistance	44
3.3.1 Deformation resistance	44
3.3.2 Stress components: ratio σ^*/σ	46
3.3.3 Dislocation density	47
3.3.4 Annihilation mechanism of grain boundary dislocations	49
3.4 Grain-size dependence of steady steady deformation resistance	51

3.4.1	Low temperature	51
3.4.2	High temperature	54
3.5	Simplified steady state solution for ufg materials	55
3.5.1	Hall-Petch relation at low homologous temperature	56
3.5.2	Grain boundary softening at elevated homologous temperature	56
3.6	Comparison with experimental observations	57
4	Discussion	61
4.1	Dislocation structure at grain boundaries	62
4.2	An alternative mechanism of annihilation of grain boundary dislocations	63
4.2.1	Concept of lateral climb of dislocation dipole	63
4.2.2	Rate of annihilation by lateral climb	65
4.2.3	Comparison between mutual climb and lateral climb	66
4.3	Deformation due to high-angle grain boundaries in ufg Cu	68
4.4	Density of mobile dislocations	70
5	Summary	73
5.1	English	74
5.2	German	75
	Figures	78
	Tables	83
	Bibliography	85
A	Appendix	93
A.1	Average radius of grain sections	94
A.2	Generation rate of dislocations in grain interiors	96
A.3	Storage rate of dislocations at grain boundaries	98
A.4	Climb velocity of grain boundary dislocations	101
	Acknowledgments	105
	Curriculum vitae	107

Inhalt

symbole	v
	ix
1 Einleitung	1
1.1 Phänomene der Verfestigung und Entfestigung durch Großwinkel-Korngrenzen	2
1.1.1 Verfestigung durch Korngrenze bei geringer homologer Temperatur	3
1.1.2 Entfestigung durch Korngrenze bei hoher homologer Temperatur . .	3
1.2 Literaturstand zu Ver- und Entfestigung durch Großwinkel-Korngrenzen .	5
1.2.1 Hall-Petch Beziehung	5
1.2.2 Entfestigung durch Korngrenze und Erklärung	7
1.3 Zielsetzung der Arbeit	9
2 Modell	11
2.1 Grundüberlegungen	12
2.1.1 Mikrostruktur des grobkörnigen und ultrafeinkörnigen Materials . .	12
2.1.2 Annahmen und Parametrisierung der Mikrostruktur	13
2.2 Evolution der Mikrostruktur	20
2.2.1 Versetzungserzeugung	20
2.2.2 Versetzungsannihilation	26
2.3 Kinetik der Versetzungsgleitung	31
2.3.1 Dichte der mobilen Versetzungen	31
2.3.2 Mittlere Gleitungsgeschwindigkeit	31
2.4 Numerische Umsetzung	32
3 Ergebnisse	35
3.1 Parametersatz und Zustand der Anfangsmikrostruktur	36
3.1.1 Material- und Modellparameter	36
3.1.2 Randbedingungen der Integration	37
3.2 Evolution des Verformungswiderstands und der Mikrostruktur mit der Dehnung	37
3.3 Stationärer Verformungswiderstand	44
3.3.1 Verformungswiderstand	44
3.3.2 Spannungskomponente: Verhältnis σ^*/σ	46
3.3.3 Versetzungsdichte	47
3.3.4 Annihilationsmechanismen der Versetzungen an der Korngrenze . .	49
3.4 Stationärer Verformungswiderstand in Abhängigkeit von der Korngröße . .	51
3.4.1 Tiefe Temperatur	51

3.4.2	Hohe Temperatur	54
3.5	Vereinfachte stationäre Lösung für ultrafeinkörnige Materialien	55
3.5.1	Hall-Petch Beziehung bei tiefer homologer Temperatur	56
3.5.2	Entfestigung durch Korngrenzen bei erhöhter homologer Temperatur	56
3.6	Vergleich mit experimentellen Beobachtungen	57
4	Diskussion	61
4.1	Versetzungsstruktur an der Großwinkelkorngrenzen	62
4.2	Ein alternativer Annihilationsmechanismus der Versetzungen an der Korngrenze	63
4.2.1	Konzept des lateralen Kletterns von Dipolen	63
4.2.2	Annihilationsgeschwindigkeit durch laterales Klettern	65
4.2.3	Vergleich des gemeinsamen Kletterns mit lateralem Klettern	66
4.3	Verformung durch GroßWinkelkorngrenzen in ultrafeinkörnigem Cu	68
4.4	Dichte der mobilen Versetzungen	70
5	Zusammenfassung	73
5.1	Englisch	74
5.2	Deutsch	75
	Abbildungen	78
	Tabellen	83
	Literatur	85
A	Anhang	93
A.1	Mittlerer Kornradius	94
A.2	Erzeugungsrate von Versetzungen im Korninnern	96
A.3	Depositionsrate von Versetzungen an Korngrenzen	98
A.4	Die Klettergeschwindigkeit der Versetzungen an Korngrenzen	101
	Danksagung	105
	Lebenslauf	107

symbols

symbol description

Δa^*	activation area
α	coefficient of dislocation interaction
b	Burgers vector
c_j	fraction of jogged sites along dislocation
D_{eff}	effective diffusion coefficient
D_{gb}	coefficient of diffusion along grain boundary
D_v	coefficient of volume diffusion
d	grain size
d_{cg}	size of coarse grains
d_{ufg}	size of ultrafine grains
d_{diff}	length of diffusion path
$d_{\text{dip},f}$	average separation of dipoles formed by free dislocations in grain interiors
$d_{\text{dip},\text{gb}}$	average separation of dipoles formed by dislocations at grain boundaries
$d_{\text{spon},f}$	minimum stable height of dipoles formed in grain interiors
$d_{\text{spon},\text{gb}}$	minimum stable height of dipoles formed at grain boundaries
δ	average spacing of free dislocations
δ_{gb}	width of grain boundary
ϵ	plastic strain
ϵ_{el}	elastic strain
ϵ_{mech}	mechanical (elastic + plastic) strain
F_c	force acting on the curved end of dipoles

f_{gb}	adjustable weighting factor grain boundary dislocations
f_{mob}	mobile fraction of single dislocations
f_{h}	volume fraction of hard region
f_{s}	volume fraction of soft region
$f_{\text{v,diff}}$	fraction of volume diffusion
$f_{\text{gb,diff}}$	fraction of grain boundary diffusion
ϕ	angle between the slip plane and the grain boundary surface
G	shear modulus
ΔG_0	total free enthalpy required to surmount an obstacle to dislocation glide
γ	plastic shear strain
$\dot{\gamma}$	plastic shear strain shear
k_{B}	Boltzmann's constant
k_{ρ}	numeric constant
k_{gb}	numeric constant
k_{w}	numeric constant
l_{c}	average length of dipoles
Λ_{ρ}	grain-size independent mean free path of free dislocations
$\Lambda_{\rho,\text{d}}$	grain-size dependent mean free path of free dislocations
λ	average spacing of thermal obstacles to dislocation glide
m	strain rate sensitivity of flow stress
M	Taylor factor
n	sensitivity of stationary strain rate on stress
n_{g}	number of active glide systems
N_{gb}	areal density (length per area) of grain boundary dislocations
ν	Poisson's ratio
ν_{Debye}	Debye frequency
ν_{G}	attack frequency
$\nu_{\text{c,f}}$	frequency of annihilation of free dislocations through climb
$\nu_{\text{c,gb}}$	frequency of annihilation of grain boundary dislocations through climb

Ω	atomic volume
p	probability for a dislocation loop expanding on its slip plane to be stored per dislocation encountered
Q	activation energy
ρ_{dip}	density of dislocations in dipolar configuration
ρ_{f}	density of free dislocations in grain interior
ρ_{gb}	density of dislocations at grain boundaries
ρ_{mob}	density of mobile dislocations
ρ_{tot}	overall density of dislocations
R	gas constant
\bar{r}	average radius of the dislocation loops being stored in grain
r'	radius of average grain section
s_{gb}	average spacing of grain boundary dislocations
σ	applied normal stress
$\sigma_{\text{c,f}}$	attractive stress between dipoles formed by free dislocation in grain interiors
$\sigma_{\text{c,gb}}$	attractive stress between dipoles formed by dislocation at grain boundaries
σ_{G}	athermal stress
σ_{h}	local stress in hard region
σ_{s}	local stress in soft region
σ^*	effective stress
T	absolute temperature
T_{hom}	homologous temperature
T_{m}	melting temperature
t	time
θ_{II}	rate of hardening in stage II of single crystal deformation
V	crystal volume
$v_{\text{c,f}}$	climb velocity of free dislocation
$v_{\text{c,gb}}$	climb velocity of grain boundary dislocation

symbols

v_g	average glide velocity of mobile dislocation segments
w	average subgrain size
w_∞	steady-state average subgrain size
ξ_c	scaling factor
ξ_{dip}	scaling factor
Δx	width of thermal obstacles

cg	coarse-grained
ECAP	equal channel angular pressing
H-P	Hall-Petch
GBS	grain boundary sliding
KWKG	Kleinwinkel-Korngrenzen
nano	nanocrystalline
ODE	ordinary differential equation
SPD	severe plastic deformation
TEM	transmission electron microscope
ufg	ultrafine-grained

Einführung

Polykristalle mit Korngrößen im Submikrometer-Bereich stellen eine aussichtsreiche Materialklasse für strukturelle Anwendungen dar. Insbesondere bei niedriger homologer Temperatur $T_{\text{hom}} = T/T_M$ (mit T : absoluter Temperatur und T_M : Schmelzpunkt) zeigen sie, verglichen mit konventioneller Korngröße (cg), verbesserte mechanische Eigenschaften [1]. Veröffentlichte Festigkeitssteigerungen beziehen sich zum Großteil auf den Beginn plastischer Verformung. Hansen [2] sowie Meyers und Mitarbeiter [3] zeigten, dass die erhöhte Festigkeit entlang der Fließkurve erhalten bleibt. Für Rein-Cu (OFHC) stellten Blum *et al.* [4] die jeweils bei Raumtemperatur in Druckversuchen gemessene Fließspannung und mittels Nanoindentierung gemessene Härte für den Korngrößenbereich $0.10 \mu\text{m} \leq d \leq 50 \mu\text{m}$ zusammen. Die Daten zeigen, dass eine Hall-Petch Beziehung sogar für bzw. nahe am Zustand stationärer Verformung gilt, d.h. die Fließspannung und Härte nimmt mit abnehmender Korngröße zu. Somit verfestigen Großwinkl-Korngrenzen dieses Material bei Raumtemperatur. Allerdings findet sich für hochverformtes Cu mit ultrafeinen Körnern der Größe $0.35 \mu\text{m}$ bei erhöhter Temperatur und/oder geringen Dehnraten, dass die stationäre Fließspannung unter derjenigen bei konventioneller Korngröße liegt [5–8]. Dieses Phänomen wurde durch beschleunigte Versetzungsannihilation an Korngrenzen erklärt [5]. Der Zustand stationärer Verformung – mit gleichbleibender Fließspannung und Dehnraten bei konstanter Temperatur – ist dabei durch ein dynamisches Gleichgewicht der Evolution der Versetzungsstruktur gekennzeichnet.

Man nimmt an, dass Plastizität auch in nanokristallinen Stoffen bis in den Bereich von $d \approx 30 \text{ nm}$ durch die Gleitung von Gitterversetzungen dominiert wird [9]. Ferner wird vermutet, dass der Verformungswiderstand von (ultra)feinkörnigen Materialien stark durch die überproportionale Anreicherung von Versetzungen an Korngrenzen beeinflusst ist [5, 9, 10]. Unter dieser Annahme spielen die Deposition und Annihilation von Korngrenzversetzungen eine entscheidende Rolle. Ersteres erzeugt eine Festigkeitssteigerung während Letzteres eine entfestigende Tendenz erklären kann. Zur Zeit existiert noch kein schlüssiges Modell, welches auf Basis von Ratengleichungen für die Erzeugung und Vernichtung von Korngrenzversetzungen die beobachteten Phänomene einer durch hohen Anteil von Großwinkel-Korngrenzen verursachte Ver- und Entfestigung zu erklären vermag. In der vorliegenden Arbeit wird versucht ein einfaches statistisches Versetzungsmodell zu entwickeln, das in der Lage ist die entscheidenden Einflüsse der Korngröße auf den stationären Verformungswiderstand wiederzugeben. Die Ableitung von Mechanismen zur Versetzungsstrukturevolution steht dabei im Vordergrund.

Am Beispiel von Cu mit Korngrößen $0.10 \mu\text{m} \leq d \leq 100 \mu\text{m}$ werden ausführliche Simulationen des Modells durchgeführt. Der resultierende stationäre Verformungswiderstand

wird unter zwei Gesichtspunkten analysiert. Zum Einen wird dessen Abhängigkeit von Dehnrates und Temperatur für eine Reihe fester Korngrößen untersucht. Zum Anderen der Einfluss der Korngröße bei gegebenen Verformungsbedingungen studiert. Anhand des Vergleichs mit experimentellen Ergebnissen wird das Modell kritisch diskutiert.

1 Introduction

Contents

1.1	Phenomena of grain boundary hardening and softening . . .	2
1.1.1	Grain boundary hardening at low homologous temperature . . .	3
1.1.2	Grain boundary softening at elevated homologous temperature .	3
1.2	Review on deformation mechanisms for grain boundary hardening and softening	4
1.2.1	Hall-Petch relation and explanation	5
1.2.1.1	Pile up theories	5
1.2.1.2	Work hardening theories	6
1.2.1.3	Grain boundary source theories	7
1.2.2	Grain boundary softening and explanation	7
1.2.2.1	Grain boundary sliding and grain boundary diffusional creep	7
1.2.2.2	Annihilation of dislocations at grain boundaries	8
1.3	Scope of the current work	8

From the point of view of structural application, the continuing scientific interest in polycrystalline materials with grain sizes from sub-micron to nanometer is mainly due to their improved mechanical behavior, especially at low homologous temperatures $T_{\text{hom}} = T/T_M$ (where T and T_M are (absolute) temperature and melting temperature, respectively), compared to material of conventional grain size (cg) [1]. To a large extent, reported strengthening concerns the onset of plasticity. Hansen [2] and Meyers *et al.* [3] pointed out that such improved mechanical behavior also holds beyond plastic yielding [2, 3]. Recently, for pure Cu¹ of various grain sizes $10 \text{ nm} \leq d \leq 50 \text{ }\mu\text{m}$ the flow stress from uniaxial compression and the hardness from nanoindentation at ambient temperature were compiled [4]. These data indicate that a Hall-Petch relation holds at room temperature even near or in the steady state of deformation, *i.e.*, flow stress increases with decreasing grain size. That suggests that the material is hardened by high-angle grain boundaries at ambient temperature. However, at elevated temperatures and/or low strain rates, for severely plastically deformed Cu with ultrafine grains of $0.35 \text{ }\mu\text{m}$, the steady state flow stress becomes smaller than that of cg material [5–8]. This phenomenon has been attributed to fast dislocation annihilation within high-angle grain boundaries, meaning that high-angle grain boundaries soften the material at elevated temperatures [5]. The term steady state deformation is defined as the state of dynamic equilibrium of the dislocation structure consisting of free dislocations (not incorporated in dislocation networks constituting low-angle grain boundaries) and low-angle boundaries, where both flow stress σ and strain rate $\dot{\epsilon}$ do not change any more with strain ϵ at constant temperature T . In the present work, attempts will be made on microstructural basis to model the role of high-angle grain boundaries in the deformation of pure Cu in a wide range of grain sizes and temperatures.

In this section we shall start with demonstrating the phenomena of grain boundary hardening as well as softening found in Cu with grain size range of $0.01 < d/\mu\text{m} < 50$ in the interval $298 \leq T/\text{K} \leq 470$ corresponding to $0.22 \leq T_{\text{hom}} \leq 0.35$. The deformation mechanisms of relevance will be briefly reviewed in section 1.2. The detailed scope of the current work will be presented in section 1.3.

1.1 Phenomena of grain boundary hardening and softening

Figure 1.1 combines published data of the maximum deformation resistances (maximum stress σ at constant strain rate $\dot{\epsilon}$ and minimum $\dot{\epsilon}$ at constant σ) of Cu of different initial grain sizes in a wide range of temperatures and strain rates [4]. The normalization of the ordinate was done as proposed by Kocks and Mecking [11] by $k_B T / (G b^3) \ln(\dot{\epsilon}/\dot{\epsilon}_0)$, where k_B is Boltzmann constant, G is the shear modulus, b is the length of Burgers vector, and $\dot{\epsilon}_0 = 10^7 \text{ s}^{-1}$. The values of G and b were taken from [12] (also see Table 3.1). This normalization successfully serves the purpose to combine data measured at different temperatures in a narrow band. Grain size varies over a large range from $0.01 \text{ }\mu\text{m}$ up

¹oxygen-free high-conductivity grade

to the dimensions of the single crystalline specimen. The circles stem from tests on bulk specimens with conventional grain size of 50 μm and ultrafine grain (ufg) size of 0.35 μm [13]. The ufg material originally came from the same batch as the cg one and achieved its fine structure by SPD through 12 passes of equal channel angular pressing (ECAP) on route C at room temperature. The tests were performed in uniaxial compression in a temperature range extending from ambient temperature up to $T_{\text{hom}} = 0.33$. For details it is referred to [5, 8]. The triangles stem from hardness H measured in nanoindentation at ambient temperature (see [14]). The materials with small sizes subjected to nanoindentation were prepared in several ways, such as magnetron sputtering ($d \leq 0.031 \mu\text{m}$), mechanical attrition ($d = 0.042 \mu\text{m}$) and ECAP ($d = 0.19 \mu\text{m}$) (see [14] for details). The flow stresses were calculated as $\sigma = H/3$ from the hardnesses H [4].

1.1.1 Grain boundary hardening at low homologous temperature

Comparison of the data from nanoindentation to uniaxial compression tests at a normalized strain rate of about -0.13 shows that the flow stress increases significantly with decreasing d (see Fig. 1.1)². Fig. 1.2 shows the room temperature data from Fig. 1.1 as function of $d^{-0.5}$. Within scatter the data for room temperature are well described by a straight line in agreement with the Hall-Petch relation:

$$\sigma = \sigma_0 + k_{\text{HP}} d^{-0.5}, \quad (1.1)$$

where σ_0 is the overall resistance of the crystal lattice to dislocation movement and k_{HP} represents the relative hardening contribution of the grain boundaries.

1.1.2 Grain boundary softening at elevated homologous temperature

For elevated temperature of 418 K, the trend is reversed in Fig. 1.2 compared to room temperature, as the maximum flow stress decreases with decreasing d . This decrease is related with increase of the strain rate sensitivity $m = d \log \sigma / d \log \dot{\epsilon}$ observed to occur for ufg Cu in Fig. 1.1. The significant difference in strain rate sensitivities causes a crossover in the saturation stresses of ufg and cg Cu at a normalized strain rate of 0.17. This means that ufg Cu becomes softer than the cg variant for normalized strain rates < -0.17 (see Fig. 1.1). There is thus a transition from hardening at low T_{hom} and high strain rate $\dot{\epsilon}$ to softening at elevated T_{hom} and low $\dot{\epsilon}$ in ufg Cu compared to cg Cu. Note that the softening relates to the steady state of deformation, but not to the yield stress which is lower for cg Cu compared to ufg Cu even at elevated temperatures [8].

Breakdown of the Hall-Petch relation has frequently been reported to occur even at low temperature, where yield stress decreases with grain refinement once the grain size is

²The fact that the flow stresses for $d = 50 \mu\text{m}$ are distinctly higher than those for $d = 23 \mu\text{m}$ is not unexpected, as in the first case stresses have been extrapolated to be the steady-state stresses corresponding to $\epsilon \approx 2$ [15] from the values measured at $\epsilon \approx 0.35$, while in the latter case the stresses were measured only at about $\epsilon \approx 0.15$.

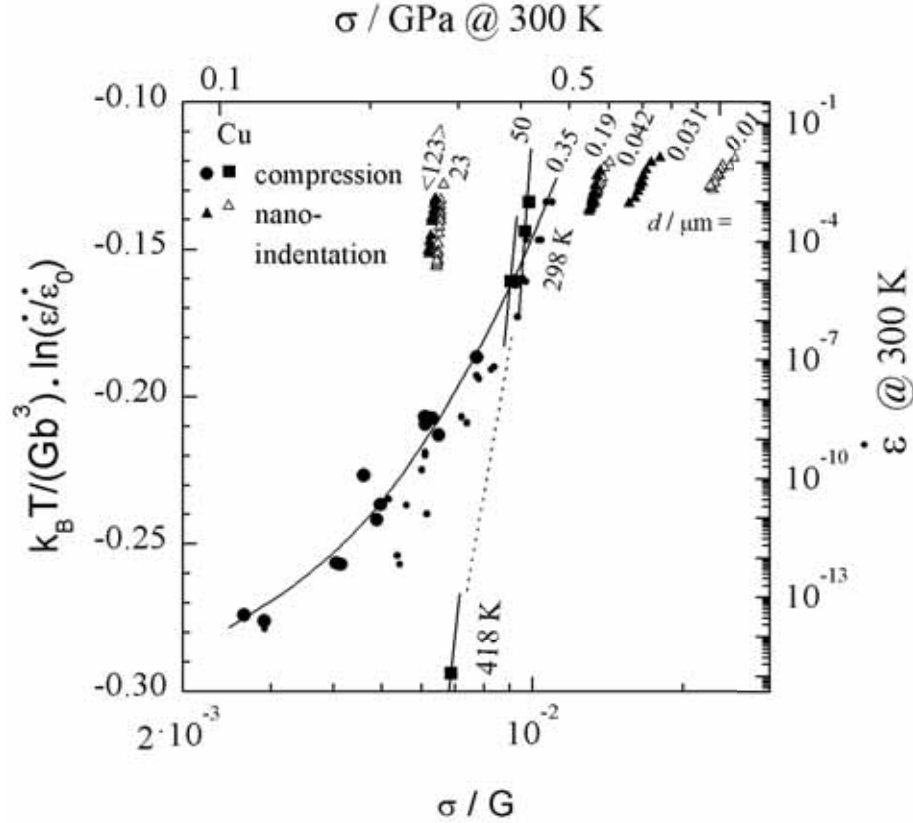


Figure 1.1: Temperature normalized strain rate as function of shear modulus normalized flow stress for Cu with different grain sizes d and a $\langle 123 \rangle$ -oriented Cu single crystal from nanoindentation at ambient temperature ($T_{\text{hom}} = 0.22$) [4, 14] and uniaxial compression from room temperature up to 448 K ($T_{\text{hom}} = 0.35$) [5, 8, 15]. Large symbols: saturation stress (or steady-state deformation resistances); small symbols: maximum deformation resistance (the flow stress or creep rate measured at the end of a test). Right ordinate axis: strain rate at 300 K.

reduced below a critical value [16–20]. However, as stated by Meyers *et al.* in their recent review paper, "Though researchers have debated the existence of the negative Hall Petch effect, there is insufficient information to validate the existence of this effect" [1].

1.2 Review on deformation mechanisms for grain boundary hardening and softening

This section briefly reviews some relevant deformation mechanisms responsible for hardening/softening by grain boundaries.

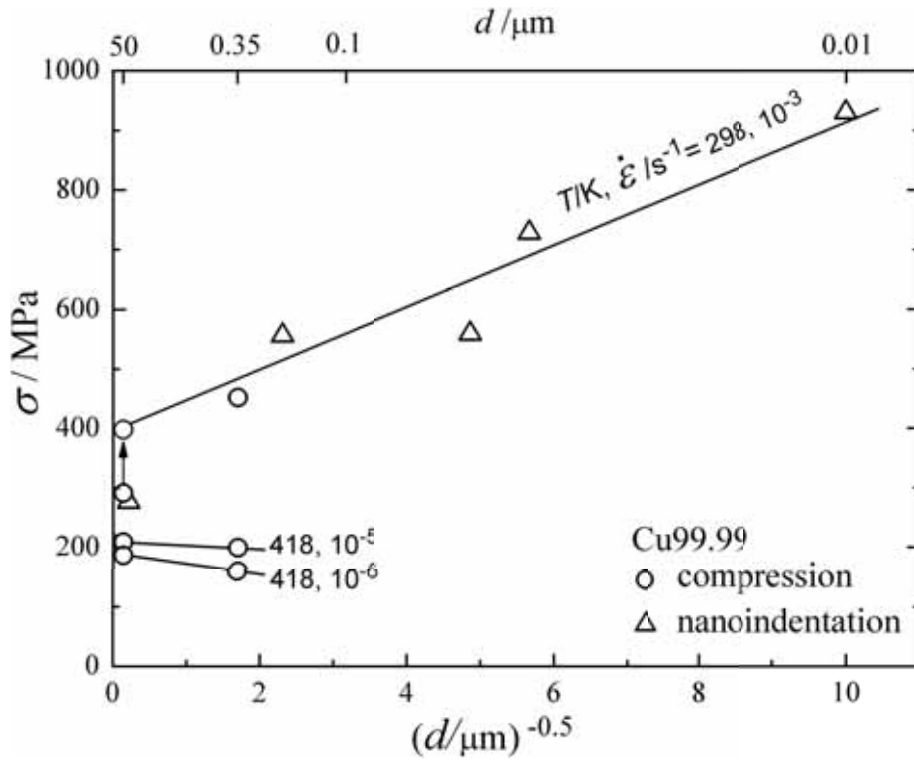


Figure 1.2: Variation of flow stress with inverse square root of grain size d with different T and $\dot{\epsilon}$. The arrow pointing to the saturated flow stress (400 ± 50) MPa of cg Cu with $d = 50 \mu\text{m}$ [4]. Data from Fig. 1.1.

1.2.1 Hall-Petch relation and explanation

As stated above, the Hall-Petch relation (1.1) describes not only the yield stress, but also the flow stresses beyond plastic yielding and the hardnesses derived from indentation testing [2–4]. Many theoretical studies have been conducted to understand this relation [21–26]. In the following some of them will be briefly reviewed.

1.2.1.1 Pile up theories

The original mechanism proposed by Hall [21] and Petch [22] involves a pile-up of dislocations against grain boundaries. The grain boundaries act as obstacles, hindering the dislocation glide along the slip planes. When subsequent dislocations move along the same slip plane, the dislocations pile up at the grain boundaries. The dislocations repel each other, so that the stress on the grain boundary increases with increasing number of dislocations in the pile-up. If there are n dislocations in the pile-up, the stress at the grain boundary will be $n\sigma$ where σ is applied stress. In order to propagate the plastic deformation, dislocations are needed to be emitted into the neighboring grain. If the critical stress required at a grain boundary for the emission of a dislocation is σ_c , then there needs to be a stress of σ_c/n applied to the sample. In a larger grain there will be more dislocations within the grain, so there will be more dislocations in the pile-up. Therefore

a lower applied stress is required to produce a local stress which is sufficiently large to cause emissions of dislocations.

Many researchers have theoretically studied various kinds of pile-ups. These include single-layer single-ended pileups in homogeneous, heterogeneous, and anisotropic media, single-layer double-ended pileups, circular pileups, and multiple-layer pileups. Excellent reviews were presented by Li and Chou [26] and Hirth and Lothe [27].

Several considerations stemming from experimental observations lead one to question the general applicability of the pile-up theories. The first is the lack of direct observation of pile-ups in pure metals. Secondly, Worthington and Smith [28] found that in Fe-3%Si, dislocations are emitted from grain boundaries at stresses much below the yield stress without the help of pile-ups and that these stresses do not seem to depend on grain size. According to the pile-up model, the function of the pile-up is to create a stress concentration at the grain boundary to activate dislocation sources. If these dislocation sources can be activated without a pile-up and at stresses below the yield stress, the necessity for pile-ups is no longer existing. Also, as the number of pile-up dislocations is reduced with grain size, the multiplication effect is lost when the dislocation spacing becomes comparable to the grain size in the nanocrystalline (nano) regime.

Motivated by these considerations, theories without the use of pile-ups have been proposed, *e.g.*, work hardening theories, grain boundary source theories and a theory based on geometrically-necessary dislocations (GNDs).

1.2.1.2 Work hardening theories

In this class of theories the athermal stress component, which is inversely proportional to the average dislocation spacing $\rho^{-0.5}$, serves as a hardening term [24, 29]:

$$\sigma = \sigma_0 + \alpha M G b \sqrt{\rho}. \quad (1.2)$$

σ_0 is a lattice friction stress. To arrive at the Hall-Petch relation, ρ needs to be inversely proportional to d . The essential assumption of the work hardening theories is that the mean free path of dislocations, Λ , is limited by the grain size d (not by the dislocation structure) so that $\Lambda = \beta d$ where β is a constant. Dislocations with a density of ρ gliding a distance L produce a plastic shear strain $\gamma = \rho b L$, so that $\rho = \gamma/(b \Lambda) = \gamma/(b \beta d)$ with $L = \Lambda$. Inserting the expression into Eq. (1.2) yields (1.1) with

$$k_{\text{HP}} = \alpha M G \sqrt{\gamma}/\sqrt{b \beta}. \quad (1.3)$$

Supporting evidence for this model was found by Conrad *et al.* [29] who showed that flow stress of niobium (columbium) is linear with the square root of strain as required by Eqs. (1.3) and (1.1) However, as ρ is not generally linearly dependent on ϵ and σ is not generally a parabolic function of ϵ as derived in Eq. (1.3), this treatment is not generally valid.

1.2.1.3 Grain boundary source theories

Li assumes grain boundaries to act as sources of dislocations [25, 26]. According to [26], let N be the total length of dislocations emitted per unit area of grain boundary at the time of yielding. Then the density of dislocations at the time of yielding is, for a spherical grain: $\rho = \frac{1}{2}\pi d^2 N / \left(\frac{1}{6}\pi d^3\right) = 3N/d$ where the factor 1/2 arises from the fact that each boundary is shared by two grains. Inserting ρ into Eq. (1.2) leads to the Hall-Petch relation with a slope:

$$k_{\text{HP}} = \alpha M G b \sqrt{3N}. \quad (1.4)$$

A similar version was proposed by Crussard [30, 31]. An experimental evidence of dislocation loops emitted from grain boundaries in an Fe-3.17%P alloy was reported by Hornbogen [32]. Recently van Swygenhoven demonstrated that grain boundary ledges act as sources as well as sinks for lattice dislocations in molecular dynamics simulations of nano Nickel [33].

1.2.2 Grain boundary softening and explanation

1.2.2.1 Grain boundary sliding and grain boundary diffusional creep

Since the well-known work of Chokshi *et al.* [16], the possibility of rapid diffusional creep in nano metals has received great attention [16, 34–36]. In addition, grain boundary sliding (GBS) has been considered as an important, even dominant process in plastic deformation of ufg and nano crystals [37–43].

GBS is generally believed to be the dominant mechanism of superplasticity, as it represents most of the strain in superplastic flow occurring at high temperatures [44]. Recently, three-dimensional molecular dynamic computer simulations predict that GBS also occurs at low temperature in nanocrystallines [45–49]. There is indirect evidence suggesting that grain-boundary sliding may occur more easily in ufg metals produced by SPD such as ECAP and high-pressure torsion [37–39, 41, 43, 50–56]. Valiev estimated the contribution of grain boundary sliding to total deformation to be 10~15% at room temperature [39]. He attributed the occurrence of GBS at relatively low temperature to the existence of highly non-equilibrium grain boundaries formed during ECAP [39, 54], which enable a faster diffusion process taking place to accommodate GBS. Recently a direct finding of low temperature GBS was reported for pure Aluminum (99.99%) processed by ECAP [57]. The authors employed depth sensing indentation (DSI) testing and atomic force microscopy (AFM) to show that there are significant differences in the indentation characteristics with and without the application of SPD. They concluded that GBS makes a very significant contribution of 40~70% strain in ECAP Al. Sklenička *et al.* estimated that the contribution of GBS to creep strain reaches 33% in the best case (12 passes of ECAP) [58]. In the phase mixture model developed by Kim *et al.* [59–61], the grain boundary softening effect was essentially accounted for by diffusional creep.

It seems clear that GBS will occur in the deformation of ufg materials, but it can hardly be an independent and rate-controlling process. If the deformation is entirely carried by GBS, theoretically a strain rate sensitivity as high as 0.5 would result [62, 63]. However, a maximum m -value of only about 0.14 was found in ufg Cu at 418 K as derived from Fig. 1.1 (also see [5, 8]). Similar findings have been reported by Höppel and Valiev [64] ($m = 0.14$ for ECAP Cu after 16 passes) and Valiev *et al.* ($m = 0.06$ for ECAP Cu after 2 passes). Hayes *et al.* also ruled out GBS as a rate controlling process based on the measured strain rate sensitivity and activation volume [65]. This suggests that dislocation activities must be considered.

1.2.2.2 Annihilation of dislocations at grain boundaries

The grain boundary softening behavior found in ufg Cu in its steady state deformation at elevated temperature was explained by Blum and coworkers by a thermally activated annihilation of dislocations at grain boundaries [5–8, 66, 67]. The idea is that in ufg Cu the mean free path of free dislocations is no longer determined by the dislocation structure, but is limited by the high-angle grain boundaries. Then fewer dislocations than normal are stored in the grain interior and more dislocations are stored at the grain boundaries. Therefore the situation becomes strongly dependent on grain boundary properties. As the diffusion process occurs much faster at grain boundaries than in grain interiors, dislocations are more easily annihilated at grain boundaries through thermally activated processes of structural rearrangement. Thus the grain boundaries may soften the material in the steady state where loss of dislocations must occur [5, 66].

A similar idea has been adopted by Wang and Ma to explain the low strain hardening rate found in ufg Cu [10]. An review was presented by Ovidka [9]. According to Wang and Ma [10] and Ovidka [9], in ufg and nano materials with grain size down to $d \approx 30$ nm, the lattice dislocations are still dominant in deformation. However, in contrast to the case of cg materials where lattice dislocations are mainly stored in grain interiors, in the ufg and nano cases dislocations are intensively stored at grain boundaries. Thus the deformation resistance is crucially influenced by grain boundaries [9, 10]. In this case, both the storage and annihilation of dislocations at grain boundaries strongly influence the deformation resistance. The storage process provides hardening, while the annihilation process provides tendency of softening. When the latter process prevails, the material becomes soft.

1.3 Scope of the current work

As described in the previous sections, the understanding of the deformation mechanism in ufg and nano materials is still unclear. So far, no satisfactory model, which incorporates rate equations governing the generation and annihilation of grain boundary dislocations, is available to interpret the grain boundary hardening and softening phenomena. The aim of the present work is to develop a simple dislocation model which catches significant fea-

tures of steady state deformation resistance of crystalline materials of various grain sizes. Two dislocation densities will be introduced to describe the microstructure: the density of dislocations in grain interiors and the density of dislocations stored at grain boundaries. The emphasis will be put on the derivation of rate equations of structure evolution, *i.e.*, the rates of generation and annihilation of the two dislocation species.

Extensive simulations will be presented on Cu with grain size varying in the range of $0.1 \mu\text{m} < d < 100 \mu\text{m}$. The steady state deformation resistance will be studied in two ways of i) dependence of $\dot{\epsilon}$ on σ and T at constant d ; and ii) dependence of σ on d at constant $\dot{\epsilon}$ and T . The simulation results will be compared with the experimental findings. The model will be assessed with a composite approach. Deficiencies of the model will be discussed.

2 Model

Contents

2.1	Basic considerations	12
2.1.1	Microstructure of coarse-grained and ultrafine-grained material	12
2.1.2	Assumptions and microstructure parametrization	13
2.1.2.1	Why a dislocation model?	13
2.1.2.2	Hardening by extrinsic dislocations	14
2.1.2.3	Annihilation of dislocations at grain boundaries	15
2.1.2.4	Microstructure parametrization	19
2.2	Evolution of microstructure	20
2.2.1	Generation of dislocations	20
2.2.1.1	Grain interior	20
2.2.1.2	Grain boundary	23
2.2.2	Annihilation of dislocations	26
2.2.2.1	Grain interior	26
2.2.2.2	Grain boundary	29
2.3	Kinetics of dislocation glide	31
2.3.1	Mobile dislocation density	31
2.3.2	Average glide velocity	31
2.4	Numerical implementation	32

2.1 Basic considerations

2.1.1 Microstructure of coarse-grained and ultrafine-grained material

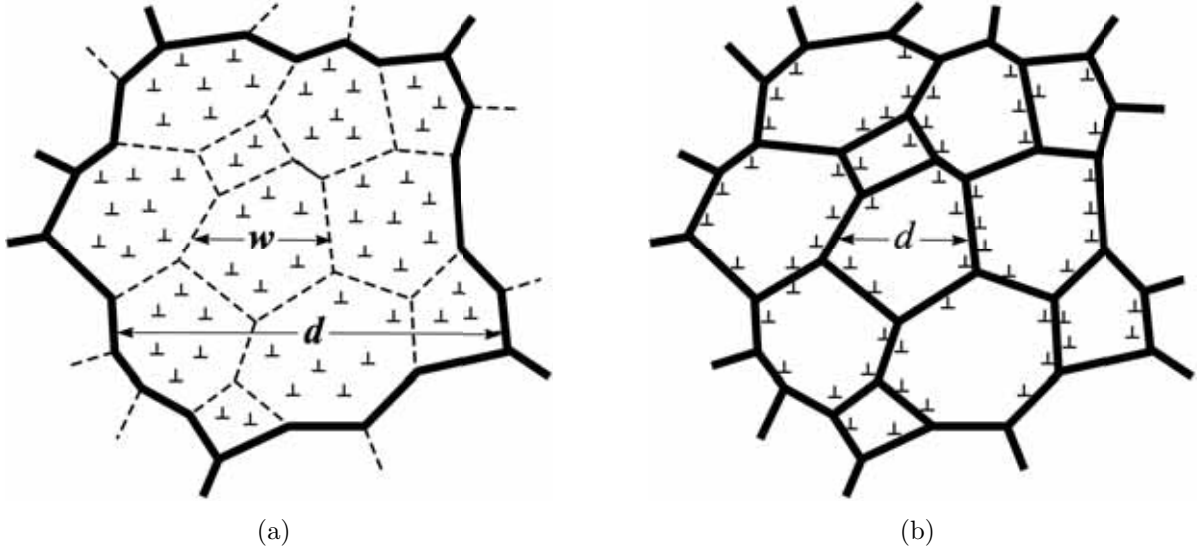


Figure 2.1: Schematic of a) subgrains of size w with free dislocations in grain interior in coarse grain of size d , b) ultrafine-grained structure with $d = w_\infty$. Thick lines: high-angle grain boundaries; Thin lines: low-angle subgrain boundaries.

In cg material the dislocations generally form a cellular structure within the grains (Fig. 2.1(a)). In the course of straining the cell boundaries build up increasing misorientations. In doing so they become more planar and take the character of low-angle grain boundaries. Naturally the state of order of these boundaries is not perfect, because the boundaries are subject to steady flows of dislocations entering and leaving them, thereby creating disorder. The cell size w (average spacing determined from the line intersection technique which is a measure of the boundary area per volume, $2/w$ for an equiaxed structure) soon reaches a value

$$w_\infty = k_w b G / \sigma \quad (2.1)$$

(k_w : factor between 10 and 30) found in the steady state of deformation [68, 69]. The low-angle (subgrain) boundaries generally have a strengthening effect [69–71].

The grain structure of the ufg Cu is a severely cold worked (not recrystallized) structure, with about 50% low-angle grain boundaries [54, 72]. That means that the cold worked structure also contains subgrains with w according to (2.1). When the as-produced material is subjected to a test under a stress being lower than the stress at which the ufg structure was achieved, firstly, new subgrains can no longer form inside the grains due to the fact that dislocations are not able to get stored in grain interiors, as the mean free path Λ_ρ of dislocations, which generally corresponds to a multiple of grain size w (factor of 2 to 4, see section 2.2.1.1 for details), becomes larger than the grain size. Thus the

dislocations are mainly stored at high-angle boundaries and not in the subgrain interior. Secondly, the existing subgrains are smaller than they will be at the reduced stress. Thus, one expects that the low-angle subgrain boundaries will disappear during deformation by migration and recombination with high-angle grain boundaries, in the attempt to attain w_∞ . This leads to the situation depicted in Fig. 2.1(b). This is the case for ufg Cu with $d = 0.35 \mu\text{m}$ in most of the investigated range as can be seen by calculating Λ_ρ and w_∞ from the observed flow stresses (see Fig. 2.2). Increase in subgrain size during deformation of ufg Cu has in fact been observed by transmission electron microscopy [73]. The virtual absence of low-angle boundaries makes the pronounced normal transient creep effects due to reversible subgrain coarsening/refinement disappear in the deformed ufg Cu [74]. Consistent with its history of predeformation and structure evolution, the ufg Cu attains a relative maximum of flow stress relatively early at $\epsilon \approx 0.05$, before approaching its steady state.

2.1.2 Assumptions and microstructure parametrization

The model to be outlined in the present work relies on a number of assumptions and simplifications:

- deformation is (only) mediated by dislocation motion;
- slip occurs spatially homogeneously within the grains;
- the grain boundaries are considered as internal surfaces where dislocations arrive without immediately losing their stress fields;
- each dislocation stored at the grain boundary is assumed to be in a dipolar configuration.

Justifications for the assumptions will be given below.

2.1.2.1 Why a dislocation model?

For Frank-Read sources emission of dislocation occurs if the total force on a source exceeds the Orowan stress σ_{source} for dislocation multiplication [75, 76]. The Orowan stress criterion is roughly given by

$$\sigma_{\text{source}} = \frac{2Gb}{l_s}, \quad (2.2)$$

where l_s is the length of dislocation segment acting as source. In the limiting case $l_s = d$, the sources cannot be activated if the applied stress is smaller and if stress concentrations are neglected. In this case, if plastic deformation still occurs, it cannot be connected to dislocation activity. Fig. 2.2 visualizes the relation l_s - σ/G for Cu. The grain sizes of cg and ufg Cu, which will be modelled in the present work, are also plotted to check whether the sources can be activated in these materials. It is seen that in the experimental range extending over a certain σ/G range, l_s is smaller than d indicating that there is no problem for activating the dislocation sources in the investigated stress range even in the absence

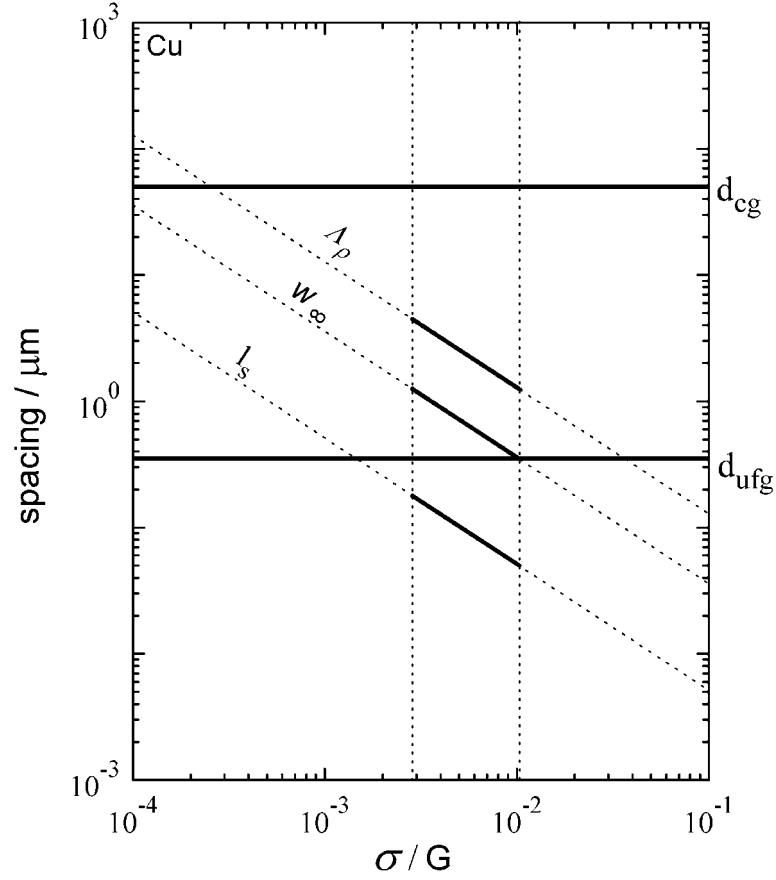


Figure 2.2: Mean free path of free dislocations $\Lambda_\rho = 50 b G/\sigma$, subgrain size w_∞ and critical size of dislocation sources as function of shear modulus normalized stress. Horizontal lines display the grain sizes d_{cg} for cg Cu and d_{ufg} for ufg Cu. Vertical dotted lines mark the boundary of experimental range where cg and ufg Cu were investigated by Li [5, 8].

of stress concentrations. This means that the first of the above assumptions is justified.

2.1.2.2 Hardening by extrinsic dislocations

Lattice dislocations trapped at high-angle grain boundaries generally keep their character as linear defects [77]. They cause lattice distortion near the grain boundary and increase the grain boundary energy [78]. This is illustrated by the fact that these extrinsic grain boundary dislocations can be made visible by transmission electron microscopy [78, 79].

Thus the extrinsic dislocations give rise to an athermal stress component. Formally the athermal stress given later by Eq. (2.30) is consistent to the one proposed by Ashby [80] who suggested that the geometrically necessary dislocations stored at grain boundaries contribute to hardening by creating a long-range back stress.

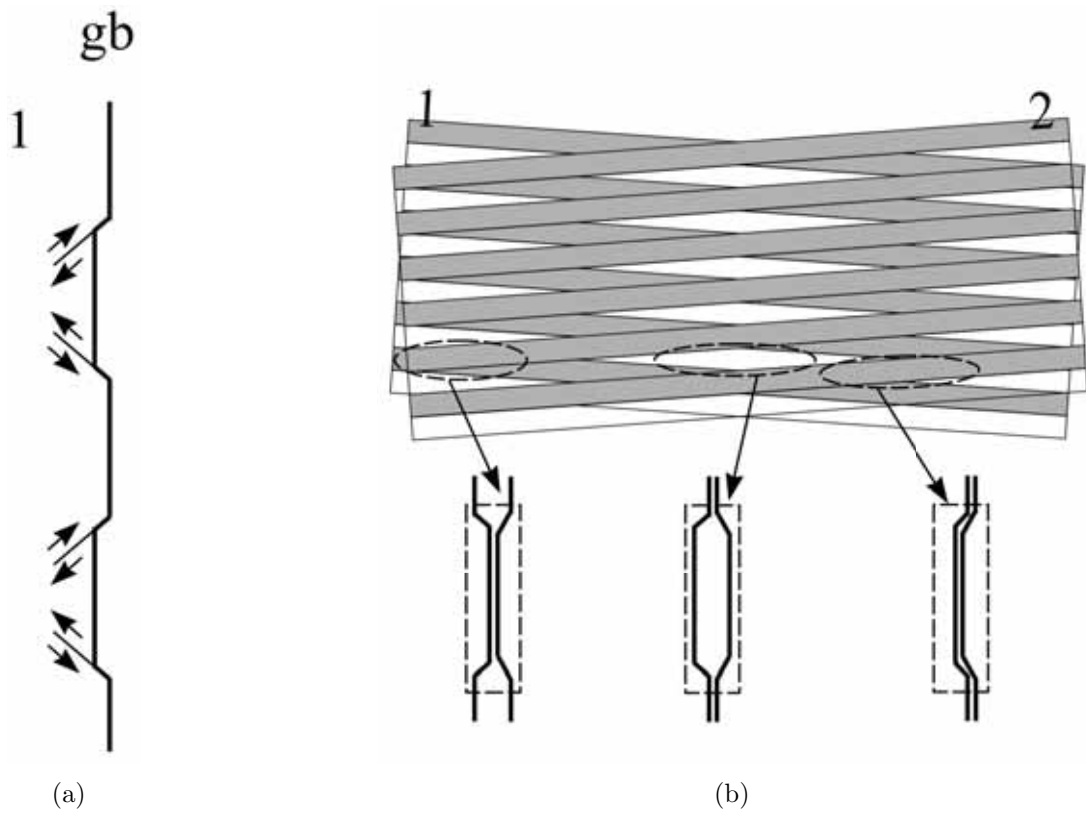
2.1.2.3 Annihilation of dislocations at grain boundaries

Grain boundary dislocation structure Figure 2.3 illustrates the arrangement of edge dislocations in a high-angle grain boundary. In symmetric double slip, edge dislocations form (single-sided) steps at the grain surface. A regular arrangement lead to valleys and hills. In a regular arrangement of dislocations there is a regular sequence of intrusions and extrusions which are connected to the single-sided steps of parallel hills and valleys (see Fig. 2.3(a)). This description holds only for the surface of single grains (single crystals). The grains are in contact with neighbours. Atomic attraction leads to stresses at the single-sided steps. When two such grains with a sequence of parallel hills and valleys are superimposed one gets the pattern of Fig. 2.3(b). Gray-gray superposition means two hills are in contact. White-white superposition means two valleys superimpose. Gray-white superposition means possible fit as valley superimposes with hill. In consequence, fit of the two grains can be reached by combining gray-gray and white-white areas such that only gray-white contacts remain. If this is the case, there is good fit everywhere due to the fact that the boundaries of hills agree with the boundaries of valleys and hills and valleys superimpose. Thus there is no elastic strain needed any more for closing valley-valley contacts and compressing hill-hill contacts. The fact that superposition of hill boundaries with valley boundaries can be attained, shows that the stresses related with the single-sided steps (extrinsic dislocations) can in principle be removed. This is possible by transport of matter by diffusion. The resulting grain boundary structure consists only of double sided steps, *i.e.* ledges.

Based on this consideration, the single-sided steps is simplified as regular dislocations with opposite signs. Fig. 2.3(c)) schematically show a regular arrangement of dislocations which form dipoles. These dipoles can eliminate each other by diffusion. The dipoles have opposite signs. The dislocations of these dipoles climb by absorption and emission of vacancies.

To quantify the rate of annihilation of the grain boundary dislocations, some approximations need to be made. By neglecting the slight difference in the Burgers vectors and line directions of the dislocations in dipolar configurations, one arrives at the pattern of Fig. 2.3(d). The regular arrangement of dislocations implies that the average distance between the dipole constituents $d_{\text{dip,gb}}$ scales with the average spacing of grain boundary dislocations s_{gb} . Generally the arrangement of dislocations at grain boundaries is irregular, so that it is difficult to make an good estimation of $d_{\text{dip,gb}}$. We assume here that the average dipole height equals the average spacing of grain boundary dislocations, namely,

$$d_{\text{dip,gb}} = s_{\text{gb}} \cdot \quad (2.3)$$



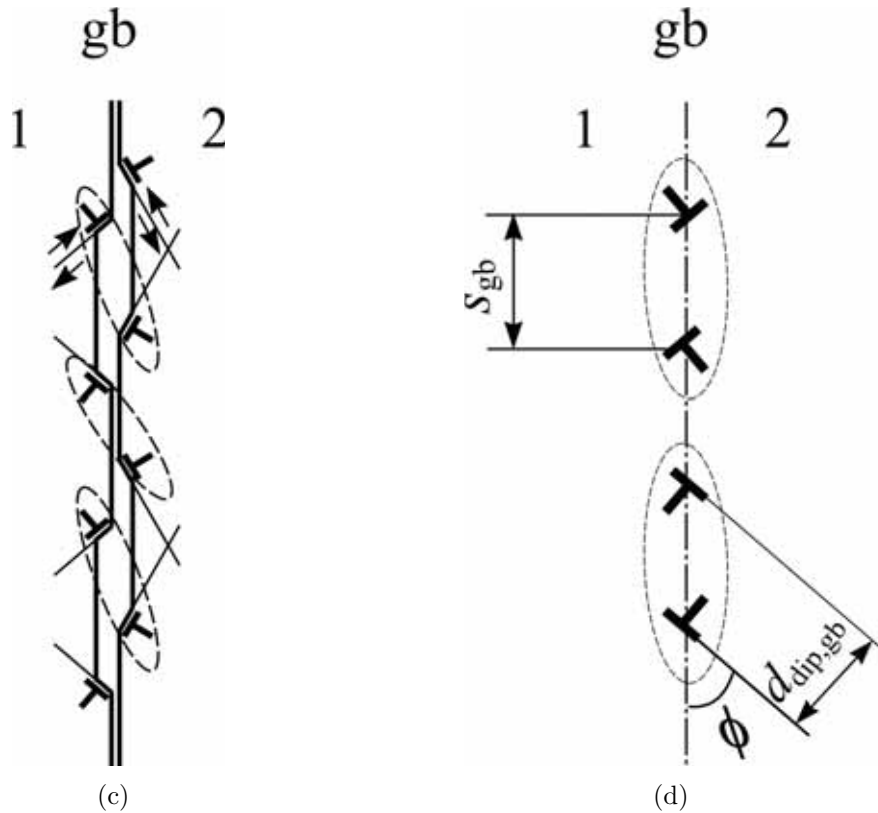


Figure 2.3: Schematic of edge dislocation structure in grain boundaries. a) grain 1 with a nonplanar surface due to intrusions (valleys) and extrusions (hills) produced by single-sided steps formed by edge dislocations resulting from symmetric double glide; b) superposition of two such grains (grain 1 and 2) with parallel gray-white sequence of hills and valleys which are in general not parallel for the two neighboring grains due to different grain orientations. The marked areas represent superpositions of valley-valley, hill-hill and valley-hill configurations from left to right; c) regular arrangement of dislocations in dipolar configurations resulting from single-sided steps of neighbouring grains on the two sides of the grain boundary; d) simplified picture of c) neglecting the differences in Burgers vectors and line directions of dislocations in dipolar configurations. s_{gb} : spacing of grain boundary dislocations; $d_{dip,gb}$: dipole height (spacing of glide planes); ϕ : angle between the slip plane and the grain boundary surface.

Annihilation of dislocation dipoles at grain boundaries According to Fig. 2.3(d), the dipoles may annihilate through climb of the extrinsic dislocations at the grain boundaries. In a grain boundary without perfect lattice of atomic positions dislocations on the two sides of the boundary need not have exactly the same Burgers vector and opposite sign to annihilate.

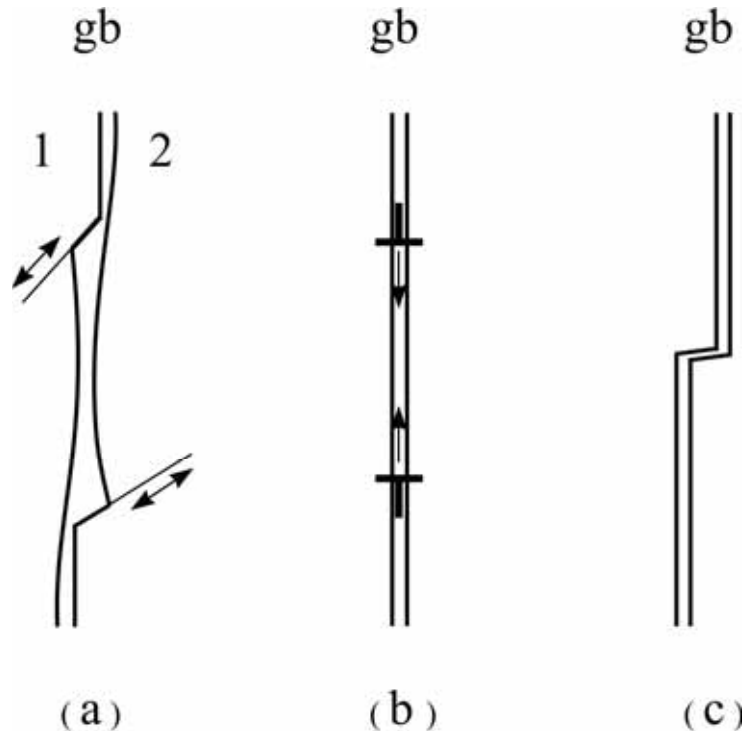


Figure 2.4: Schematic of the structure of extrinsic grain boundary dislocations. (a) a grain boundary between grain 1 and 2; (b) schematic dislocation picture of (a); (c) stress-free grain boundary ledge after recombination of steps by dislocation climb in grain boundary.

Fig. 2.4 illustrates the process of dissolution of a grain boundary dislocation dipole (formed in the way as demonstrated in Fig. 2.3) through mutual climb of dipole constituents. A lattice edge dislocation entering a high-angle boundary from one of the two neighboring crystallites forms a step at the surface of that crystal while the surface of the neighboring crystal remains unchanged. An analogous single-sided step results from glide in the second crystallite. Despite the slight difference in Burgers vectors and line directions, the two steps in Fig. 2.4(a) react by diffusive processes in the boundary to form a ledge with reduced stress field (Fig. 2.4(c)). In an approximative manner we treat this process of ledge formation from two single-sided steps as dissolution of a dislocation dipole (Fig. 2.4(b)) [81]. Note that the lack of crystalline order at the boundary is the prerequisite for the formation of ledges as shown in Fig. 2.4(c). This process cannot happen so easily inside the grain unless the Burgers vectors of reaction partners are exactly equal.

2.1.2.4 Microstructure parametrization

The dislocation structure is described in a statistical manner. The microstructural parameters entering the model are the density (dislocation length per crystal volume) ρ_f of free dislocations in grain interiors, the areal density N_{gb} (dislocation length per grain boundary area) at grain boundaries, the mean grain size d , and the width of grain boundary δ_{gb} (see Fig. 2.5). Dislocations in the grain interior may exist in the form of dipoles (see the pairs

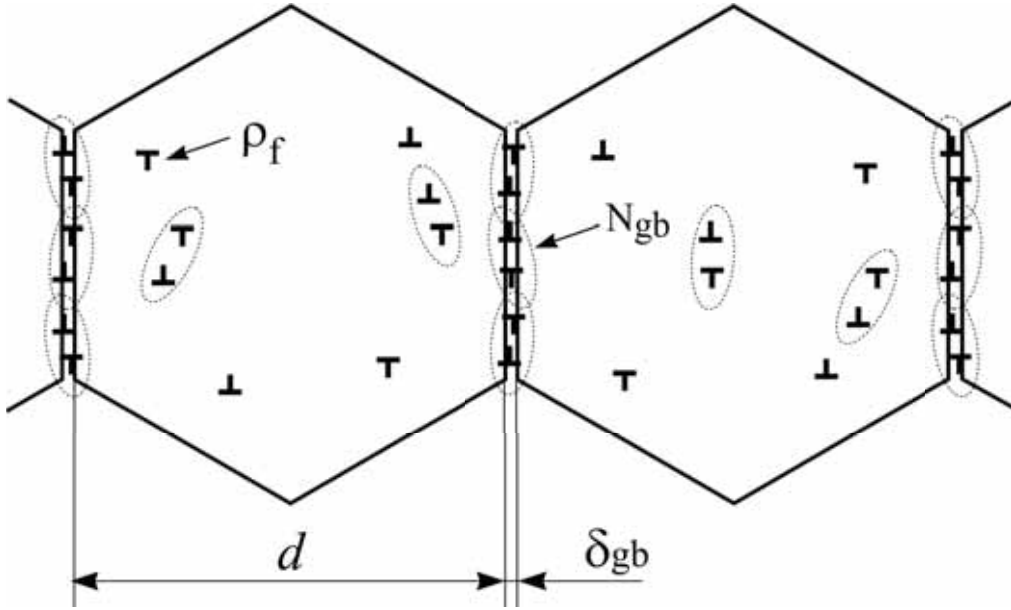


Figure 2.5: Schematic of the microstructure with dislocations described by: ρ_f : density of free dislocations in grain interior; N_{gb} : areal density of dislocations at grain boundaries; d : grain size; δ_{gb} : the width of grain boundary. Dashed ellipses mark dislocations in a dipolar configuration.

of dislocations marked by the dashed ellipses in Fig. 2.5) and in the form of singles. For the dislocations deposited at the grain boundaries, all the dislocations are assumed to be in dipolar configurations as stated before. In principle, both edge and screw dislocations can form dipoles. Since the annihilation of screw-dipoles through cross slip is generally easier than the annihilation of edge-dipoles through climb, the rate of annihilation is determined by edge-dipoles. Therefore, only edge-dipoles are considered in the current work.

The average grain boundary dislocation density (length per volume) ρ_{gb} is the areal density N_{gb} (length per area), times the grain boundary area per volume $2/d$:

$$\rho_{gb} = N_{gb} \frac{2}{d}. \quad (2.4)$$

The average spacing of free dislocations δ is defined as

$$\delta = \rho_f^{-0.5}. \quad (2.5)$$

is called spacing of free dislocations. The average spacing of grain boundary dislocations s_{gb} equals the reciprocal of the length of dislocations per grain boundary area, namely,

$$s_{\text{gb}} = \frac{1}{N_{\text{gb}}}. \quad (2.6)$$

In the following the rates of evolution of dislocation densities as well as the kinetics for dislocation motion will be derived.

2.2 Evolution of microstructure

Dislocations are generated as free ones from sources and then glide in their slip plane to produce plastic strain until they leave the crystal or annihilate through formation of dipoles. The formation and annihilation of dipoles during deformation lead to a decrease in dislocation line energy. The current model considers two kinds of mechanisms of dislocation annihilation. If the distance between dipole constituents is smaller than a certain value d_{spont} , the mutual attraction force between the dislocations is sufficient high to leads to an immediate annihilation [82, 83] (Fig. 2.9(a)); otherwise the dipole constituents need to approach each other through a thermally activated process (Fig. 2.9(b)). The net rate of change of dislocations equals the difference between the generation rate of dislocations (denoted by "+" in the superscript) and the sum of the annihilation rates (denoted by "-" in the superscript, spon: spontaneous annihilation, therm: thermally activated annihilation). A steady state of deformation is attained when the generation rate equals the annihilation rate.

$$\dot{\rho} = \dot{\rho}^+ - \dot{\rho}^- \quad (2.7)$$

$$\dot{\rho}^- = \dot{\rho}^{-,\text{spon}} + \dot{\rho}^{-,\text{therm}} \quad (2.8)$$

In following, the rates for the generation and annihilation of dislocations will be formulated.

2.2.1 Generation of dislocations

2.2.1.1 Grain interior

The rate of storage of free dislocations in crystals is written as

$$\dot{\rho}_f^+ = \frac{2}{b\Lambda_\rho} \dot{\gamma}. \quad (2.9)$$

where Λ_ρ is the mean free path of dislocations [70, 84, 85] and $\dot{\gamma}$ is the shear strain rate. If the dislocations are circular loops [70], Λ_ρ equals the average radius of the dislocation

loops at the point of storage. The length of free dislocations generated per slipped area is determined as $2\pi\Lambda_\rho/(\pi\Lambda_\rho^2) = 2/\Lambda_\rho$. Statistically the mean free path Λ_ρ is proportional to the spacing of free dislocations δ (see Eq. (2.5)):

$$\Lambda_\rho = k_\rho \delta, \quad (2.10)$$

where k_ρ is a constant [11, 70, 85, 86]. As can be derived from the rate of work hardening in stage II of single crystal deformation, the quantity k_ρ equals $\alpha G/\theta_{II}$ (α : dislocation interaction constant, G : shear modulus, θ_{II} : rate of hardening in stage II of single crystal deformation), which approximately equals 50 [11]. The mean free path of 50δ corresponds to about 2 subgrains (2.1). The quantity k_ρ has been derived by Nes [70] as

$$k_\rho = \frac{1}{2\sqrt{p}}, \quad (2.11)$$

where $p \approx 10^{-4}$. p is the probability for a dislocation loop expanding on its slip plane to be stored per dislocation encountered¹.

Relation (2.10) only applies to the situation where the grain size d is much larger than the mean free path of free dislocations Λ_ρ and the dislocation loops get stored in the grain interior (Fig. 2.6(a)). With decreasing grain size, more and more dislocation loops are able to reach the grain boundaries. Accordingly, the length of free dislocations generated in the grain interior per slipped area $2/\Lambda_\rho$ is reduced (Fig. 2.6(b)). In the limit of very small grains, dislocation storage in the grain interior virtually ceases. In this case, the length generated per slipped area $2/\Lambda_\rho$ in the grain interior approaches 0. This indicates that the mean free path of free dislocations is not only a function of the average spacing between free dislocations δ (see Eq. (2.10)), but also a function of grain size d .

Based on Nes' statistical approach [70], the grain-size dependent storage rate of free dislocations in grain interiors can be derived in several steps. If there are dN_m loops which are generated per volume in the interval $d\gamma$, a certain fraction of dN_m loops will get stored due to interactions with other dislocations during expanding. Within a certain area, the more dislocations a loop encounters during expanding, the more interactions occur to stop the loop from further expanding (see Fig. 2.7). This means that the probability of a loop getting stored is dependent on the dislocation density (or the spacing between dislocations). Hence, the first step is to statistically determine the number of dislocation loops $dN(d/2, \delta)$ which get stored within the grain of size d . Then one can determine the length of the stored dislocation loops and the shear strain produced by these loops per volume. The ratio of these two quantities gives the *total* length of dislocation generated per shear strain in grain interiors $d\rho_f/d\gamma$.

Figure 2.7(c) schematically display the probability derived from Eq. (A.6) of dislocation loops getting stored within grains of different sizes. For a certain dislocation spacing, *e.g.*

¹This is identical to the probability per slipped area and per total dislocation density ρ_f introduced by Nes, as the product of the two equals the number of encountered dislocations

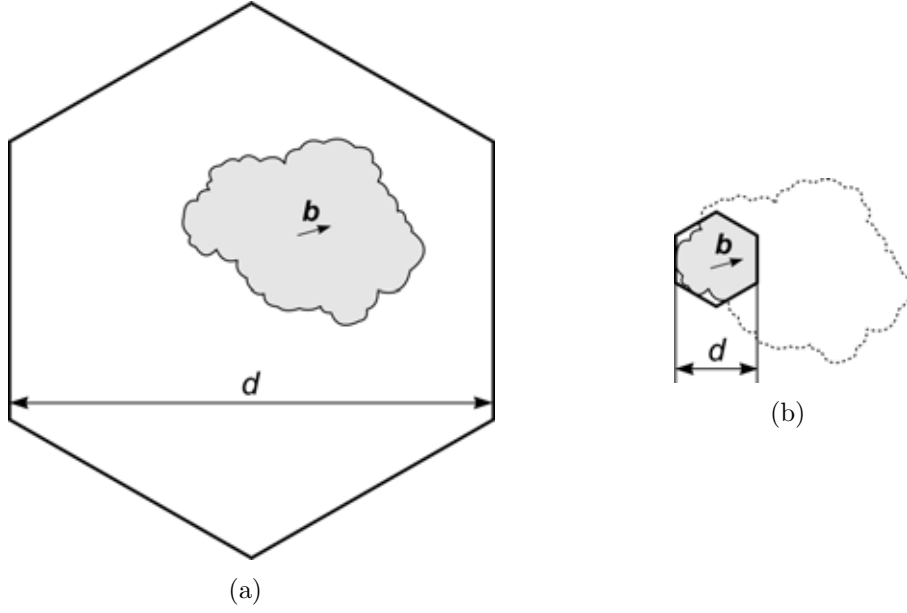


Figure 2.6: Schematic of the comparison between the slipped area (gray region) and the cross section of a grain. a) the dislocation loop is completely stored in the grain interior; b) most part of the dislocation loop is stored at the grain boundary.

δ_1 , for a large grain of size d_{cg} , all loops are stored in the grain interior (bounded by the thick line in Fig. 2.7(a)), the probability reaches 1 (see Fig. 2.7(c)). For the small grain of size d_{ufg} , the probability stays below 1 as only a few small loops can be stored within the small grain, the rest enters the grain boundary (bounded by the thick line in Fig. 2.7(b)). When the dislocation spacing becomes larger (as is usually the case of deformations at low stresses), even the probability of the storage of dislocation loops within the large grain of size d_{cg} becomes smaller than 1. Accordingly, the storage rate is reduced.

The generation rate of dislocations in grain interior is derived in appendix A.2. From Eqs. (A.12) and (2.9) one obtains the expression for the length of dislocations stored in the grain interior per slipped area:

$$\frac{2}{\Lambda_{\rho,d}} = \frac{2\bar{r} \left(1 - \exp\left(-p\rho_f \pi r'^2\right)\right)}{\left(\bar{r}^2 + \left(r'^2 - \bar{r}^2\right) \exp\left(-p\rho_f \pi r'^2\right)\right)}. \quad (2.12)$$

Here \bar{r} is the average radius of the dislocation loops being stored in grain interiors; r' is proportional to the grain size d (see Appendix A.1 for the geometrical factor). For coarse grains ($r' \rightarrow \infty$), $\frac{2}{\Lambda_{\rho,d}}$ equals $\frac{2}{\bar{r}}$ with $\bar{r} \rightarrow k_\rho \rho_f^{-0.5}$. This means that $\Lambda_{\rho,d}$ become identical to Λ_ρ (see 2.10). As the grain size decreases ($r' \rightarrow 0$), $\frac{2}{\Lambda_{\rho,d}}$ is a grain-size dependent quantity which accounts for the influence of grain boundary on the storage of dislocations in grain interiors.

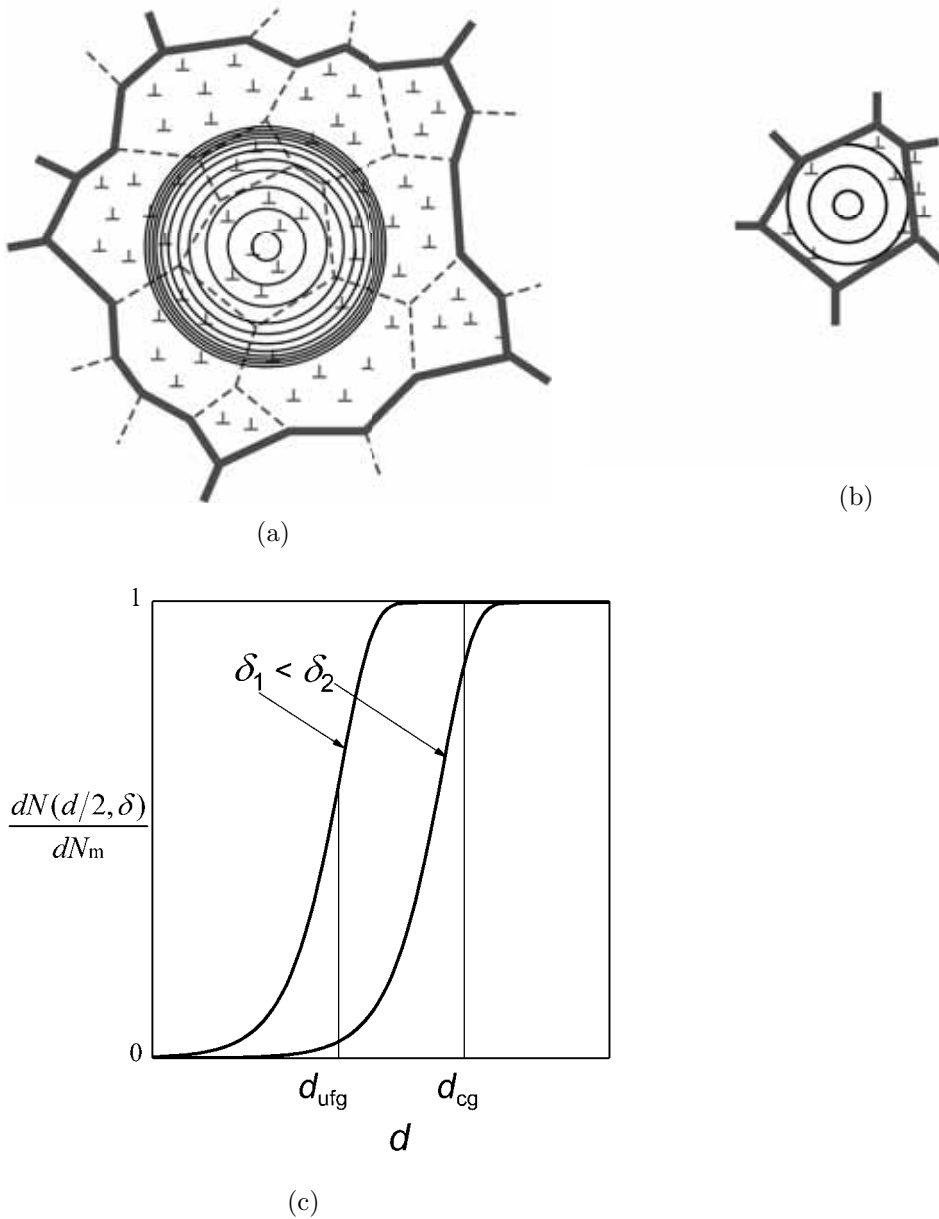


Figure 2.7: Schematic of dislocation loops in a) a large and b) a small grains, and c) the probability of loops getting stored within grains as a function of dislocation spacing δ and grain size at the same deformation condition.

2.2.1.2 Grain boundary

Penetration of grain boundaries by free dislocations is in general impossible. Note that the penetration means passage of the whole dislocation, not nucleation in the neighbouring grain at a point near the grain boundary; the latter is always possible, but does not affect the storage rate of dislocations in the boundaries. The grain boundaries are thus

filled with dislocations coming from neighbouring grains. The mean free path Λ_{gb} of such dislocations is proportional to grain size d .

The rate of dislocation length stored at grain boundaries per volume is derived in appendix A.3). Combining Eqs. (A.19) and (2.4) leads to the rate of dislocation length stored per grain boundary area:

$$\dot{N}_{\text{gb}}^+ = \frac{1}{2k_{\text{gb}}b} \cdot \dot{\gamma}. \quad (2.13)$$

where k_{gb} is a geometrical constant equal to 0.5.

Summary From Eq. (A.19) the length of dislocation which is deposited per slipped area at the grain boundaries can be determined as

$$\frac{2}{\Lambda_{\text{gb}}} = \frac{2}{2k_{\text{gb}}d} = \frac{2}{d}. \quad (2.14)$$

Combining Eqs. (2.12) and (2.14) yields the total length of dislocations generated in grain interiors and at grain boundaries per slipped area

$$\frac{2}{\Lambda_{\text{tot}}} = \frac{2}{\Lambda_{\rho,d}} + \frac{2}{\Lambda_{\text{gb}}}. \quad (2.15)$$

Figure 2.8 shows the length of dislocations generated per slipped area versus δ for several grain sizes d . The curve for $2/\Lambda_{\rho}$ was derived from Eq. (2.10) with a constant k_{ρ} (see Table: 3.2) meaning that the length of free dislocations generated in grain interiors per slipped area is exclusively determined by the free dislocations themselves within grains without any influence of grain boundaries. This line serves the purpose to assess the relative significance in the contributions of free dislocations in grain interiors and dislocations at grain boundaries to the total rate of generation of dislocations. The curves for $2/\Lambda_{\text{tot}}$ (total length of dislocations generated in grain interiors and at grain boundaries per slipped area (see Eq. 2.15)) display a kink where Λ_{ρ} (see Eq. (2.10)) approximately equals the grain size d . At the left of this point $2/\Lambda_{\text{tot}}$ progressively agrees with $2/\Lambda_{\rho}$ with decreasing spacing of free dislocations δ . This means that the *total* rate of dislocation generation is determined by the *free* dislocations in grain interiors. This is in agreement with the fact that the length of free dislocations generated per slipped area $2/\Lambda_{\rho,d}$, which progressively increases in proportion to decreasing δ , approximately equals $2/\Lambda_{\rho}$ and $2/\Lambda_{\text{tot}}$ in large grains. At the right of this point $2/\Lambda_{\text{tot}}$ levels off. The corresponding level of *total* mean free path Λ_{tot} equals the grain size d indicating that the *total* rate of generation of dislocations is no longer dominated by the rate of generation of *free* dislocations in grain interiors but by the rate of generation of dislocations at grain boundaries. And the *total* rate of dislocation generation is enhanced due to $d < \Lambda_{\rho}$. It can be seen that $2/\Lambda_{\rho,d}$ continuously decreases in proportion to δ^2 with increasing δ . This is due to the fact that more dislocations reach the boundaries and fewer are stored inside the grains as the average free dislocation spacing increases.

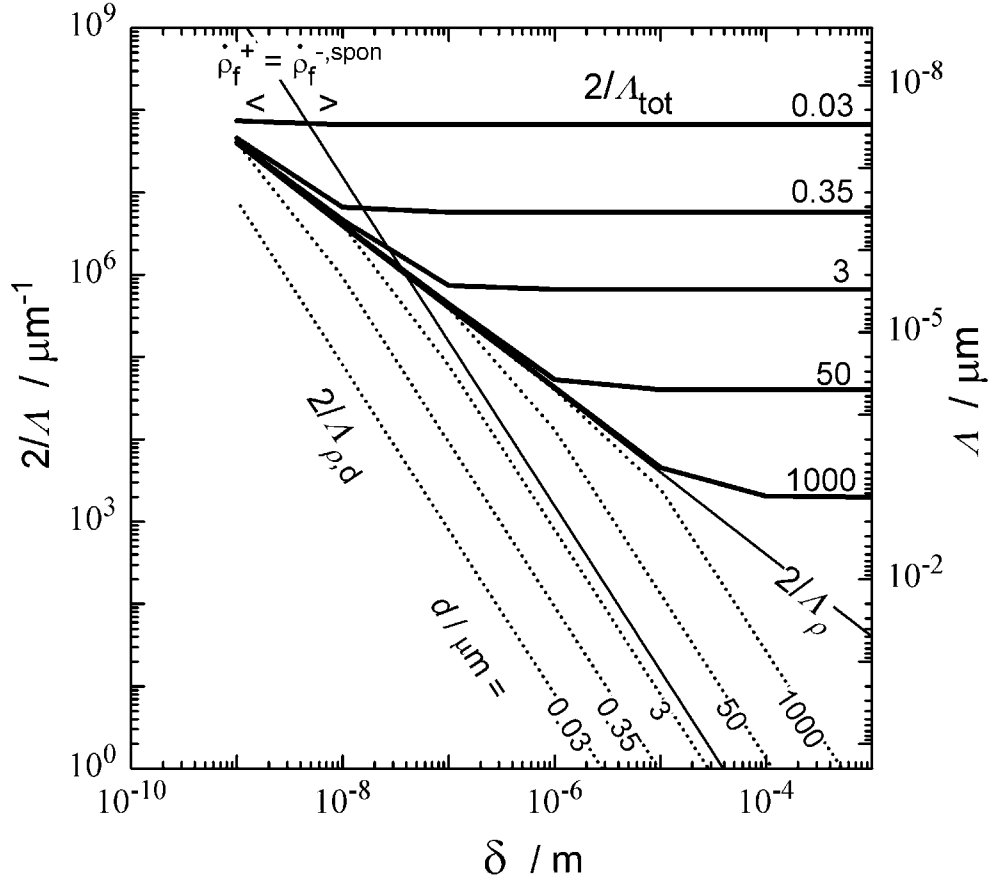


Figure 2.8: Relation between length of dislocations generated per slipped area and spacing of free dislocations δ . $2/\Lambda_{\rho,d}$ (Eq. (2.12)) and $2/\Lambda_{\rho}$ (Eq. (2.10)): length of free dislocations generated in grain interiors per slipped area; $2/\Lambda_{\text{tot}}$: total length of dislocations generated in grain interiors and at grain boundaries per slipped area (Eq. (2.15)); The line marked by $\dot{\rho}_f^+ = \dot{\rho}_f^-, \text{spon}$ is derived by equating the rate of generation (2.9) and the rate of spontaneous annihilation (2.16) of free dislocations. The symbols $<$ and $>$ mark the area as where the generation rate $\dot{\rho}_f^+$ is smaller or larger than the annihilation rate $\dot{\rho}_f^-, \text{spon}$, respectively.

2.2.2 Annihilation of dislocations

Depending on temperature and stress the annihilation of dislocations may take place in two manners. In the following sections the rates of annihilation of dislocations in grain interiors and at grain boundaries will be formulated, respectively.

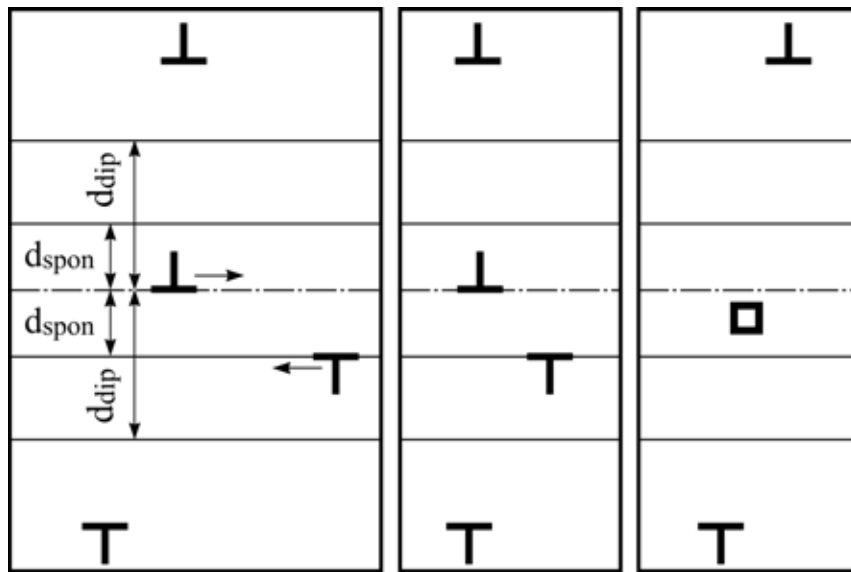
2.2.2.1 Grain interior

Spontaneous annihilation Kocks [87] proposed that dynamic recovery is controlled by glide of dislocations to (unspecified) recovery sites. A more detailed description of glide-controlled recovery was given by Essmann and Mughrabi [88] who proposed that the recovery site of a gliding dislocation is provided by a dislocation of opposite sign lying on a parallel glide plane which is less than a spacing $d_{\text{spont},f}$ apart from that of the incoming dislocation (Fig. 2.9(a)). Assuming spatially homogeneous distribution of the dislocations of equal sign, the rate of spontaneous annihilation of free dislocation density thus equals the volume fraction $(\dot{\gamma}/b) 2 d_{\text{spont},f}$, which is sampled per time by the gliding dislocations for potential annihilation partners, times the length per volume $2(1/(2n_g))\rho_f$ of such partners of one glide system; n_g is the number of active slip systems so that $1/(2n_g)$ is the average fraction of dislocations with Burgers vectors of opposite sign. The leading factor 2 is appropriate as both dislocations disappear in each annihilation event [82, 83]:

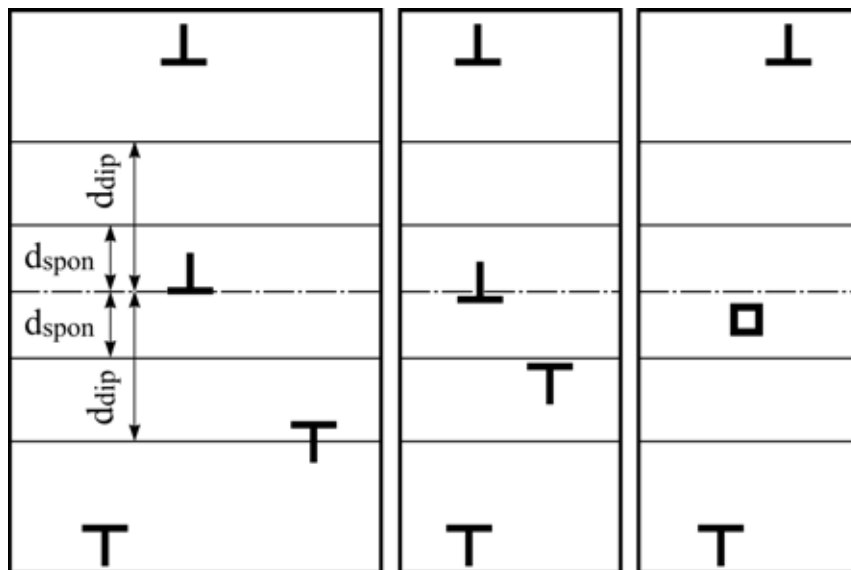
$$\dot{\rho}_f^{-,\text{spont}} = \frac{\dot{\gamma}}{b} 2d_{\text{spont},f} \times \frac{\rho_f}{n_g}. \quad (2.16)$$

The spontaneous annihilation usually takes place at low temperature and high stress as a high density of dislocations results. Figure 2.8 also shows the line where generation of free dislocations is compensated by spontaneous annihilation. At the left of this line spontaneous annihilation of dislocations outweighs generation of free dislocations. This means that the density of free dislocations in the grains must decrease. This is due to the relatively small spacings of free dislocations which make spontaneous annihilation a rather probable event. Note that not only single dislocations, but also free dislocations in dipolar configuration are subject to such spontaneous annihilation with bypassing gliding dislocations. In the case of the curves for $2/\Lambda_{\rho,d}$, which intersect this line, a steady state free dislocation density is reached when the generation rate equals the annihilation rate at the intersection point. In the case of the curves for $2/\Lambda_{\rho,d}$, which do not intersect this line, the free dislocation density must steadily decrease. This is due to the fact that the mean free path $\Lambda_{\rho,d}$ increases more strongly with δ .

Thermally activated annihilation The rate of thermally activated annihilation is derived under the assumption that steady state deformation is controlled by climb of edge dislocations [89–91]. Dislocation climb occurs by diffusion of vacancies to or away from the site of the dislocation leading it to move out of the slip plane onto a parallel plane directly above or below the slip plane.



(a) spontaneous annihilation



(b) thermally activated annihilation

Figure 2.9: Formation of dipoles by mutual attraction of free dislocations with Burgers vectors of opposite sign within slip planes of d_{dip} apart. Within the spacing d_{spon} , the dipole disappears spontaneously; Beyond the spacing d_{spon} but within d_{dip} , the dipole constituents overcome the distance of d_{dip} through mutual climb. Vacancy debris (open squares) are left after annihilation.

The rate, at which dislocation length is annihilated per volume through the thermally

activated process, is

$$\dot{\rho}_f^{-,\text{therm}} = \rho_{\text{dip},f} \nu_{c,f}, \quad (2.17)$$

where $\rho_{\text{dip},f}$ is the density of dislocations existing in dipolar configuration, and $\nu_{c,f}$ is the frequency of annihilation.

Dipoles exist with a dipole separation between $d_{\text{spon},f}$ (minimum) and $d_{\text{dip},f}$ (maximum separation of stable dipoles at stress σ). The frequency is assumed to be controlled by the time interval at which the distance $(d_{\text{dip},f} - d_{\text{spon},f})/2$ has been overcome by climb (Fig. 2.9(b)):

$$\nu_{c,f} = \frac{2v_{c,f}}{(d_{\text{dip},f} - d_{\text{spon},f})/2} \quad (2.18)$$

The factor 2 in the numerator accounts for the factor that two dislocations disappear in each annihilation event. Following a simple approach [11, 70], the density of dislocation dipole $\rho_{\text{dip},f}$ is assumed to be a fraction of the density of free dislocations ρ_f , namely,

$$\rho_{\text{dip},f} = f_{\text{dip}} \rho_f. \quad (2.19)$$

An intensive study of the evolution of $\rho_{\text{dip},f}$ presented by Eisenlohr [92] shows that when the annihilation is controlled by the thermally activated process, the ratio of the single dislocation density to the dipole density is almost stress independent showing only a slight decrease with increasing stresses. This statement suggests a scaling relation between ρ_f and $\rho_{\text{dip},f}$ as postulated in Eq. (2.19).

The average separation between dipole constituents $d_{\text{dip},f}$ is assumed to be proportional to the average spacing of free dislocations of one glide system:

$$d_{\text{dip},f} = \frac{\rho_f^{-0.5}}{\xi}. \quad (2.20)$$

where ξ is a constant. The dipole capture spacing is expressed in [83, 93] by the passing stress of parallel edge dislocations which is inversely proportional to stress. The same inverse proportionality results from (Eq. 2.20) if δ is inversely proportional to stress as is usually the case [69].

The climb velocity $v_{c,f}$, at which the dipole constituents climb perpendicular to their slip planes, is expressed as [27, 94]

$$v_{c,f} = \frac{D_{\text{sd}}}{b} \left[\exp\left(\frac{\sigma_{c,f} \Omega}{k_B T}\right) - 1 \right] \quad (2.21)$$

where D_{sd} is the coefficient of volume diffusion, Ω is the atomic volume, k_B is Boltzmann constant, and $\sigma_{c,f}$ is the climb stress of dipole constituents. This formula was proposed for the case that dislocations are perfect. In reality they are split into partials with a stacking fault in between. The splitting reduces the climb rate. Climb is concentrated at jogs and becomes dependent on jog density and stacking fault energy. The dependence on

jog spacing may enhance the stress dependence of the climb velocity. Eq. (2.21) has been modified by Argon and Moffatt by incorporating the stack fault energy [95]. The formation and concentration of jogs has been treated by many others [92, 96, 97]. For simplicity the influence of splitting and jogs is neglected here. This means that the thermally activated annihilation rate is somewhat overestimated.

$\sigma_{c,f}$ is the stress which drives the dipole constituents to climb towards each other. As mentioned above, dipoles exist with dipole separations between $d_{\text{spn},f}$ and $d_{\text{dip},f}$. Thus an average dipole can be defined with an average separation of $(d_{\text{dip},f} + d_{\text{spn},f})/2$. The climb stress can be expressed as a function of the average dipole separation

$$\sigma_{c,f} = \frac{Gb}{2\pi(1-\nu)} \frac{1}{(d_{\text{dip},f} + d_{\text{spn},f})/2} \quad (2.22)$$

(ν : Poisson's ratio)

It might be better to treat the dipole density $\rho_{\text{dip},f}$ as an explicit microstructure parameter as was done, for example, in the work of Roters [98], Roters *et al.* [82] and Blum *et al.* [83] and Eisenlohr [92]. The intention of discarding this parameter in the present work is to make the model as simple as possible. Compared to the model of thermally activated annihilation presented in [83] where the evolution of dipole density was separately formulated, the present simplified model will not bring about any qualitative difference. By carefully choosing the relevant model parameters, quantitative differences can be minimized. In addition, since there are very few dislocations within ultrafine grains, the simplification in the treatment of the annihilation rates of free dislocations will not result in significant influences on the simulation results. Using the simplified model facilitates to assess the role of grain boundary dislocations in deformation without paying much attention to the detailed configuration of free dislocations in grain interiors.

2.2.2.2 Grain boundary

Annihilation of dislocations in the grain boundary is described by similar concepts as in the grain interior (section 2.2.2.1). The rates of annihilation will be derived for one glide system.

Spontaneous annihilation Whenever a dislocation arrives at the boundary within a distance $d_{\text{spn},\text{gb}}$ from an annihilation partner, *i.e.* an already present dislocation from the neighbouring grain with nearly the same Burgers vector and opposite sign, spontaneous annihilation of both occurs.

According to Fig. 2.3(c) the probability of an intruding dislocation to find an appropriate annihilation partner (with the same Burgers vector and opposite line direction) equals $2d_{\text{spn}}/(2n_g s_{\text{gb}})$. Considering that two dislocations disappear in each annihilation event, the rate, at which the spontaneous annihilation occurs, equals two times the product of the

storage rate of dislocations at grain boundaries and the probability for a grain boundary dislocation to be spontaneously annihilated determined above

$$\dot{N}_{\text{gb}}^{-,\text{spon}} = 2 \dot{N}_{\text{gb}}^{+} \frac{d_{\text{spon,gb}}}{n_{\text{g}} s_{\text{gb}}} . \quad (2.23)$$

Combining Eqs. (2.13), (2.6) and (2.3) yields

$$\dot{N}_{\text{gb}}^{-,\text{spon}} = \frac{1}{k_{\text{gb}}} \frac{\dot{\gamma}}{b} d_{\text{spon,gb}} \times \frac{N_{\text{gb}}}{n_{\text{g}}} . \quad (2.24)$$

Thermally activated annihilation The rate, at which dislocation length is annihilated per grain boundary area through the thermally activated process is

$$\dot{N}_{\text{gb}}^{-,\text{therm}} = N_{\text{gb}} \nu_{\text{gb}} , \quad (2.25)$$

where ν_{gb} is the frequency of annihilation, which is estimated to be determined by the velocity of climb $v_{\text{c,gb}}$ at which the distance $(d_{\text{dip,gb}} - d_{\text{spon,gb}})/2$ is overcome by each climbing annihilation partner:

$$\nu_{\text{gb}} = \frac{2v_{\text{c,gb}}}{(d_{\text{dip,gb}} - d_{\text{spon,gb}})/2} . \quad (2.26)$$

Climb occurs through diffusive motion of matter or point-defects like vacancies or interstitials to or from the climbing dislocations. For the climb of grain boundary dislocations, matter mainly diffuses along the grain boundary, while vacancies or interstitials mainly diffuse through the lattice. For pure Cu we ignore the diffusive motion of interstitials as vacancies are the main point-defects. Thus the climb velocity is connected to the diffusion fluxes of matter and vacancies along the grain boundary and through the lattice respectively. The diffusion flux is the product of the current density of atoms or vacancies given by Fick's first law and the relevant areas across which the currents flow. Detailed derivations of the fluxes of matter and vacancies are presented in appendix A.4. From Eqs. (A.26), (A.34) and (A.48) one obtains the climb velocity of grain boundary dislocations:

$$\begin{aligned} v_{\text{c,gb}} &= \frac{2}{\pi(1-\nu)} \frac{G\Omega}{k_{\text{B}}T} \delta_{\text{gb}} D_{\text{b}} \frac{1}{s_{\text{gb}}^2} \\ &+ \frac{D_{\text{sd}}}{b} \left[\exp\left(\frac{\sigma_{\text{c,gb}}\Omega}{k_{\text{B}}T}\right) - 1 \right] \frac{2\pi}{\ln[R^2/(b s_{\text{gb}})]} . \end{aligned} \quad (2.27)$$

where $\sigma_{\text{c,gb}}$ (Eq. (A.37)) is the mutual attractive between the dipole constituents; R is the distance from the dislocation to the region where the concentration of vacancies being in equilibrium. In the present case, one may choose $R \approx d/2$.

2.3 Kinetics of dislocation glide

The strain rate $\dot{\epsilon}$ is determined by the product of density ρ_f of free dislocations and their average velocity v_g [99]:

$$\dot{\epsilon} = \frac{M}{b} \rho_f v_g. \quad (2.28)$$

This formula connects the macroscopic strain to the average velocity of individual dislocations. In following the ingredients of Eq. (2.28) will be determined.

2.3.1 Mobile dislocation density

When dislocations move, the slipped area per volume expands, thus strain results. The slipped area expands or the dislocation length (as the circumference of the slipped area) increases with a certain velocity, thus strain rate is determined. If the dislocations move in a stop and go manner, so that only the density ρ_{mob} of mobile dislocations is moving at the average velocity v_{mob} [69], then one needs to quantify ρ_{mob} and v_{mob} . Attempts have been made to identify ρ_{mob} [100–102]. However, so far there is no generally agreed theory or approach available. One may argue that in steady state deformation all dislocations must be able to move somehow. In that sense one may describe the strain rate by the total dislocation density and the average velocity of the total dislocations. In addition, one may introduce a factor f_{mob} to account for the fact that dislocations are not always moving at the assumed glide velocity v_g of all dislocations, but may intermediately wait at obstacles (stop and go). This factor can be integrated into the equation of average velocity.

2.3.2 Average glide velocity

Thermal and athermal stress The average glide velocity v_g depends not only on the applied stress σ , but is limited by dislocation interaction at a given temperature T [83]. According to the classical effective stress approach, the average glide velocity v_g of mobile dislocations is a monotonic function of the effective stress σ^* available for thermally activated overcoming of obstacles:

$$\sigma^* = \sigma - \sigma_G, \quad (2.29)$$

where σ_G is the athermal (back) stress.

The observation of extrinsic grain boundary dislocations by transmission electron microscopy [78, 79] indicates that the extrinsic dislocations give rise to an athermal stress (also see section 2.1.2.2). According to [9, 10, 24, 26, 80], the athermal stress component σ_G resulting from dislocations within the grain and at the grain boundary can be expressed as

$$\sigma_G = \alpha M G b \sqrt{\rho_f + f_{\text{gb}} \rho_{\text{gb}}}, \quad (2.30)$$

where f_{gb} is a weighting factor accounting for the relaxation of the stress field of the extrinsic grain boundary dislocations.

Velocity of Jerky glide Dislocations may glide in a jerky manner in pure metals (class M) or in a viscous manner in alloy (class A) [103]. The current work considers only the jerky glide resulting from thermally activated overcoming of obstacles which are posed by forest dislocations. The kinetics of the thermally activated process has been thoroughly studied in [104]. Usually it is described by a sinh function:

$$v_g = f_{\text{mob}} \Delta x \nu_G \exp\left(-\frac{\Delta G_0}{k_B T}\right) \sinh\left(\frac{\sigma^* b \Delta a^*}{M k_B T}\right) \quad (2.31)$$

$$\Delta a^* = \Delta x \lambda, \quad (2.32)$$

where Δx is the width of obstacles (Fig. 2.10), ν_G is the attempt frequency, ΔG_0 is the free activation enthalpy of the thermal obstacles at $\sigma^* = 0$, Δa^* is the activation area [70, 82, 83], and λ (Fig. 2.10) is the spacing of thermal obstacles along the dislocation lines. As the dislocations do not move across high-angle grain boundaries, the dislocations stored at grain boundaries do not pose thermal obstacles. Then the obstacle spacing λ is solely related to the dislocations existing in grain interiors. Following a common approach it is chosen to be the average spacing of free dislocations δ [70]. See the preceding section (2.3.1) for the reason of the introduction of f_{mob} .

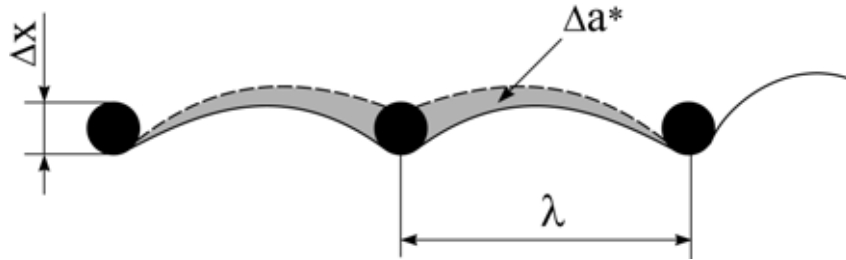


Figure 2.10: Schematic of the thermally activated process of a dislocation overcoming local obstacles. λ : the mean spacing of thermal obstacles along the dislocation line; Δx : the width of obstacle; shadowed area: the activation area.

2.4 Numerical implementation

The model presented in the current work is constructed in a general framework proposed by Sedláček and Blum [105] for developing microstructure based statistical dislocation models. From its logics, the model can be divided into several interconnected modules (Fig. 2.11).

The model is implemented in the programming language C to be able to incorporate an efficient solver (CVODE) for ODEs developed by Cohen and Hindmarsh [106]. The results

of integration are passed to the commercial mathematical software Mathcad² version 11 for various evaluations and preliminarily visualization.

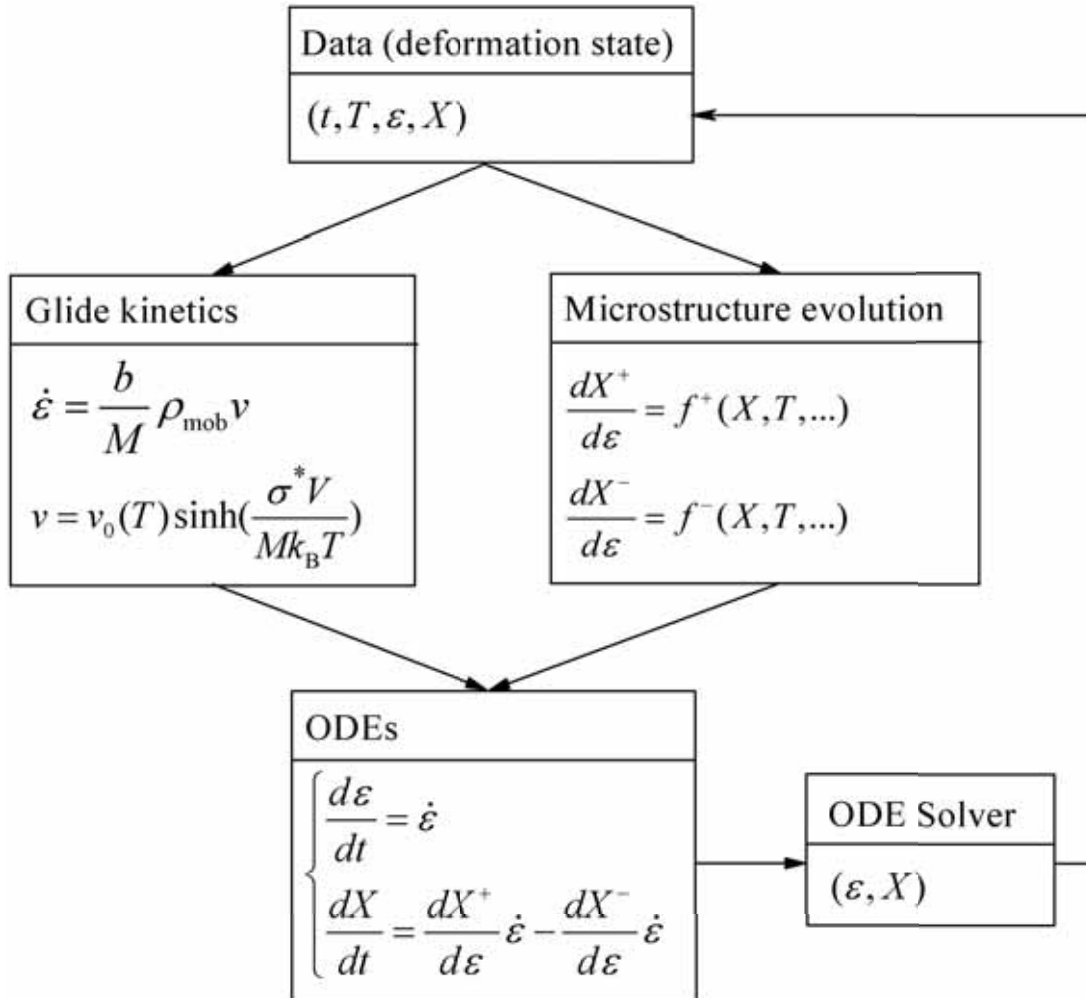


Figure 2.11: Logical structure of the model.

²Mathcad (from Mathsoft Engineering & Education, Inc., 101 Main Street, Cambridge, MA 02142-1521, USA).

3 Results

Contents

3.1	Parameter set and initial microstructural state	36
3.1.1	Material and model parameters	36
3.1.2	Integration conditions	37
3.2	Evolution of deformation resistance and microstructure with strain	37
3.3	Steady state deformation resistance	44
3.3.1	Deformation resistance	44
3.3.2	Stress components: ratio σ^*/σ	46
3.3.3	Dislocation density	47
3.3.4	Annihilation mechanism of grain boundary dislocations	49
3.4	Grain-size dependence of steady steady deformation resistance	51
3.4.1	Low temperature	51
3.4.2	High temperature	54
3.5	Simplified steady state solution for ufg materials	55
3.5.1	Hall-Petch relation at low homologous temperature	56
3.5.2	Grain boundary softening at elevated homologous temperature	56
3.6	Comparison with experimental observations	57

3.1 Parameter set and initial microstructural state

3.1.1 Material and model parameters

The material parameters and variables entering the current model are listed in Table 3.1 and 3.2, respectively.

parameter	value
b /nm	0.256 [12]
Ω /m ³	$1.18 \cdot 10^{-29}$ [12]
G /GPa	$42.1 \left(1 - 0.54 \frac{T/K - 300}{1356} \right)$ [12]
E /GPa	$118 \left(1 - 0.54 \frac{T/K - 300}{1356} \right)$
ν	0.34 [107] [12]
ν_G /s ⁻¹	10^{11} [104]
D_{sd} /m ² s ⁻¹	$2 \cdot 10^{-5} \exp \left(-\frac{197 \text{ kJ/mol}}{RT} \right)$ [12]
D_{gb} /m ² s ⁻¹	$5 \cdot 10^{-6} \exp \left(-\frac{104 \text{ kJ/mol}}{RT} \right)$ [12]

Table 3.1: Material parameters for Cu.

parameter	Cu	Eq.
M	3.06	(2.9)
α	0.2	(2.30)
$d_{\text{spon},f}$	$6b$	(2.16)
$d_{\text{spon},gb}$	$6b$	(2.24)
f_{mob}	10^{-4} [92]	(2.31)
ΔG_0 /eV	1.5	(2.31)
Δx	b	(2.31)
n_g	2	(2.16)
k_ρ	50	(2.10)
ξ	25 [70]	(2.20)
f_{dip}	1	(2.19)
f_{gb}	1	(2.30)

Table 3.2: Model variables.

3.1.2 Integration conditions

Deformation condition The calculations have been performed in the current work exclusively in the condition of strain controlled deformation where the total mechanical strain ϵ_{mech} increases with time at a constant prescribed strain rate. However, as demonstrated in [92], the choice of other deformation modes, *e.g.* stress controlled deformation condition (so-called creep) does not yield any difference in the steady state deformation resistance. In principle, the model can be applied to any deformation condition.

Initial condition The initial microstructural parameters chosen were shown in Table 3.3. The choice of the initial value of ρ_f is based on the microstructural observations done by Dalla *et al.* [108] for pure Cu after ECAP. The choice of the initial value of N_{gb} is arbitrary as there is no microstructural observation available. The value is chosen with considerations that the spacing of grain boundary dislocations is not larger than grain size and is not smaller than the critical distance for spontaneous annihilation occurring. The same initial values of dislocation densities are taken for cg Cu to facilitate direct comparisons in simulation results between cg and ufg Cu so that one can exclude possible differences in final results caused by different choices of initial values. Actually, the exact choice of these parameters is not important as the steady state deformation behavior is of major concern in the present work.

	ρ_f / m^{-2}	$N_{\text{gb}} / \text{m}^{-1}$	$d / \mu\text{m}$
value	10^{14}	10^8	$0.01 \sim 100$

Table 3.3: Initial state of microstructure.

3.2 Evolution of deformation resistance and microstructure with strain

Figs. 3.1 and 3.2 display examples of the evolution of stress and dislocation densities with strain for cg and ufg Cu at $\dot{\epsilon} = 10^{-3} \text{ s}^{-1}$ and 298 K, respectively. For the cg material ($d = 50 \mu\text{m}$), the generation of free dislocations in grain interiors is not affected by high-angle grain boundaries as the grain size d is distinctly larger than $\Lambda_\rho \approx 2 \mu\text{m}$ (derived from Eq. (2.10) and the density ρ_f shown in Fig. 3.1(b)) so that the grain-size dependent mean free path of free dislocations $\Lambda_{\rho,d}$ approximately equals the grain-size independent quantity Λ_ρ (Fig. 2.8). Thus the generation of free dislocations in the grain interiors is determined by the free dislocations themselves. Meanwhile, the generation rate of grain boundary dislocations is so small that the *total* rate of generation of dislocations virtually equals the rate of generation of free dislocations in grain interiors (Fig. 3.1(c)).

The areal density of grain boundary dislocations N_{gb} attains its maximum value close to $d_{\text{spont,gb}}$ as spontaneous annihilation prevails. However, the large d translates N_{gb} into a rather small ρ_{gb} (Eq. (2.4)) compared to ρ_f so that the deformation resistance is mostly determined by the free dislocations within the grain interior through contributing to athermal as well as effective stress (see Fig. 3.1(b)). In the current case of high stress, the glide of dislocations controls not only the rate of generation of dislocations, but also the rate of loss of dislocations by spontaneous annihilation (Fig. 3.1(b)-(c)).

For ufg material ($d = 0.2 \mu\text{m}$) at the same condition, the grain-size independent mean free path of free dislocations Λ_ρ becomes larger than the grain size d so that free dislocations are able to leave from grain interiors and arrive at grain boundaries. Consequently, the grain-size dependent mean free path of free dislocations $\Lambda_{\rho,d}$ becomes larger than Λ_ρ and d and increases in proportion to δ^2 with increasing δ (Fig. 2.8). Accordingly, the rate of generation of free dislocations is slowed down (see Fig. 3.2(c)). The mean free path $\Lambda_{\rho,d}$ at $d = 0.2 \mu\text{m}$ lies in the left region of Fig. 2.8 where the rate of generation of free dislocations is larger than the rate of spontaneous annihilation. The result is a continuous decrease of density ρ_f (see Fig. 3.2(b)-(c)). The density ρ_f may decrease too low so that the spacing between thermal obstacles becomes too large, even larger than the grain size. This may indicate that i) thermal obstacles become unimportant for ufg materials; ii) that the density of mobile dislocations which produce strain is underestimated (see section 4.4 for further discussions). Presently the density of mobile dislocations is treated to equal the density of free dislocations in grain interiors. And we do not consider those dislocations which also produce strain before they get stored at grain boundaries. That means the density of mobile dislocations may become larger than the density of free dislocations in grain interiors if we count those dislocations which ever produced strain as mobile ones before they arrive at grain boundaries. In any case, when the grains become very small there is no accumulation of dislocations within the grains any more as dislocations can reach the next-neighbouring grain boundary before getting stored in the grain interior.

In contrast to the rate of generation of free dislocations the total generation rate is enhanced in the ufg case (Figs. 3.2(c)) compared to the cg case (Figs. 3.1(c)) as grain size d as well as Λ_{tot} is decreased. The generated dislocations are mainly stored at grain boundaries. Since the annihilation of grain boundary dislocations is not very efficient at the present simulation condition (low temperature and high strain rate), the steady state density ρ_{gb} remains at a rather high level (Fig. 3.2(b)). The high density ρ_{gb} compared to the density ρ_f in the cg case (Fig. 3.1(b)) causes the ufg material to have higher steady state deformation resistance than the cg material. This means that the ufg material is strengthened by the grain boundary dislocations at low temperature and high strain rate. The effective stress becomes negligible. This is due to disappearance of thermal obstacles in consequence of decreasing density of free dislocations in grain interiors (see Fig. 3.2(a)).

At elevated temperature of 418 K and a low strain rate $\dot{\epsilon} = 10^{-8} \text{ s}^{-1}$, for cg material, the mean free path of free dislocations holds a value of about $2 \mu\text{m}$ similar to the low temperature case. Thus it is still distinctly smaller than d . Consequently, the deforma-

tion is still dominated by the free dislocations in grain interiors. The thermally activated annihilation of free dislocations becomes competitive, but is still less efficient than spontaneous annihilation (Fig. 3.3(c)). However, for grain boundary dislocations, the thermally activated climb process now becomes dominant in annihilation. This is due to the fact that the diffusion process is more efficient at grain boundaries than in grain interiors.

The same situation of annihilation of grain boundary dislocations being dominated by dislocation climb is found in the ufg material (Fig. 3.4(c)) at the same deformation conditions. As in the case of low temperature, the grain interior becomes free from dislocations, and the storage rate of grain boundary dislocations is enhanced due to the small d (Fig. 3.4(c)). However, as the high rate of annihilation by climb reduces the level of density ρ_{gb} below that which would be necessary for purely spontaneous annihilation as in the low temperature case (Fig. 3.2(c)), the ufg material loses strength. This means that the ufg material is softened by the fast annihilation of grain boundary dislocations at high temperature and low strain rate.

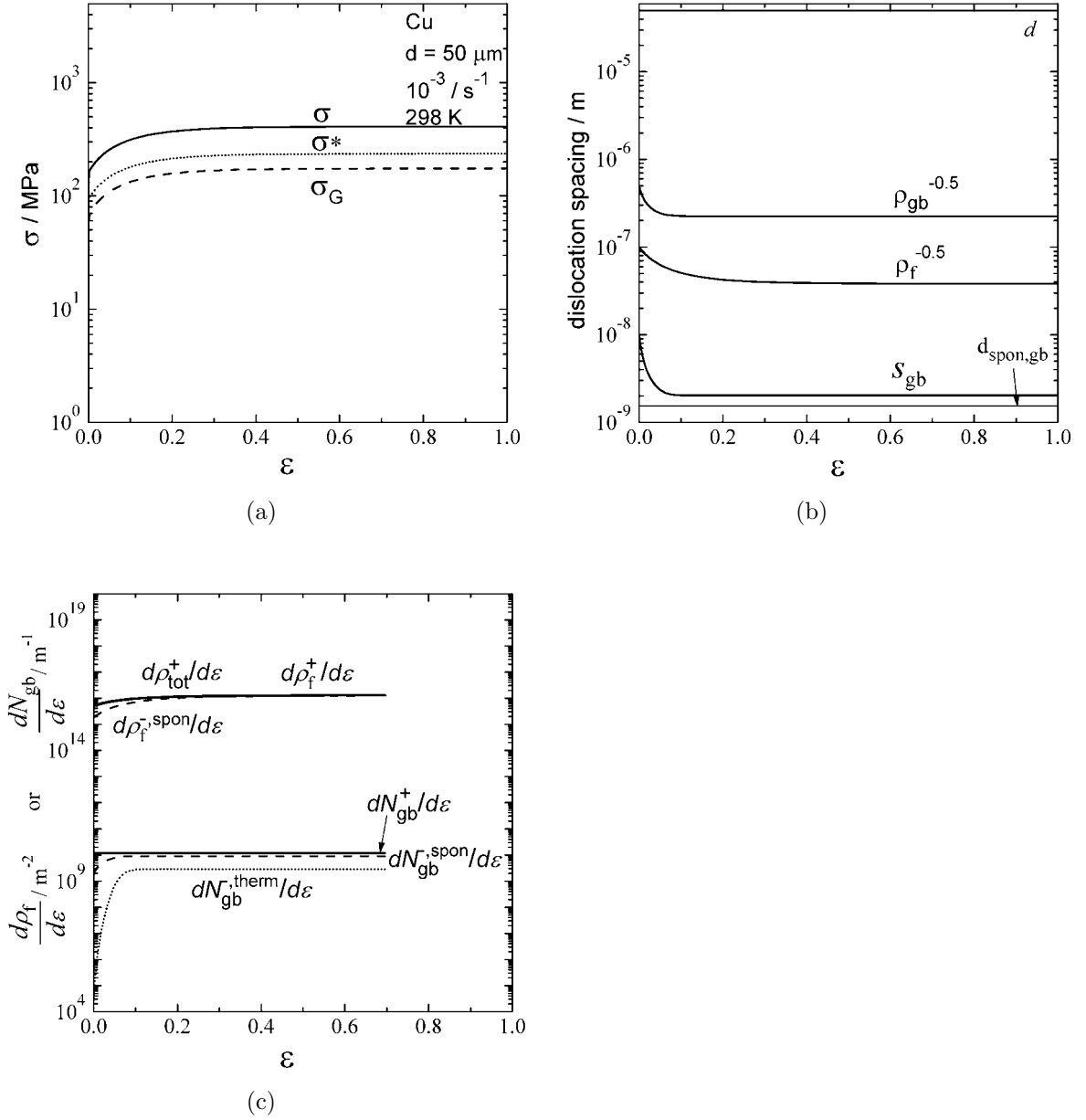


Figure 3.1: Example of curves for the evolution of stress and dislocation densities with strain for cg ($d = 50 \mu\text{m}$) at 298 K. (a) flow stress σ , athermal stress σ_G , and effective stress: σ^* ; (b) dislocation spacing $\rho_f^{-0.5}$, $\rho_{\text{gb}}^{-0.5}$ and s_{gb} . The quantities d and d_{spon} are the grain size and the critical spacing for spontaneous annihilation, respectively. (c) rates of evolution of dislocation density. Deriving from Eq. (2.15) the total rate of generation of dislocations $d\rho_{\text{tot}}^+/d\epsilon$ equals $d\rho_f^+/d\epsilon + dN_{\text{gb}}^+/d\epsilon \cdot 2/d$.

3.2 Evolution of deformation resistance and microstructure with strain

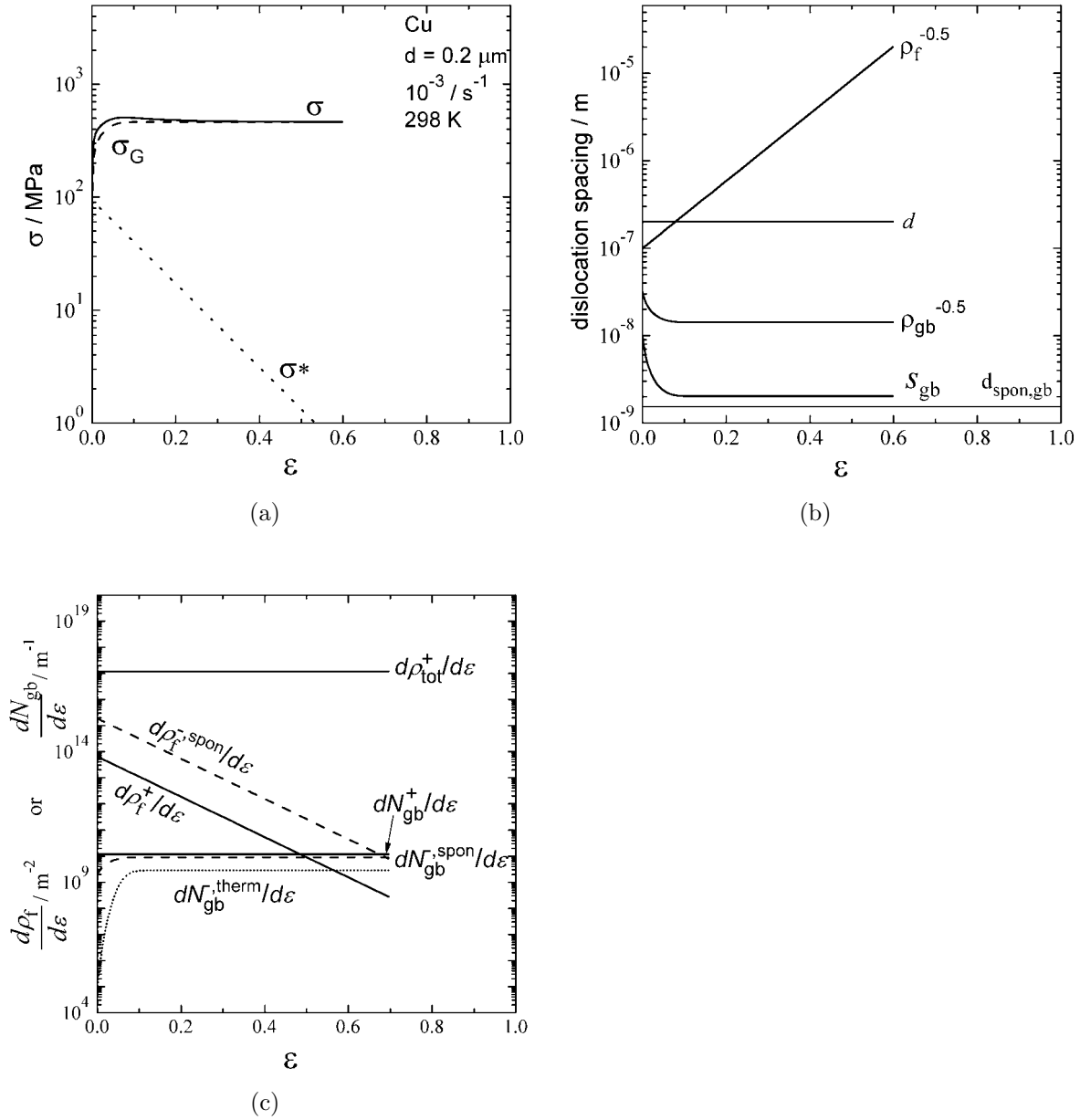


Figure 3.2: As Fig. 3.1 for ufg Cu.

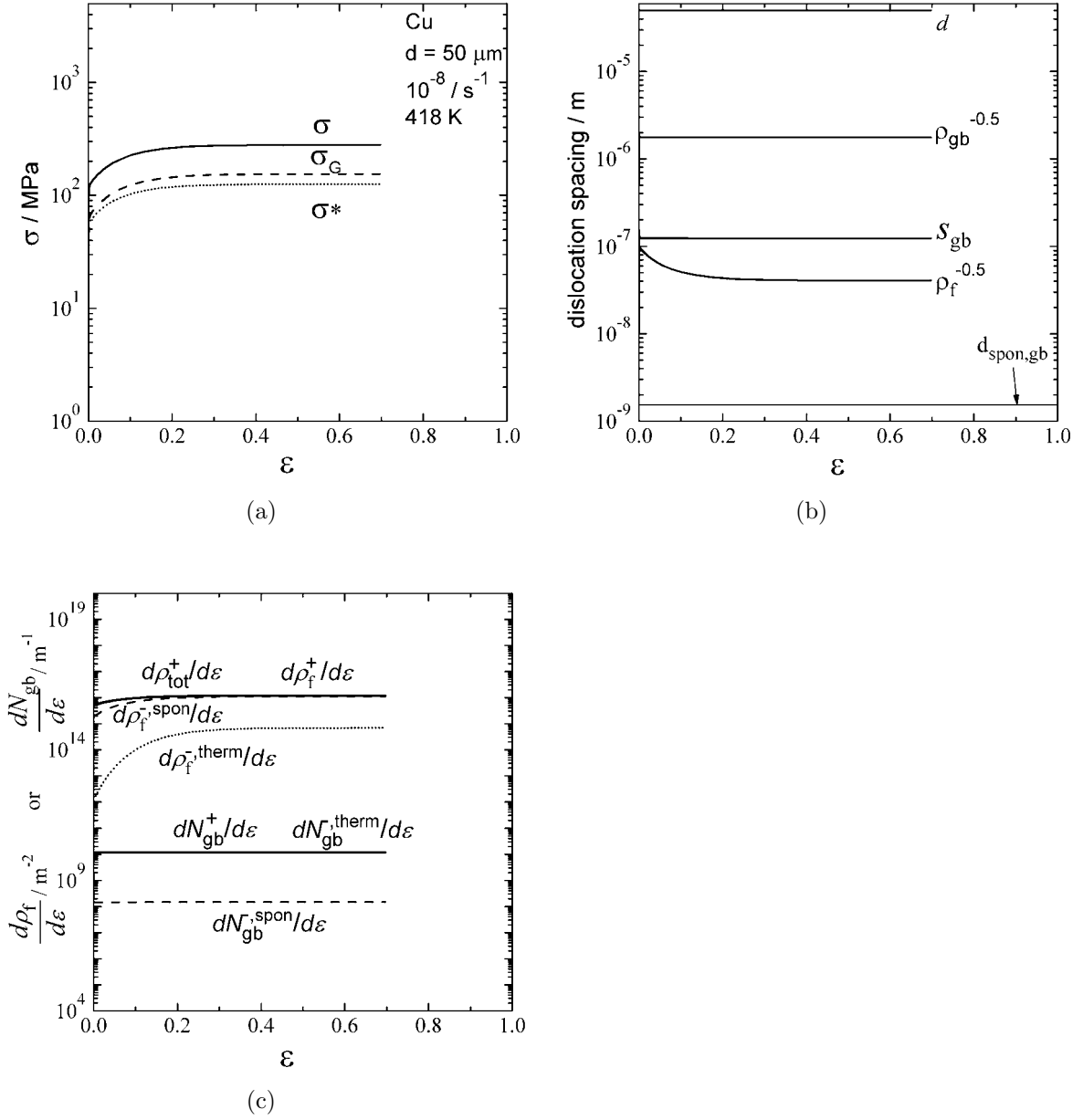


Figure 3.3: As Fig. 3.1 for 418 K.

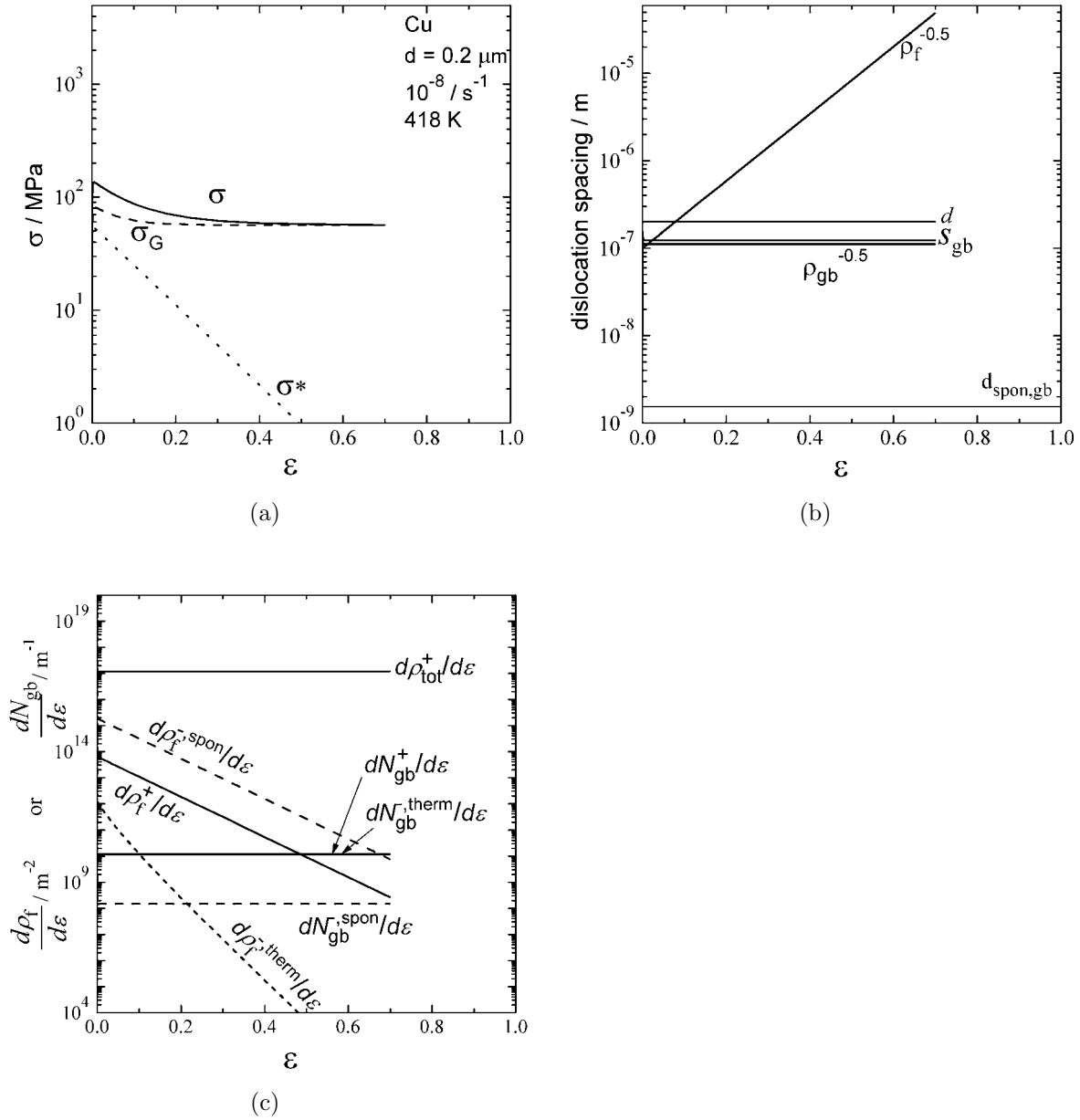


Figure 3.4: As Fig. 3.2 for 418 K.

3.3 Steady state deformation resistance

3.3.1 Deformation resistance

Figure 3.5 shows the relation between steady state stresses and strain rate for cg and ufg Cu resulting from simulations at 298 and 418 K. In both kinds of material the calculated

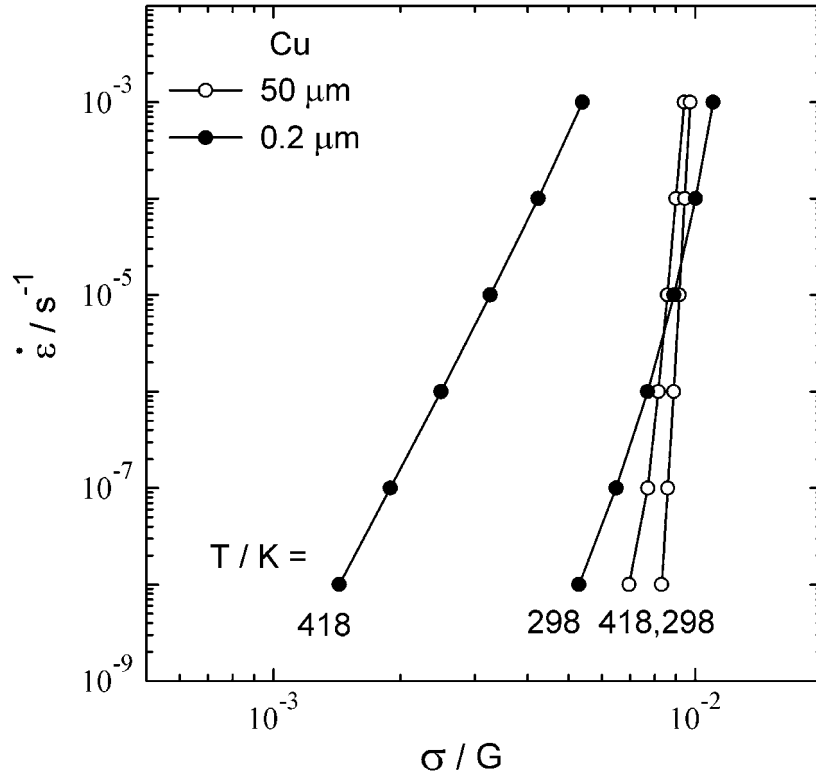


Figure 3.5: Calculated steady state deformation resistance of cg (grain size $d = 50 \mu\text{m}$) and ufg ($d = 0.2 \mu\text{m}$) at 298 and 418 K. Simulations were done at strain rates ranging from 10^{-3} to 10^{-8} s^{-1} separated by one order of magnitude. Open and full Circles mark strain rates at the shear modulus normalized stress σ/G for cg and ufg Cu, respectively.

steady state flow stress decreases with increasing temperature and/or decreasing strain rate. However, the dependence of stress on temperature and strain rate is stronger for ufg than for cg Cu as shown in Figs. 3.5 and 3.6. At the lower temperature of 298 K, the significant difference in strain rate sensitivities of flow stress causes a crossover of the curves for the steady state stress of ufg and cg Cu. This means that the ufg Cu becomes softer than the cg Cu at low strain rates. At the elevated temperature of 418 K the ufg Cu is softer than its cg variant even at high strain rates in the steady state of deformation.

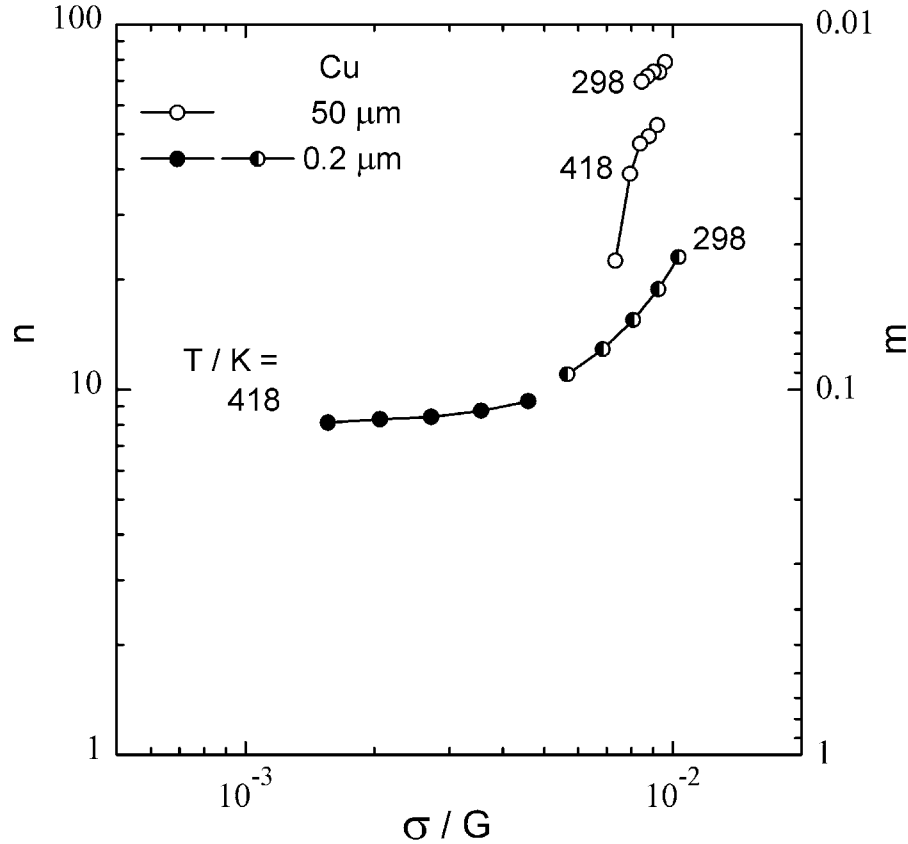


Figure 3.6: Stress exponent $n \approx \Delta \ln \dot{\epsilon} / \Delta \ln \sigma$ (derived from neighbouring points of Fig. 3.5) of the steady state deformation rate and strain rate sensitivities $m = 1/n$ of the steady state flow stress as function of shear modulus normalized stress.

For cg material the $\dot{\epsilon}$ - σ relations at low and high temperature are similar. This is due to the fact that spontaneous annihilation of free dislocations prevails in grain interiors (Fig. 3.1(c) and 3.3(c)) at both temperatures. This causes most n -values (derived from Fig. 3.5) to be larger than 40 (Fig. 3.6). The strong decrease of n with decreasing stress at 418 K is due to the fact that the thermally activated annihilation process becomes competitive so that the annihilation process is accelerated (Fig. 3.4(c)).

For ufg Cu the reduction in n -value from a relatively high value of 20 to 8 is due to a gradual shift in the most effective annihilation mechanism from spontaneous annihilation which prevails at high strain rate and low temperature to dislocation climb at low strain rate and/or high temperature (Fig. 3.2(c) and 3.4(c)). This transition in the annihilation mechanism leads to a transition from strengthening to softening in ufg material.

In the following sections we shall explain why ufg Cu has such unusual properties. We shall start with analyzing the stress components and dislocation densities of ufg as well as

cg Cu.

3.3.2 Stress components: ratio σ^*/σ

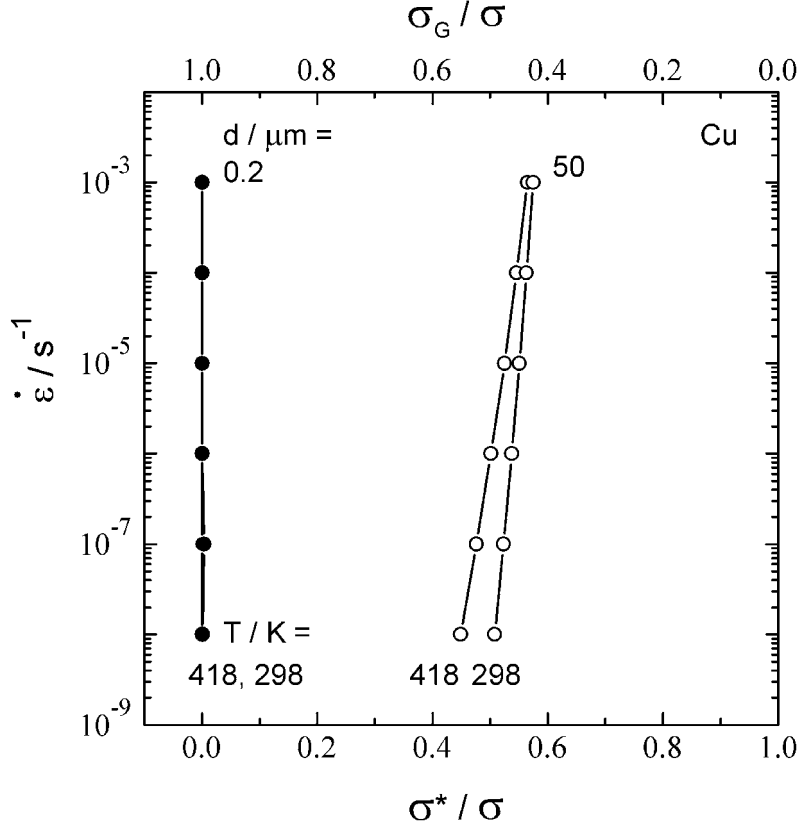


Figure 3.7: σ^*/σ versus $\dot{\epsilon}$ in steady state deformation of cg and ufg Cu at 298 and 418 K.

Figure 3.7 displays the strain rate dependent steady state ratios σ^*/σ and σ_G/σ obtained from the simulations. For cg Cu σ^*/σ lies in the range of $0.4 \sim 0.6$. At ambient temperature the effective stress is larger than the athermal stress. The high effective stress is required to transport dislocations which end their lives by spontaneous annihilation. The decrease in σ^*/σ (or increase in σ_G/σ) indicates that the thermally activated annihilation of dislocations becomes progressively important compared to the spontaneous annihilation. This can be seen by comparing Fig. 3.1 to 3.3.

For ufg Cu, the effective stress is negligible because thermal obstacles are no longer existing as the density of free dislocations in the grain interior is negligible (*e.g.* see Figs. 3.2(b) and 3.4(b)).

Summary In the simulated range of strain rates, for cg material the athermal stress and effective stress both make significant contributions to the steady state flow stress; for ufg material, only the athermal stress contributes to the steady state flow stress.

3.3.3 Dislocation density

In this section we shall analyze which kind of dislocation contributes to the applied stress and its components in each kind of material.

Figures 3.8 and 3.9 display the average spacing of grain boundary dislocations, quantified by s_{gb} (derived from Eq. (2.6)) and $\rho_{gb}^{-0.5}$, and the average spacing of free dislocation $\rho_f^{-0.5}$ (derived from Eq. (2.4)) for cg and ufg Cu, respectively.

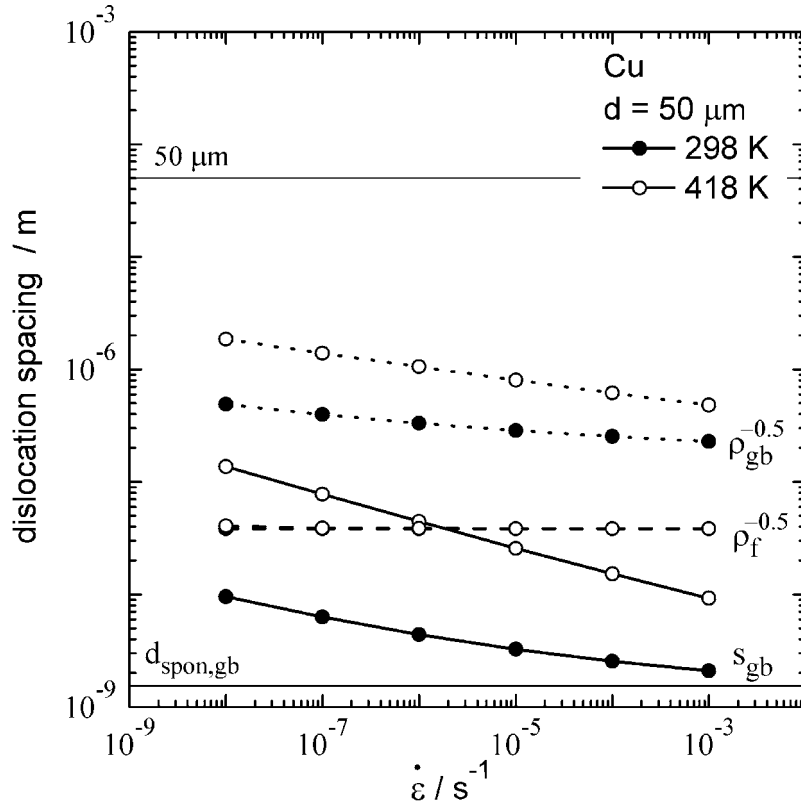


Figure 3.8: Strain rate dependence of dislocation spacings for cg Cu at 298 and 418 K. The horizontal lines mark $d_{\text{spon,gb}}$ and the grain size.

By comparing Fig. 3.8 and 3.9 it is found that the spacing s_{gb} is independent of grain size d . This means that the cg and ufg material have the same areal density of grain boundary dislocations N_{gb} . This is due to the fact that the evolution of N_{gb} (see Eqs. (2.13), (2.24)

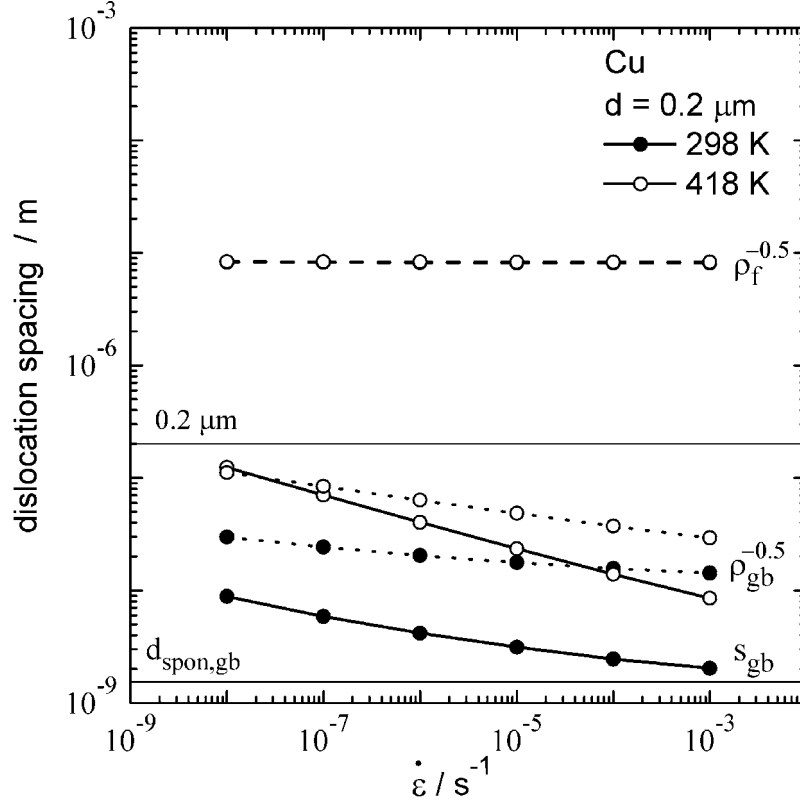


Figure 3.9: As Fig. 3.8 for ufg Cu. The densities ρ_f are obtained from the calculations at $\epsilon = 0.5$ where the flow stresses have already saturated.

and (2.25)-(A.37)) is independent of grain size. However, the geometric factor $2/d$ (grain boundary area per volume) transforms N_{gb} into the grain-size dependent quantity ρ_{gb} (see Eq. (2.4)).

For cg material, as stated before (see Figs. 3.1 and 3.3), generation of ρ_f is not affected by high-angle grain boundaries. The density ρ_f is distinctly larger than the density ρ_{gb} so that the deformation resistance is mainly determined by the free dislocations in grain interiors through contributing to athermal as well as effective stress (Fig. 3.7).

For ufg material, as the small grains can hardly accommodate the storage of free dislocations in their interiors, dislocations are mainly stored at high-angle grain boundaries. Thus the density ρ_{gb} determines the athermal stress and the applied stress.

At ambient temperature the increase of s_{gb} with decreasing $\dot{\epsilon}$ indicates the transition in the most effective annihilation mechanism from spontaneous annihilation to thermally activated annihilation. At elevated temperature the relation $\dot{\epsilon} \propto N_{gb}^4$ is found (see Fig. 3.9). See section 3.5.2 for detailed derivation of this relation.

3.3.4 Annihilation mechanism of grain boundary dislocations

Figures 3.10 and 3.11 illustrate the steady state rates of the generation and annihilation of grain boundary dislocations resulting from the present simulations at 298 K and 418 K, respectively.

In any case the easier annihilation process controls the loss of dislocations. At low temperatures and high strain rates, in order for spontaneous annihilation to occur, the dipole spacings $d_{\text{dip,gb}}$ must be less than $d_{\text{spon,gb}}$. This requires high stresses to produce dislocations. When the flow stress is high enough, spontaneous annihilation occurs along with glide and balances dislocation generation. In this situation glide is the only process controlling not only the rate of generation, but also the rate of annihilation of dislocations. At low strain rate and high temperature climb-controlled annihilation becomes competitive. It allows dipoles with $d_{\text{dip,gb}} > d_{\text{spon,gb}}$ to disappear. In this case annihilation is no longer a byproduct of glide but depends on an independent process. The high rate of annihilation by climb reduces the level of flow stress below that which would be necessary for purely spontaneous annihilation.

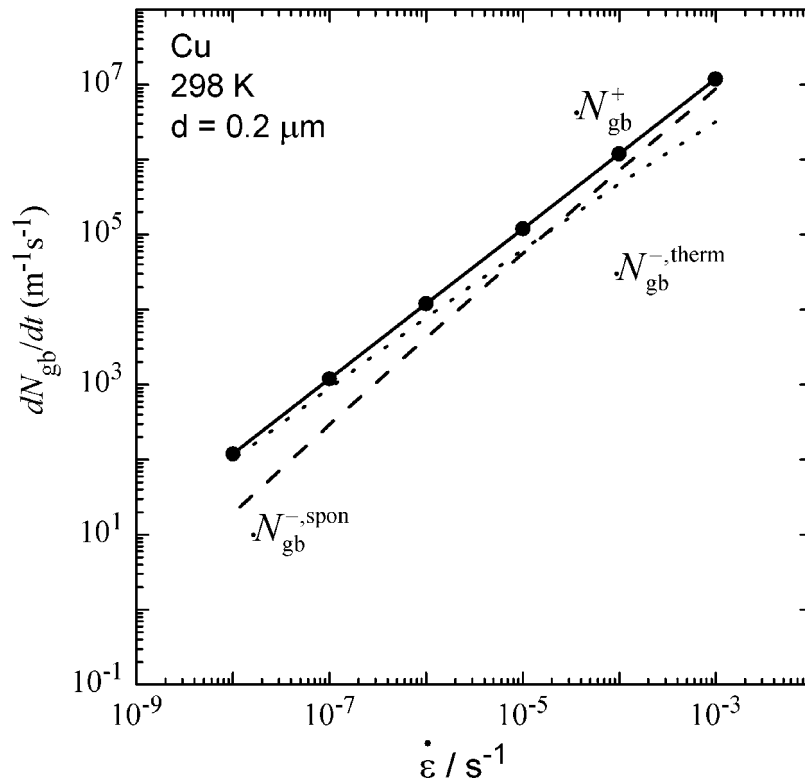


Figure 3.10: Rates of generation and annihilation of grain boundary dislocations as function of strain rate at 298 K.

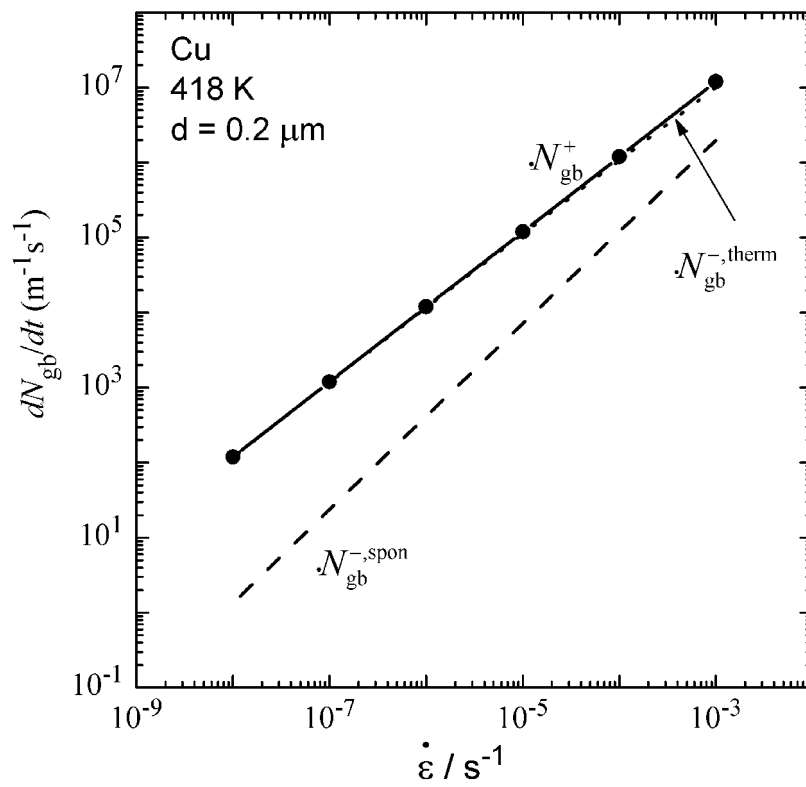


Figure 3.11: As Fig. 3.10 for 418 K.

3.4 Grain-size dependence of steady steady deformation resistance

To analyze the influence of grain size d on the steady state deformation resistance, besides the simulations performed for the two kinds of materials in the previous sections, additional calculations were done for different modeled materials of different grain sizes.

3.4.1 Low temperature

Fig. 3.12 displays the steady state deformation resistance resulting from the simulations for ambient temperature as function of grain size. The newly calculated curves with $d \leq 1 \mu\text{m}$ have a same shape as the curve calculated for the ufg Cu with $d = 0.2 \mu\text{m}$ indicating that grain boundary dislocations dominate the deformation resistance in the materials modeled. With d decreasing from the size of ufg regime further into nano regime, the curves shift to the right in proportion to $d^{-0.5}$ (see Fig. 3.12). This phenomenon of hardening by fine grains is related to the fact that the rate, at which dislocations are stored at the boundaries, increases with decreasing d (see Eq. (A.19)).

The modeled materials with $d = 0.35 \mu\text{m}$ and $1 \mu\text{m}$ are softer than the cg material even at high plastic strain rate of 10^{-3} s^{-1} at room temperature. To understand the reason behind this observation, more simulations were done for a wide range of grain size $0.01 \leq d/\mu\text{m} \leq 100$ at constant plastic strain rate of $10^{-3} /\text{s}$. Figure 3.13(a) displays the steady state stress as a function of $d^{-0.5}$; the corresponding steady state dislocation densities are shown in Figure 3.13(b). The difference between the flow stress σ and the athermal stress σ_G gives the effective stress σ^* . As the deformation rate is high and the temperature is low, spontaneous annihilation dominates the loss of grain boundary dislocations so that the areal density N_{gb} remains independent of d .

In the regime of large grain size the grain-size dependent mean free path of free dislocations $\Lambda_{\rho,d}$ is distinctly smaller than the grain size (Fig. 3.14(b)). Thus $\Lambda_{\rho,d}$ reduces to the grain-size independent quantity Λ_ρ of about $2 \mu\text{m}$. This means that high-angle grain boundaries do not affect the evolution of ρ_f . The deformation resistance is dominated by the free dislocations in grain interiors. For detailed informations of the evolution of stress and dislocation densities with strain, see the examples shown in Fig. 3.1. When the grain size approaches Λ_ρ , the fraction of free dislocations, which are able to reach high-angle grain boundaries, begins to rise significantly. This leads $\Lambda_{\rho,d}$ to deviate from Λ_ρ and increase. With further decrease of d below Λ_ρ , more and more dislocations reach grain boundaries; thus $\Lambda_{\rho,d}$ increases further (Fig. 3.14). Consequently ρ_f decreases (Fig. 3.13(b)), which in turn leads to a decrease in athermal stress (see $\sigma_{G,f}$ in Fig. 3.13(a)) as well as effective stress produced by the free dislocations in grain interiors. In contrast to the decrease of ρ_f with decreasing d , the average volume density of grain boundary dislocations ρ_{gb} following from the areal density N_{gb} increases with decreasing d . When the density ρ_f becomes significantly smaller than ρ_{gb} , the flow stress is determined by the grain boundary disloca-

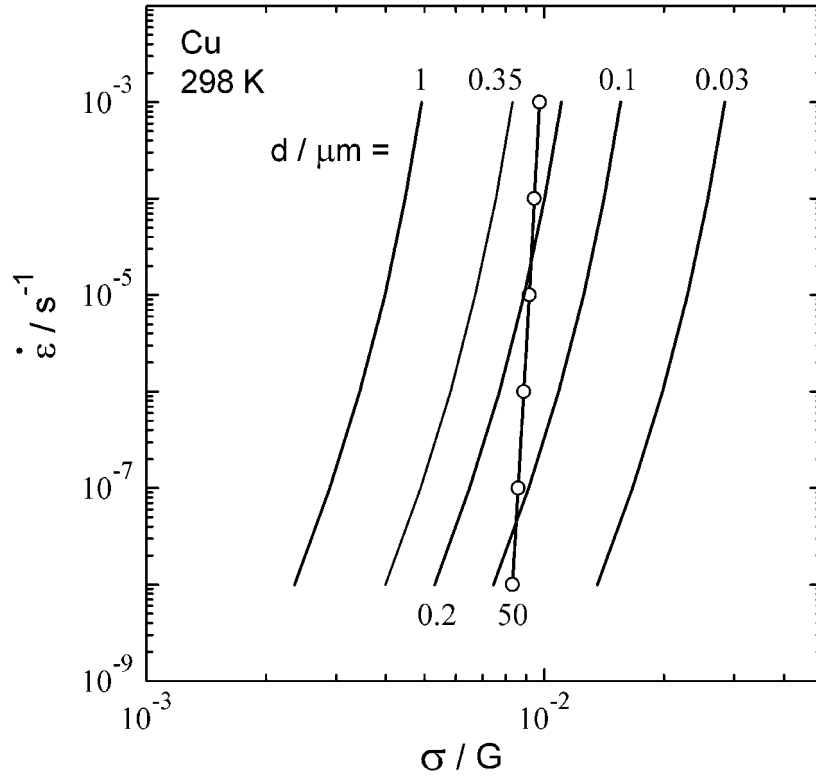


Figure 3.12: Steady state deformation resistance $\dot{\epsilon}-\sigma$ of pure Cu at room temperature calculated from the model as function of grain size.

tions where $\sigma \approx \sigma_G \approx \sigma_{G,gb}$. Thus the Hall-Petch relationship between σ and $d^{-0.5}$ results.

In the vicinity of $d = 4 \mu\text{m}$ the flow stress displays a relative minimum. This grain size corresponds to a radius of the average grain cross section r' to be $2.5 \mu\text{m}$, which is very close to Λ_ρ at the given deformation condition. The small grain size, on the one hand, leads to a tendency of decreasing the deformation resistance as free dislocations are lost in the grain interior by reaching high-angle grain boundaries; on the other hand, the volume density ρ_{gb} stored at grain boundaries becomes very high causing the athermal stress component to increase strongly. However, when the density ρ_{gb} is not sufficiently high to compensate the loss of strengthening by free dislocations contributing to athermal as well as effective stress, the deformation resistance is reduced. This explains the relative minimum of flow stress.

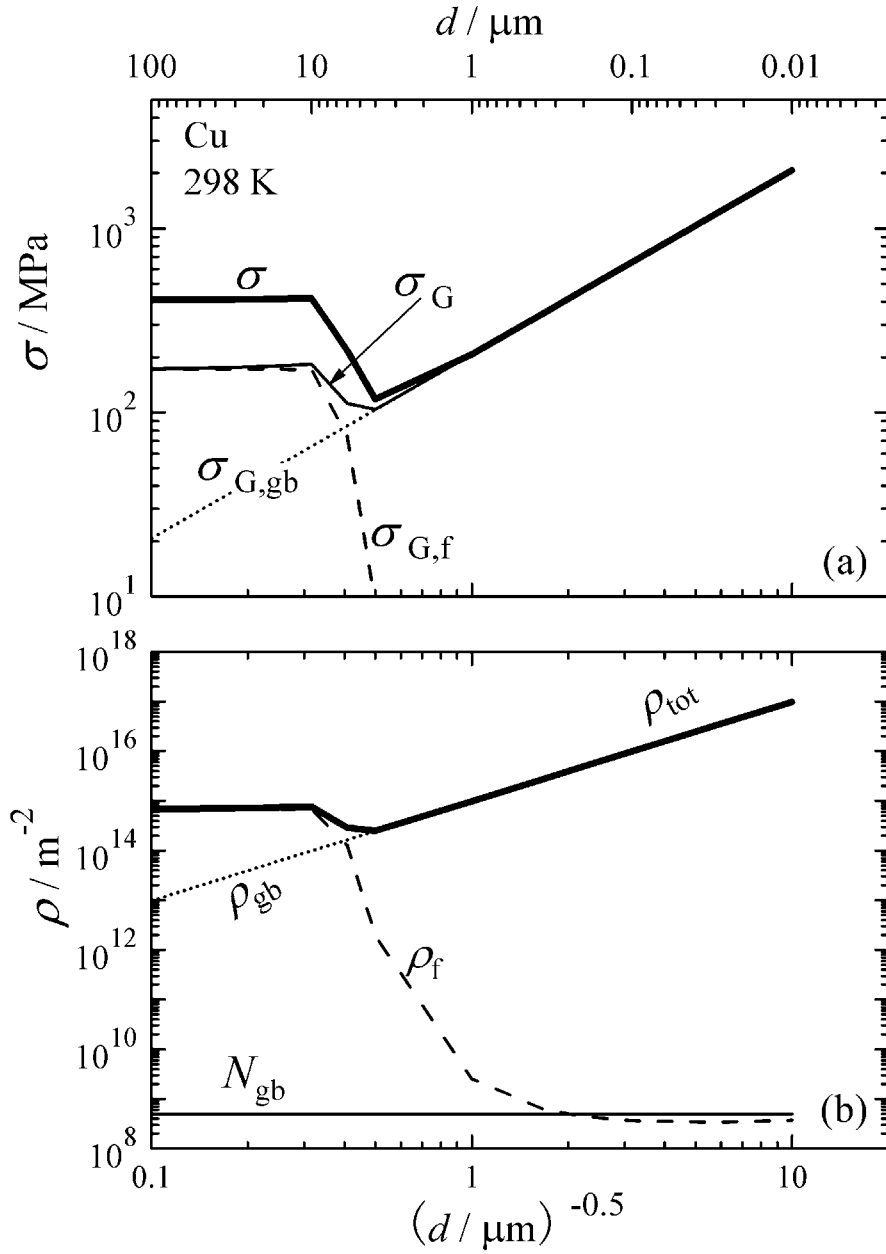


Figure 3.13: Steady state stresses and dislocation densities as function of grain size at ambient temperature and $\dot{\epsilon} = 10^{-3} \text{ s}^{-1}$ for Cu. (a) stress σ and athermal stress components; σ_G : total athermal stress (Eq. (2.30)); $\sigma_{G,gb} = \alpha M G b \sqrt{f_{gb} \rho_{gb}}$ and $\sigma_{G,f} = \alpha M G b \sqrt{\rho_f}$ characterize the athermal stress contributions due to ρ_{gb} and ρ_f alone. (b) dislocation densities; $\rho_{tot} = \rho_f + \rho_{gb}$ is the total dislocation density. The density ρ_f is obtained from the calculations at $\epsilon = 0.5$.

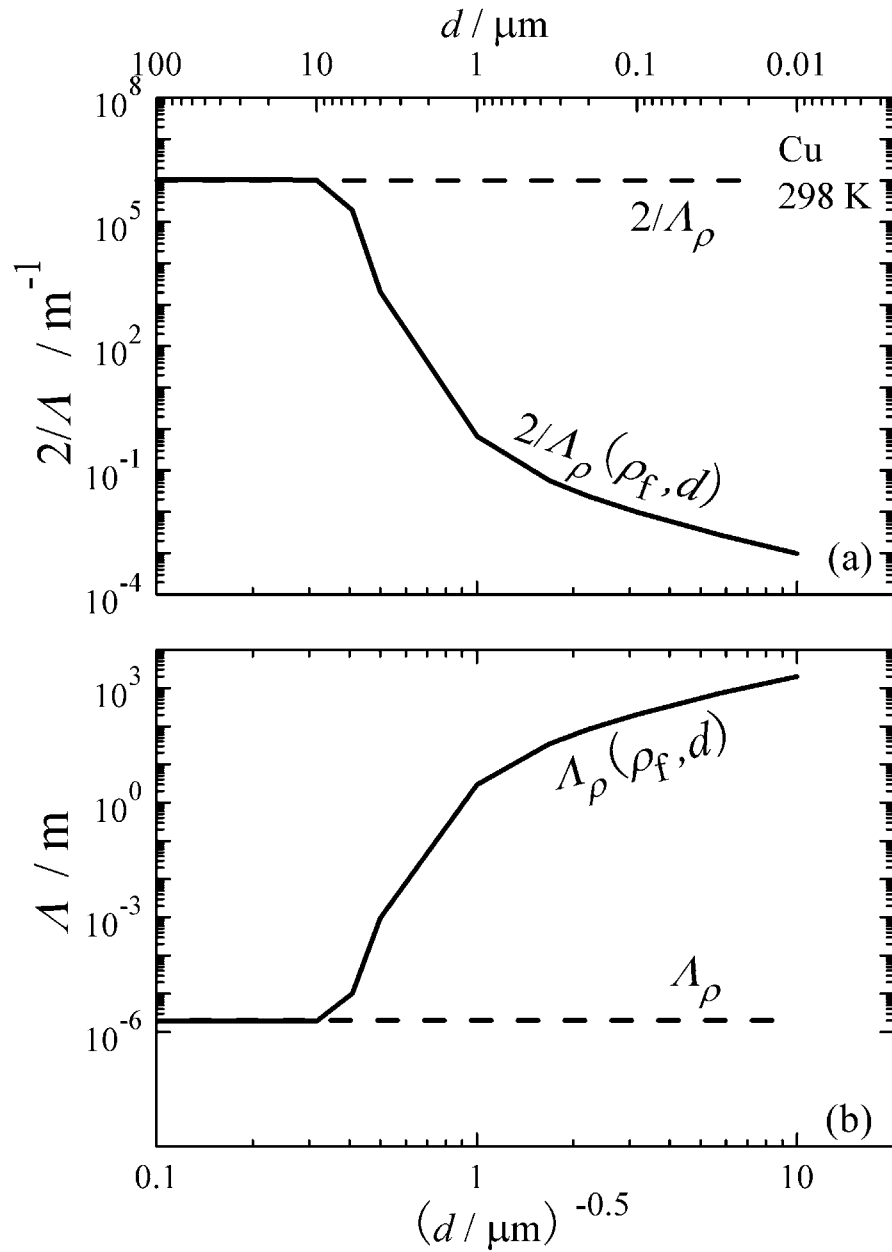


Figure 3.14: (a) Stored dislocation length per slipped area in the grain interior and (b) mean free path of free dislocations as function of $d^{-0.5}$. Data are derived from Fig. 3.13(b).

3.4.2 High temperature

Fig. 3.15 displays the steady state deformation resistance resulting from the simulations at elevated temperature as function of grain size. Due to the enhancement in the rate of thermally activated annihilation of grain boundary dislocations, the softening compared to cg material even becomes visible in the modeled nanocrystalline material with $d =$

0.03 μm . The curves for $d = 0.1 \mu\text{m}$ and $0.03 \mu\text{m}$ do not extend into the field of even lower strain rates is to prevent the spacing of grain boundary dislocations from exceeding the grain size.

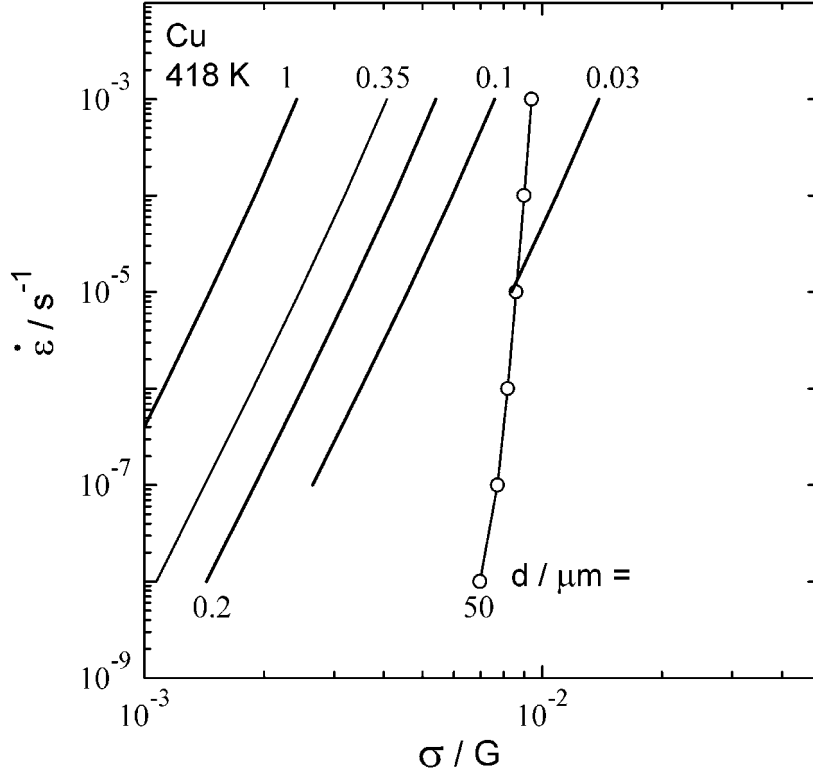


Figure 3.15: Steady state deformation resistance $\dot{\epsilon}-\sigma$ of pure Cu at elevated temperature of 418 K calculated from the model as function of grain size.

3.5 Simplified steady state solution for ufg materials

Based on the results shown in the previous sections, a simplified steady state solution can be derived for ufg and nano material by neglecting the density of free dislocations in grain interior ρ_f as it is negligible compared to the density of grain boundary dislocations ρ_{gb} . The flow stress can thus be modified as

$$\sigma \approx \sigma_G \approx \alpha M G b \sqrt{f_{gb} \rho_{gb}}. \quad (3.1)$$

In the following two simplified steady state solutions for low temperature and elevated temperature will be derived, respectively.

3.5.1 Hall-Petch relation at low homologous temperature

In the low temperature case loss of dislocations during deformation is mainly controlled by spontaneous annihilation. Saturation is attained by equating the rates given in (2.13) and (2.24). This yields the steady state value of $N_{\text{gb},\infty}$ as

$$N_{\text{gb},\infty} = \frac{n_{\text{gb}}}{2 d_{\text{spon,gb}}} . \quad (3.2)$$

Combining Eqs. (2.4), (3.1) and (3.2) yields

$$\sigma = \alpha M G b \sqrt{\frac{f_{\text{gb}} n_{\text{g}}}{d_{\text{spon,gb}}}} d^{-0.5} . \quad (3.3)$$

This formula reproduces the Hall-Petch hardening (1.1) with

$$k_{\text{HP}} = \alpha M G b \sqrt{\frac{2 f_{\text{gb}} n_{\text{g}}}{d_{\text{spon}}}} . \quad (3.4)$$

3.5.2 Grain boundary softening at elevated homologous temperature

At elevated temperature climb facilitates annihilation of edge dislocations at grain boundaries. A complete expression of the rate of thermally activated dislocation annihilation $\dot{N}_{\text{gb}}^{-,\text{therm}}$ can be derived based on the equations given in section 2.2.2.2. As the diffusion of atoms along grain boundaries dominates the climb of dislocations, the second term of Eq. (2.27) which accounts for the contribution to dislocation climb by diffusion of vacancies through the lattice can be neglected. In addition, as the dipole separation $d_{\text{dip,gb}}$ becomes distinctly larger than $d_{\text{spon,gb}}$, it is also possible to ignore $d_{\text{spon,gb}}$ from Eqs. (2.26). With this simplifications and combining Eqs. (2.25) to (2.27), (2.3) and (2.6) yields:

$$\dot{N}_{\text{gb}}^{-,\text{therm}} = \frac{8}{\pi (1 - \nu)} \frac{G \Omega}{k_{\text{B}} T} \delta_{\text{gb}} D_{\text{gb}} N_{\text{gb}}^4 . \quad (3.5)$$

Equating the rate of dislocation generation (Eq. (2.13)) to the rate of dislocation annihilation (Eq. (3.5)) yields the steady state grain boundary dislocation density:

$$N_{\text{gb},\infty} = \left[\frac{16 k_{\text{gb}} b}{\pi (1 - \nu)} \frac{G \Omega}{k_{\text{B}} T} \delta_{\text{gb}} D_{\text{gb}} \right]^{-\frac{1}{4}} \dot{\gamma}^{\frac{1}{4}} . \quad (3.6)$$

Combining Eqs. (2.4), (3.1) and (3.6) leads to the $\dot{\gamma}$ - τ relation in the saturation state as

$$\dot{\gamma} = C d^4 \frac{G \Omega}{k_{\text{B}} T} \cdot \frac{\delta_{\text{gb}} D_{\text{gb}}}{b^7} \cdot \left(\frac{\tau}{G} \right)^8 , \quad (3.7)$$

where

$$C = \frac{k_{\text{gb}}}{\alpha^8 f_{\text{gb}}^4 \pi (1 - \nu)} . \quad (3.8)$$

The results calculated by the simplified equations (Eqs. (3.3) and (3.7)) and the results calculated by the complete model outlined in section 2 will be compared in the next section.

3.6 Comparison with experimental observations

Fig. 3.16 shows the room temperature data from Fig. 1.2 together with the model line. The flow stress predicted by Eq. (3.3) is slightly higher than the flow stress calculated by the complete model. This is due to the neglect of thermally activated annihilation in deriving Eq. (3.3) (see section 3.5.1). For the cg Cu with $d \leq 10 \mu\text{m}$, the modeled steady state stress well agrees to the experimental findings. In the grain size range of $d \leq 0.1 \mu\text{m}$ the model overestimates the hardening effect. Three reasons may be responsible for that. First, the measured σ -data for nano Cu produced without severe plastic deformation are too low, as work hardening is not yet complete at the strain applied in nanoindentation in the equivalent normal strain of about 10~20%. Second, the dislocation interaction constant $\alpha = 0.2$ which is typical for lattice dislocations [69], may be too high for extrinsic grain boundary dislocations as the relaxation of the dislocation line energy and stress field by the grain boundaries is neglected. Although the weighting factor f_{gb} has been introduced to account for the relaxation of the stress field of grain boundary dislocations, presently, in the present calculations, the choice of $f_{\text{gb}} = 1$ does not alter α . Third, grain boundary sliding, which has not been considered in the model, may increasingly reduce the gain of strength with decreasing d in the nano regime. In the grain size range of $0.1 < d / \mu\text{m} < 10$, the modeled materials show lower steady state stress compared to the cg material at room temperature and high strain rate. Due to lack of experimental data in this range of grain size comparison is not possible. One must also take into account that polycrystals always contain a rather broad mixture of grain sizes which does not allow to observe the minimum.

Fig. 3.17 displays the comparison of simulated and experimental deformation resistance of cg ($d = 50 \mu\text{m}$) and ufg ($d = 0.35 \mu\text{m}$) Cu in the steady state using the temperature normalization described in section 1.1.

The simulation agrees reasonably well with the experimental findings at ambient and elevated T in the case of cg Cu. For the ufg material, only qualitative consistency emerges in that the relative softening of ufg compared to cg Cu increases with increasing T (or decreasing $\dot{\epsilon}$) as seen from the sequence of simulation results at elevated T . The model overestimates the softening at both low and elevated temperatures. The reason may be twofold. First, the rate of generation of free dislocations in grain interior is underestimated at this grain size (see section 3.4.1 for the explanation of the occurrence of the relative minimum) so that the grain interior is too soft. Second, the assumption that each grain boundary dislocation is in dipolar configuration, is clearly overidealized. This means that the density of dislocation dipoles at grain boundaries is grossly overestimated. Considering the more general case where dislocations arrange irregularly at grain boundaries, there must be some dislocations which cannot find a compatible partner to form dipoles. Therefore the estimate of the average distance between grain boundary dislocation dipoles $d_{\text{dip,gb}} \approx s_{\text{gb}}$ may be too low. A good fitting is demonstrated in Fig. 3.17 (see the dashed line) by choosing a little large $d_{\text{dip,gb}} = 10 s_{\text{gb}}$. At elevated temperature, the overestimation of softening by high-angle grain boundaries may have been further intensified by overesti-

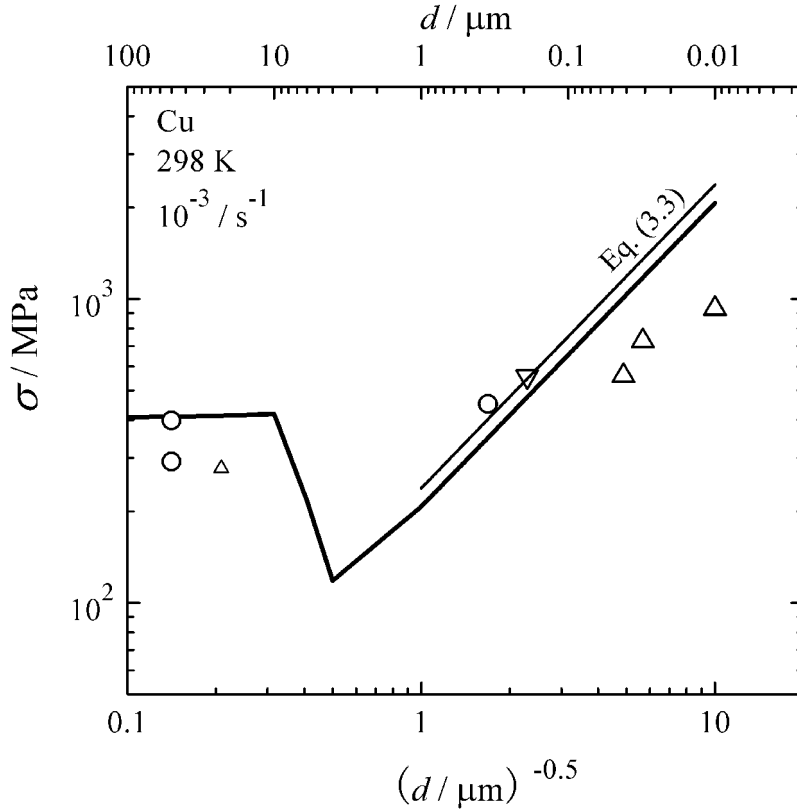


Figure 3.16: Data from Fig. 1.2 in double log scale. Line from Fig. 3.13 and Eq. (3.3).

mating the climb velocity at which the dipole partners approach each other. The driving force, which acts on dipole constituents, is presently assumed to be identical to that of an equally wide dipole in the grain interior. Due to relaxation of the stress fields of dislocations at grain boundaries the actual climb force will certainly be lower than assumed. When this point is taken into account, the factor 10 chosen in the fitting simulation will certainly be reduced towards a more reasonable value.

At 418 K, the slight difference between the line predicted by Eq. (3.7) and the curve calculated by the complete model is due to linearizing the square bracketed term in Eq. (2.27) in deriving Eq. (3.7) (see section 3.5.2).

The semi-quantitative agreement between the experimental data and the calculated results indicates that in spite of its deliberate simplicity, the model captures essential features of influence of grain boundaries on the steady state deformation resistance of pure metals at homologous temperatures less than 0.31. At ambient temperature, the model is able to explain the Hall-Petch relation found in Cu; at elevated temperature, it is able to account for the softening of ufg compared to cg Cu.

4 Discussion

Contents

4.1	Dislocation structure at grain boundaries	62
4.2	An alternative mechanism of annihilation of grain boundary dislocations	63
4.2.1	Concept of lateral climb of dislocation dipole	63
4.2.2	Rate of annihilation by lateral climb	65
4.2.3	Comparison between mutual climb and lateral climb	66
4.3	Deformation due to high-angle grain boundaries in ufg Cu	68
4.4	Density of mobile dislocations	70

4.1 Dislocation structure at grain boundaries

One may raise the question whether the dislocations can enter the boundaries when the dislocation spacing is so low here that enormous forces must act on the dislocations to press them into the boundaries against the stress fields of the existing dislocations. The problem is equivalent to inserting a new dislocation into a low-angle tilt boundary.

The situation may be checked by using a composite model [109] where the flow stress is a weighted sum of the local stresses $\sigma_s > 0$ in the soft region and $\sigma_h > 0$ in the hard region. The soft regions, which contain few dislocations, are enclosed by the hard regions with a high density of dislocations. In the current case the grain interior is the soft region and the grain boundary and its vicinity is the hard region. The flow stress reads

$$\sigma = f_s \sigma_s + f_h \sigma_h \quad \text{with} \quad f_s + f_h = 1, \quad (4.1)$$

where f_s and f_h are the volume fractions of the soft region and hard region, respectively.

We estimate that the width of the hard region roughly equals the spacing of grain boundary dislocations s_{gb} . Then volume fraction of hard region is estimated to be the ratio of s_{gb} to grain size, s_{gb}/d . The local stress in the hard region, which acts on an intruding dislocation, equals $\alpha M G b/s_{gb}$. Inserting the estimated quantities into Eq. (4.1) yields

$$\sigma_s = \frac{\sigma d - \alpha M G b}{d - s_{gb}}. \quad (4.2)$$

Now the question is whether the local stress σ_s is positive to fulfill Eq. (4.1). The result shown in Fig. 4.1 indicates that the assumption that each dislocation can be stored at the grain boundary although a dense array of dislocations is existing there, is valid.

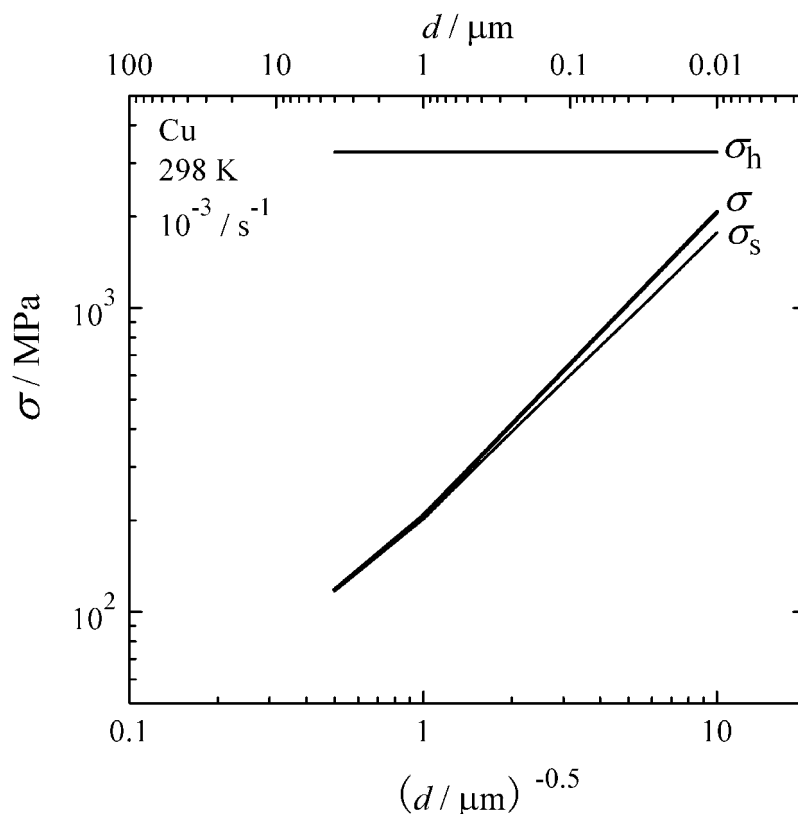


Figure 4.1: Estimated local stresses as a function of grain size. The data are taken from Fig. 3.13.

4.2 An alternative mechanism of annihilation of grain boundary dislocations

4.2.1 Concept of lateral climb of dislocation dipole

Fig. 2.3(b) actually describes a grain boundary consisting of a dislocation network formed by dislocations (the boundaries of the gray and white areas) of symmetric double glide systems from neighbouring grains. Considering the dislocations of one glide system, Fig. 2.3(b) can be simplified as Fig. 4.2 where the dislocations marked by 1 and 2 are from neighbouring grains and slightly differ on Burgers vector and line direction. At the intersection points of the dislocation lines there are immediate (spontaneous) annihilations. In the rest of the dislocation lines dipoles with a curved end are formed [110, 111]. Fig. 4.3 illustrates the configuration of a dipole taken from Fig. 4.2 by turning 90° and by neglecting the difference in the Burgers vector and the line direction.

According to Fig. 4.3, there are two possibilities for the dislocation dipoles to annihilate. Either the dipoles disappear by mutual climb of the dipole partners, which has been

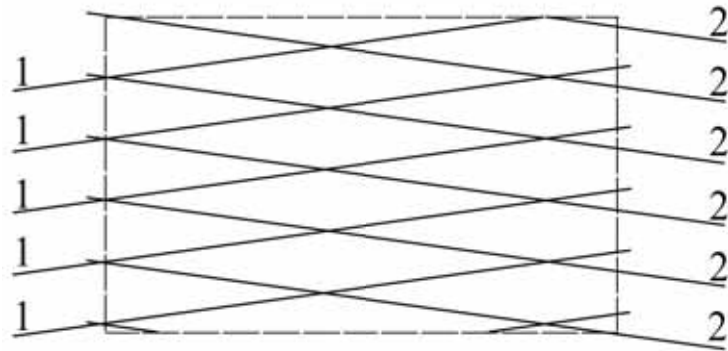


Figure 4.2: Schematic of a grain boundary consisting of a network formed by nonparallel dislocations of one glide system from neighbouring grains.

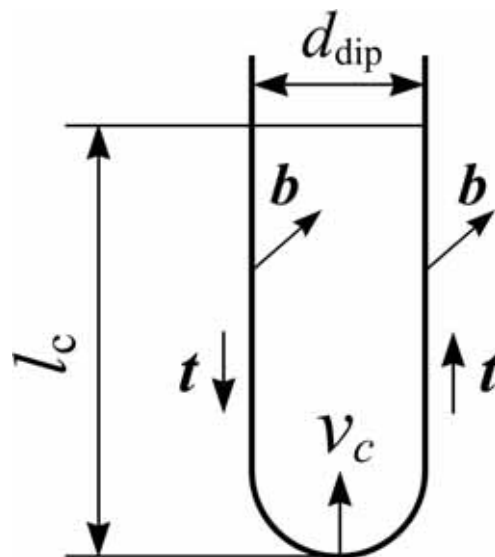


Figure 4.3: Schematic of annihilation of edge dipoles in a hair-needle configuration. b : Burgers vector, t : sense vector; d_{dip} : the average separation between dipole constituents, l_c : the length of the dipole segment needed to be overcome by the curved-end through climb at velocity v_c .

formulated in the present work (section 2.2.2.2); or the curved end climb along the lateral dislocation lines to shorten their lengths and decrease the line energy.

The velocity of lateral climb has been formulated by Nes *et al.* [111] in estimating the rate of annihilation of dislocations in the cell interior. In the following the rate of annihilation of grain boundary dislocations by lateral climb will be derived.

4.2.2 Rate of annihilation by lateral climb

The rate at which dislocations are lost through the above-mentioned process can be expressed as:

$$\dot{N}_{\text{gb}}^- = N_{\text{gb}} \nu. \quad (4.3)$$

where ν is the collapse frequency of dipoles, which is controlled by the time interval at which the distance l_c is overcome by climb

$$\nu = \frac{v_c}{l_c}. \quad (4.4)$$

The length of dipole segments l_c and the average separation between dipole partners d_{dip} scale with the average spacing of dislocations s_{gb} , respectively,

$$d_{\text{dip}} = \frac{s_{\text{gb}}}{\xi_{\text{dip}}} = \frac{1}{\xi_{\text{dip}} N_{\text{gb}}}, \quad (4.5)$$

$$l_c = \xi_c s_{\text{gb}} = \frac{\xi_c}{N_{\text{gb}}}. \quad (4.6)$$

where ξ_{dip} and ξ_c are scaling factors.

According to Nes [111], the velocity of lateral climb reads

$$v_c = b^2 B_\rho c_j \nu_{\text{Debye}} \exp\left(-\frac{Q_{\text{gb}}}{RT}\right) 2 \sinh\left(\frac{F_c b^2}{k_B T}\right) \quad (4.7)$$

where B_ρ is a constant, Q_{gb} is the activation energy of diffusion of atoms along grain boundaries, the diffusion of vacancies through the lattice is neglected here. F_c is the climb force given by line tension of the dislocation in the dipolar configuration driving the curved end to climb,

$$F_c = \frac{G b^2}{d_{\text{dip}}/2}, \quad (4.8)$$

and c_j is the density of geometrically necessary jogs in the strongly curved segments, estimated as

$$c_j = \frac{1}{d_{\text{dip}}}. \quad (4.9)$$

Combining Eqs. (4.3) to (4.9) yields

$$\dot{N}_{\text{gb}}^- = \frac{\xi_{\text{dip}}}{\xi_c} B_\rho b^2 \nu_{\text{Debye}} N_{\text{gb}}^3 \exp\left(-\frac{Q_{\text{gb}}}{RT}\right) 2 \sinh\left(\frac{2 \xi_{\text{dip}} G b^4 N_{\text{gb}}}{k_B T}\right). \quad (4.10)$$

The sinh-function term in Eq. (4.10) can be linearized at high temperature and low strain rate where its argument is much smaller than 1. Then equating the rates of generation (2.13) and annihilation (4.10) yields the steady state relation:

$$\dot{\epsilon} \propto N_{\text{gb}}^4. \quad (4.11)$$

Combining Eqs. (4.11), (2.4) and (2.30) and neglecting ρ_f , one gets

$$\dot{\epsilon} \propto \sigma^8. \quad (4.12)$$

This limiting relation agrees to that obtained with the previous model (see Eq. (3.7)). However, It is seen from Fig. 4.4 that it has not yet been reached within the range of simulation.

4.2.3 Comparison between mutual climb and lateral climb

Figure 4.4 compares the normalized relations $\dot{\epsilon}-\sigma$ calculated by using the mutual climb and lateral climb velocity. The calculations were done by choosing $B_\rho = 0.01$ [84], $Q_{\text{gb}} = 104$ kJ/mol [12], $\xi_{\text{dip}} = 1$ and $\xi_c = 5$.

At low temperature, the lateral climb gives lower deformation resistance at high strain rates. This means that the rate of annihilation of grain boundary dislocations determined by the lateral climb is more efficient than the rate of spontaneous annihilation. According to Fig. 4.3, the smaller the spacing d_{dip} of dislocation dipoles, the smaller is the radius of the curved end, and the larger the climb stress acting on the curved end produced by the line tension of the dipole partners. The enhancement in climb stress will lead to increase in climb velocity which is amplified by sinh function (see Eq. (4.7)). Moreover, the small dislocation spacing will lead to a short distance l_c over which the curved ends climb (Eq. 4.6)). When the dipole spacing becomes sufficiently small, as is usually the case at low temperature and high strain rate, a high frequency of annihilation resulted from the fast climb velocity and the short climb distance may lead to a high annihilation rate, which with the parameters chosen even exceeds the rate of spontaneous annihilation.

At elevated temperature the lateral climb process results in higher deformation resistance compared to mutual climb. This means that the lateral climb process is less efficient than the mutual climb process in annihilating of dislocations. To understand this situation one needs to compare the frequencies of annihilation given by the mutual climb and lateral climb, respectively (Eqs. (2.26) and (4.4)). Comparing Eqs. (4.8) and (A.37) it is found that the climb stress in the lateral climb case (Eq. (4.8)) is about 4 times of the climb stress in the mutual climb case (Eq. (A.37)). This may result in a higher climb velocity in the case of lateral climb. However, at elevated temperature, the dislocation spacing also becomes very large, then the distance l_c may becomes much larger than the distance over which the dipole partners climb towards each other as in the case of mutual climb. The larger ξ_c is chosen (Eq. (4.6)), the larger is the difference in the climb distance. The present choice of $\xi_c = 5$ leads the distance of climb in the case of lateral climb to be 10

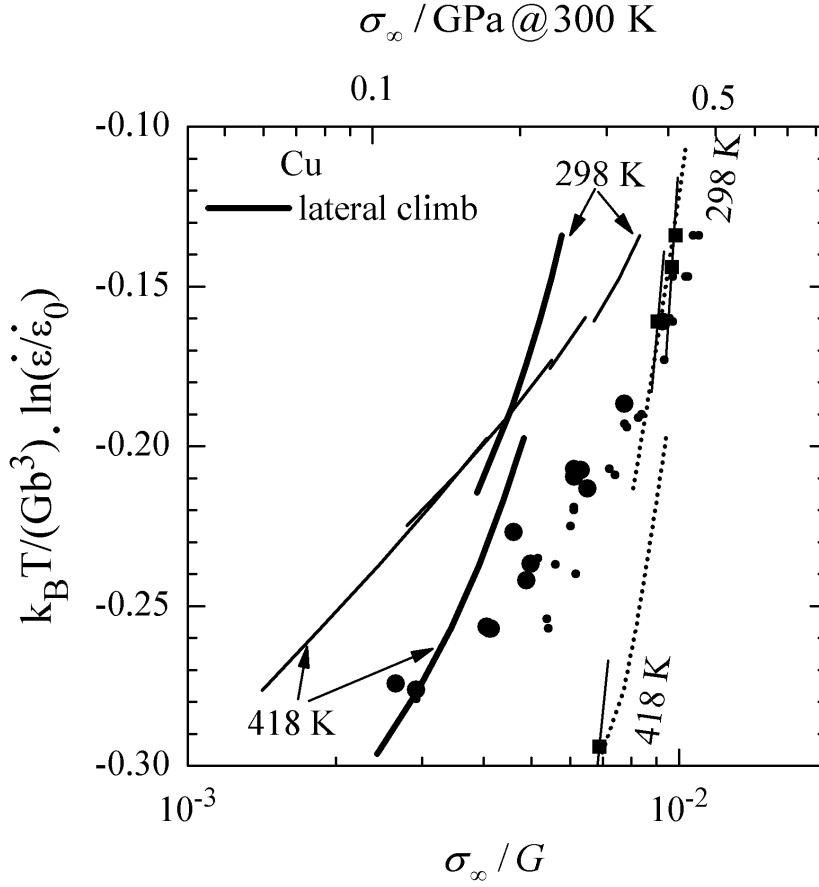


Figure 4.4: Comparison of normalized relation between $\dot{\epsilon}$ and σ for ufg Cu predicted by the mutual climb and lateral climb processes. The experimental data are from Fig. 3.17.

times that in the case of mutual climb ($l_c/(d_{\text{dip,gb}}/2)$). Thus, for the case of lateral climb, if the enhancement in velocity does not compensate the increase in climb distance, a lower frequency of annihilation compared to that in the case of mutual climb may be resulted.

The calculations suggest that the lateral climb may act as a very competitive annihilation process compared to the annihilation process described in the present model. However, to have a more exact evaluation of the rate of annihilation given by the lateral climb, one needs to consider more details on the formation of the dipolar configuration shown in Fig. 4.3 based on a microstructural basis.

4.3 Deformation due to high-angle grain boundaries in ufg Cu

Frequently, grain boundary related process like grain boundary sliding [39, 41] and diffusive flow (Nabarro-Herring and Coble creep) [16] are invoked as major mechanisms of deformation of ufg material. In the following we shall compare experimental results to theoretical predictions to discuss the possibility of Coble creep in ufg Cu.

The rate of diffusional flow by Coble creep (with diffusion along grain boundaries) is shown in Fig. 4.5 for two grain sizes d chosen as the initial grain size of ufg Cu and, to illustrate the effect of possible grain growth, as $1\mu\text{m}$. It was calculated from the standard formula [12, 112]:

$$\dot{\epsilon} = 14\pi \frac{\sigma \Omega}{k_B T} \frac{\delta D_b}{d^3}. \quad (4.13)$$

It is seen that the strain rate due to Coble creep is negligible at the lowest investigated temperature, but lies close to the experimental results at the highest one. The T -normalized plot of the data of Fig. 4.5 yields a band of data approaching the Coble creep prediction with decreasing σ (see Fig. 4.6). Lower stresses than shown could not be reached due to beginning instability of the grain structure [5]. In summary, at room temperature, Coble creep can hardly be an independent and rate controlling mechanism for ufg Cu. However, at elevated temperature, Coble creep may become the dominant deformation process.

In addition, if grain boundary sliding or diffusive flow is the dominant deformation mechanism, a strain rate sensitivity $m = 0.5$ [62, 63] or 1 [112] would be expected from theory. However, such values have never been observed for ufg Cu produced by ECAP either in our own work [5] or from literatures. Thus the deformation of ufg materials cannot be solely attributed to direct strain contributions by grain boundaries, such as grain boundary sliding and Coble creep.

4.3 Deformation due to high-angle grain boundaries in ufg Cu

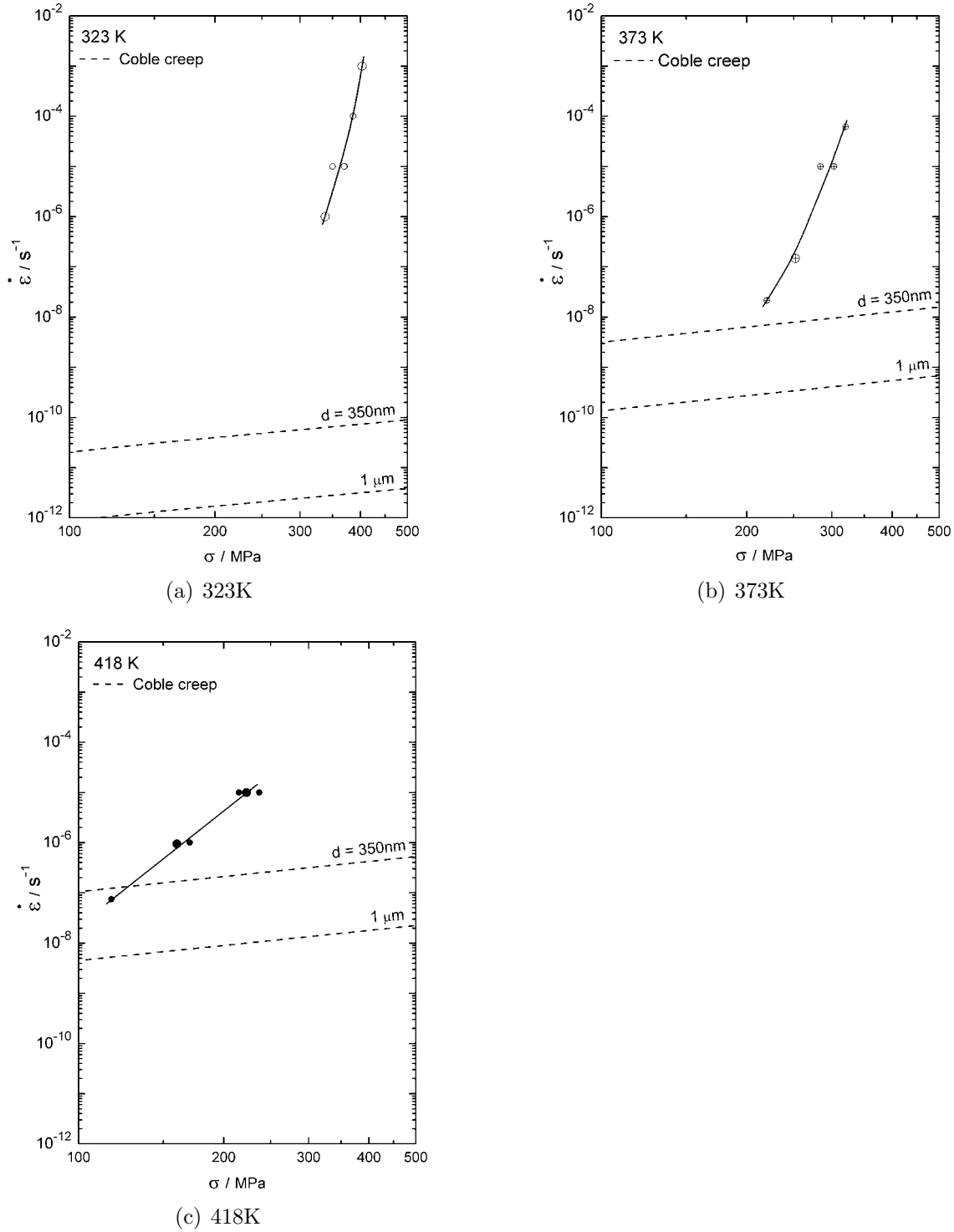


Figure 4.5: Steady-state deformation resistances of ufg Cu from [6]. Large symbols: isothermal tests at constant $\dot{\epsilon}$ or σ , small symbols: additional data from changes of deformation conditions, dashed lines: prediction for Coble creep.

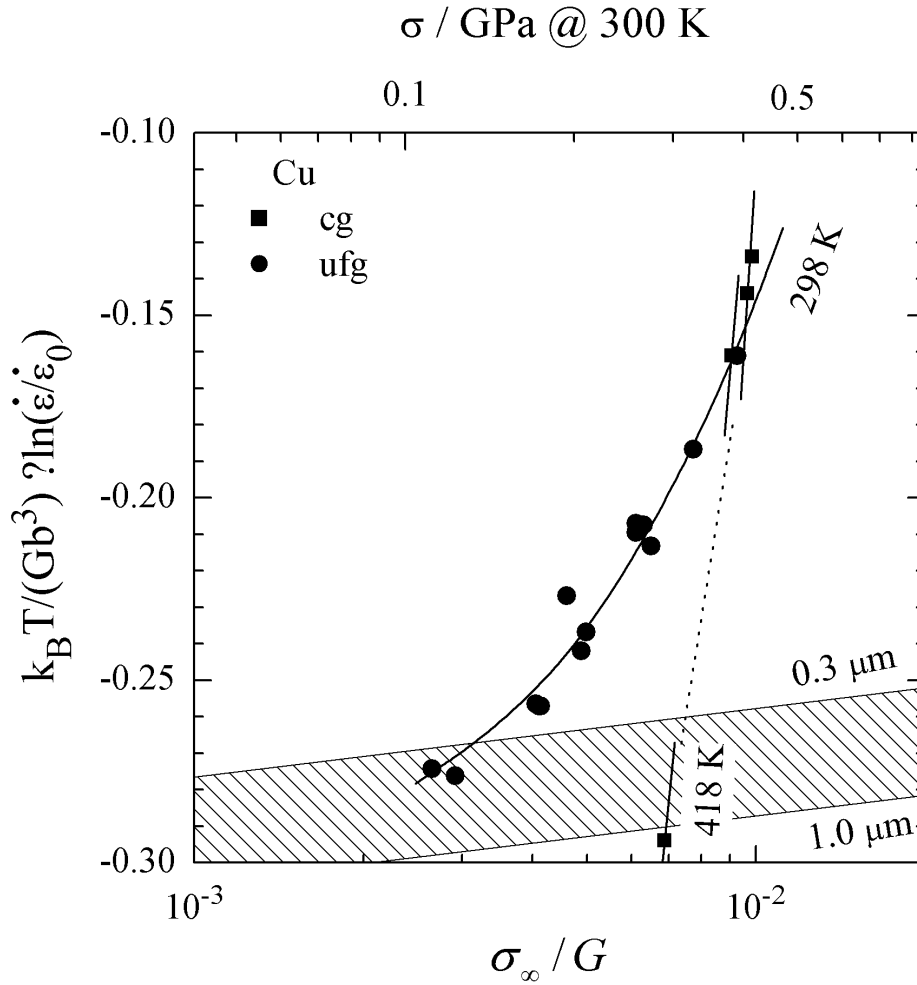


Figure 4.6: Normalized relation between stress and strain rate for steady-state deformation resistance of ufg and cg Cu. Symbols from Fig. 3.17, lines for coble creep calculated with $d/\mu = 0.3$ and 1.0 .

4.4 Density of mobile dislocations

A deficiency of the model presented in this work is that the density of free dislocation in grain interior continuously decreases with increasing strain (Figs. 3.2 and 3.4) in modeled ufg materials. This deficiency may suggest that the mobile dislocation density may be underestimated as stated in section 3.2.

According to the Orowan equation (Eq. (2.28)), for a prescribed strain rate, a continuous decrease in the mobile dislocation density must result in a continuous increase in the

average velocity of moving dislocations. However, the velocity cannot increase to infinity but must stop at an upper limit. The upper limit for dislocation velocity appears to be the velocity of sound in the crystal [113]. That means that the density of mobile dislocations must not further decrease to attain the prescribed strain rate when the upper limit of dislocation velocity is reached. Thus a new situation may arise in grain interiors of ufg and nano materials where the density of mobile dislocations becomes larger than the density of stored dislocations. From this point of view, the density of mobile dislocation is underestimated for modeled ufg and nano materials. One may expect that a steady state of free dislocation density can be reached, if the mobile dislocation density is enhanced by counting the dislocations which produce strain before they arrive at grain boundaries.

To check the consequence of enhancement in mobile dislocation density, one may modify the rate of generation of free dislocations by replacing the density ρ_f in Eq. (2.12) by the total density $\rho_f + \rho_{gb}$. Thus the generation rate of mobile dislocations is accounted for by the dislocations stored at grain boundaries. A steady state in the evolution of the density of free dislocations can be indeed observed in simulations based on this consideration. However, to arrive at reasonable formulations on the rates of evolution of mobile dislocations, more considerations are needed in the future work.

5 Summary

Contents

5.1	English	74
5.2	German	75

5.1 English

Published data on pure Cu at or close to its steady state of deformation suggest a Hall-Petch relation for the flow stress at ambient temperature in the range of grain sizes $1\ \mu\text{m} > d > 10\ \text{nm}$ [4] while for elevated temperatures ultrafine-grained (ufg) Cu produced by severe plastic deformation exhibits softening relative to conventional grain (cg) sizes $d > 10\ \mu\text{m}$ [5]. Such deformation behavior can be explained based on understanding the microstructure of the materials. In cg materials the dislocations generally form a cellular structure with low-angle (subgrain) boundaries within the grains. The low-angle (subgrain) boundaries generally have a strengthening effect [69–71]. In ufg and nanocrystalline materials, the mean free path of free dislocations approaches or becomes larger than the grain size so that free dislocations are able to reach high-angle grain boundaries, before they get stored in the grain interiors. Thus the cellular structure does not form and the deformation resistance is determined by the extrinsic dislocations with edge character of high density located at high-angle grain boundaries. The extrinsic dislocations form single-sided steps in the grain boundaries. The single-sided steps may react with each other to form grain boundary ledges (double sided steps) with zero stress field. The formation of double-sided steps with two single-sided steps is regarded as annihilation of extrinsic grain boundary dislocations. If the annihilation process is not sufficiently high to lower the density of grain boundary dislocations, the material is hardened. Otherwise, the material is softened.

A model based on statistical dislocation theory was developed to explain the deformation behavior of ufg and nano Cu. Two dislocation species were introduced to describe the dislocation structure consisting of dislocations in grain interiors and dislocations stored at grain boundaries. Rate equations for dislocation structure evolution by generation and annihilation of the two dislocation species were derived.

The steady state deformation behavior of Cu within a grain size range of $0.01 \leq d / \mu\text{m} \leq 100$ was simulated in the interval $298 \leq T/\text{K} \leq 418$, corresponding to $0.22 \leq T_{\text{hom}} \leq 0.31$. Strain-controlled simulations were performed for strain rates ranging from 10^{-3} to $10^{-8}\ \text{s}^{-1}$. The simulation results were compared with the experimental findings. The possibility of the occurrence of Coble creep in ufg Cu ($d = 0.35\ \mu\text{m}$) was evaluated.

The main results are:

- Within the simulated range of deformation conditions, for cg Cu, the ratio of effective stress to applied stress varies in the range $0.4 < \sigma^*/\sigma < 0.6$ (see 3.3.2), while for ufg Cu, the ratio is vanishingly small.
- For cg Cu, the density of free dislocations is distinctly higher than the density of dislocations at grain boundaries. Thus the deformation resistance is mainly determined by the free dislocations in grain interiors. For ufg Cu, the opposite is the case (see 3.3.3).

- The dependence of strain rate on temperature and stress is stronger for ufg than for cg Cu. The enhanced strain rate sensitivity of flow stress leads to a transition from strengthening to softening in steady state deformation for some modeled ufg Cu compared to cg Cu. The strain rate sensitivity of 0.125 predicted by the model for ufg Cu at elevated temperature agrees remarkably well with the experimental observations [5] (see 3.3.1, 3.6).
- The total rate of generation of dislocations increases with decreasing grain size. In cg material, the enhancement in the total generation rate due to grain boundaries is not significant as the mean free path of free dislocations is distinctly smaller than the grain size. In ufg materials, the generated dislocations are mainly stored at grain boundaries. We consider two mechanisms of annihilation of grain boundary dislocations. At low homologous temperatures where spontaneous dislocation annihilation prevails, Hall-Petch strengthening leads to increase of deformation resistance with decreasing grain size (see 3.4, 3.5.1). At elevated temperatures fast thermally activated (climb-controlled) annihilation of dislocations at grain boundaries leads to softening compared to cg material when the grains are ultrafine.
- The Hall-Petch relation can be derived from the model. The flow stresses are overestimated by the model compared to the experimental results. Probable reasons are i) possible uncertainty of the experimental results; ii) neglect of relax the relaxation of the stress field of grain boundary dislocations; and iii) neglect of diffusional deformation in nano materials (see Fig. 3.16 in 3.6).
- The simulation results for ufg Cu ($d=0.35 \mu\text{m}$) are in semi-quantitative agreement with experimental findings. At ambient temperature, the model falls short of predicting the hardening effect of grain boundary for $d = 0.35 \mu\text{m}$. At elevated temperature, the softening effect is overestimated. This may be due to i) underestimating the rate of generation of free dislocations in grain interiors; and ii) overestimating the rate of annihilation of grain boundary dislocations (see Fig. 3.17 in 3.6).
- At room temperature, Coble creep can hardly be independent and rate controlling mechanisms for ufg Cu. However, at the highest investigated temperature, Coble creep may be the dominant deformation process (see 4.3).

In spite of its deliberate simplicity, the model captures essential features of influence of grain boundaries on the steady state deformation resistance of pure metals at homologous temperatures less than 0.31.

5.2 German

Publizierte Daten zum Verformungsverhalten von Rein-Cu im bzw. nahe am Zustand stationärer Verformung legen eine Hall-Petch Beziehung bei Raumtemperatur für einen Korngrößenbereich $1 \mu\text{m} > d > 10 \text{ nm}$ nahe [4]. Hingegen zeigt durch Hochverformung erzeugtes ultrafeinkörniges (ufg) Cu bei erhöhter Temperatur eine Erweichung im Vergleich

zur konventionellen Korngröße (cg) mit $d > 10 \mu\text{m}$ [5]. Dieses Verhalten kann auf der Basis eines Verständnisses der Mikrostruktur erklärt werden. In cg Materialien ordnen sich die Versetzungen zu zellularen Strukturen mit einem Netzwerk von Kleinwinkel-Korngrenzen (KWKG) innerhalb der Kristallite. Die KWKG führen üblicherweise zu einer Verfestigung [69–71]. In ufg und nanokristallinen (nano) Materialien erreicht der mittlere Laufweg freier Versetzungen die Korndimension so dass Versetzungen die Großwinkel-Korngrenzen erreichen bevor sie innerhalb des Kornes liegenbleiben. In diesem Fall bildet sich keine Zellstruktur im Korninneren und der Verformungswiderstand wird durch die (hohe) Dichte von Korngrenzversetzungen bestimmt. Korngrenzversetzungen stellen einseitige Stufen innerhalb der Korngrenze dar (sofern eine entsprechende Stufenkomponente vorliegt). Zwei einseitige Stufen durch Versetzungen aus benachbarten Körnern können zu einer zweiseitigen Stufen mit verschwindendem Spannungsfeld reagieren. Diese Reaktion wird als Annihilation von Korngrenzversetzungen betrachtet. Falls die Annihilationsgeschwindigkeit nicht ausreicht, um die Dichte der Korngrenzversetzungen zu reduzieren folgt eine Materialverfestigung bzw. eine Entfestigung im Falle rascher Annihilation.

In dieser Arbeit wurde ein Modell auf der Basis einer statistischen Versetzungstheorie entwickelt, mit dem das Verformungsverhalten von ufg und nano Kupfer erklärt werden soll. Die Versetzungsstruktur wird dabei durch die beiden Familien von Versetzungen im Korninneren und an den Korngrenzen beschrieben. Für beide Versetzungstypen sind Evolutionsgleichungen, d.h. Terme zur Erzeugung und Vernichtung, formuliert worden.

Das stationäre Verformungsverhalten von Cu mit Korngrößen $0.01 \leq d / \mu\text{m} \leq 100$ wurde im Temperaturbereich $298 \leq T/\text{K} \leq 418$ (entspricht $0.22 \leq T_{\text{hom}} \leq 0.31$) simuliert. Dehnratenkontrollierte Simulationen deckten den Bereich von 10^{-3} bis 10^{-8}s^{-1} ab und sind mit experimentellen Ergebnissen verglichen worden. Die Möglichkeit des Auftretens von Coble-Kriechen in ufg Cu ($d = 0.35 \mu\text{m}$) wurde erörtert.

Im Folgenden sollen die wichtigsten Ergebnisse der Simulationen zusammengefasst werden.

- Innerhalb des abgedeckten Dehnratenbereichs ergibt sich für cg Cu ein Verhältnis von effektiver zu angelegter Spannung von $0.4 < \sigma^*/\sigma < 0.6$ (siehe 3.3.2). Im Falle von ufg Cu ist dieses Verhältnis verschwindend klein.
- In cg Cu überwiegt die Dichte freier Versetzungen im Korninneren die der Korngrenzversetzungen deutlich. Der Verformungswiderstand ist somit durch die Dichte freier Versetzungen bestimmt. In ufg Cu ist die Situation umgekehrt (siehe 3.3.3).
- Die Abhängigkeit der Fließspannung von Dehnraten und Temperatur ist für ufg Cu größer als für cg Cu. Diese erhöhte Dehnratenabhängigkeit führt unter bestimmten Bedingungen zu einem Übergang von relativ erhöhter zu relativ erniedrigter Festigkeit von ufg im Vergleich zu cg Cu. Die Modellvorhersage eines Spannungsex-

ponenten von $n = 8$ (entspricht $m = 0.125$) bei erhöhter Temperatur stimmt bemerkenswert mit den experimentellen Beobachtungen überein [5] (siehe 3.3.1,3.6).

- Die Gesamterzeugungsrate von Versetzungen steigt mit sinkender Korngröße. Für cg Material spielt diese Erhöhung keine Rolle, da der mittlere freie Laufweg immer deutlich geringer als die Korngröße bleibt. Die in ufg Material erzeugten Versetzungen werden überwiegend an den Korngrenzen deponiert. Im vorliegenden Modell werden zwei Annihilationsmechanismen für Korngrenzversetzungen angenommen. Bei niedriger homologer Temperatur, bei der spontane (athermische) Annihilationsreaktionen dominieren, findet sich Hall-Petch Verfestigung mit abnehmender Korngröße (siehe 3.4, 3.5.1). Bei erhöhter Temperatur erfolgt Annihilation thermisch aktiviert (und kletterkontrolliert), und sorgt für eine relative Erweichung von ufg im Vergleich zu cg Material.
- Die Hall-Petch Beziehung kann aus dem Modell abgeleitet werden. Das Modell überschätzt allerdings die Fließspannung verglichen mit experimentellen Resultaten. Mögliche Gründe könnten sein: i) Unsicherheit der Messwerte; ii) Vernachlässigung der Reduzierung des Spannungsfelds von Korngrenzversetzungen; iii) Vernachlässigung von Diffusionsbeiträgen zur Verformung in nano Materialien (siehe Abbildung 3.16 in 3.6).
- Die Simulationsergebnisse von ufg Cu ($d=0.35 \mu\text{m}$) stimmen halb-quantitativ mit den experimentellen Ergebnissen überein. Bei Raumtemperatur sagt das Modell keine Festigkeitssteigerung durch Korngrenzen mit mittlerem Abstand $d=0.35 \mu\text{m}$ (ufg) voraus. Für erhöhte Temperatur wird die Erweichung überschätzt. Dies kann durch folgende Punkte begründet werden: i) Unterschätzung der Erzeugungsrate von Versetzungen im Korninnern; und ii) Überschätzung der Annihilationsrate von Korngrenzversetzungen (siehe Abbildung 3.17 in 3.6)
- Coble-Kriechen kann bei Raumtemperatur kaum als unabhängiger und ratenkontrollierender Verformungsmechanismus angesehen werden. Hingegen erscheint dies plausibel bei erhöhter Temperatur (siehe 4.3).

Obwohl das Modell bewusst einfach gehalten ist, beschreibt es die wichtigen Einflüsse der Korngrenzen auf den stationären Verformungswiderstand reiner Metalle bei homologen Temperaturen von unter 0.31.

Figures

1.1	Temperature normalized strain rate as function of shear modulus normalized flow stress for Cu with different grain sizes d and a $\langle 123 \rangle$ -oriented Cu single crystal from nanoindentation at ambient temperature ($T_{\text{hom}} = 0.22$) [4, 14] and uniaxial compression from room temperature up to 448 K ($T_{\text{hom}} = 0.35$) [5, 8, 15]. Large symbols: saturation stress (or steady-state deformation resistances); small symbols: maximum deformation resistance (the flow stress or creep rate measured at the end of a test). Right ordinate axis: strain rate at 300 K.	4
1.2	Variation of flow stress with inverse square root of grain size d with different T and $\dot{\epsilon}$. The arrow pointing to the saturated flow stress (400 ± 50) MPa of cg Cu with $d = 50 \mu\text{m}$ [4]. Data from Fig. 1.1.	5
2.1	Schematic of a) subgrains of size w with free dislocations in grain interior in coarse grain of size d , b) ultrafine-grained structure with $d = w_{\infty}$. Thick lines: high-angle grain boundaries; Thin lines: low-angle subgrain boundaries.	12
2.2	Mean free path of free dislocations $\Lambda_p = 50 b G / \sigma$, subgrain size w_{∞} and critical size of dislocation sources as function of shear modulus normalized stress. Horizontal lines display the grain sizes d_{cg} for cg Cu and d_{ufg} for ufg Cu. Vertical dotted lines mark the boundary of experimental range where cg and ufg Cu were investigated by Li [5, 8].	14
2.3	Schematic of edge dislocation structure in grain boundaries. a) grain 1 with a nonplanar surface due to intrusions (valleys) and extrusions (hills) produced by single-sided steps formed by edge dislocations resulting from symmetric double glide; b) superposition of two such grains (grain 1 and 2) with parallel gray-white sequence of hills and valleys which are in general not parallel for the two neighboring grains due to different grain orientations. The marked areas represent superpositions of valley-valley, hill-hill and valley-hill configurations from left to right; c) regular arrangement of dislocations in dipolar configurations resulting from single-sided steps of neighbouring grains on the two sides of the grain boundary; d) simplified picture of c) neglecting the differences in Burgers vectors and line directions of dislocations in dipolar configurations. s_{gb} : spacing of grain boundary dislocations; $d_{\text{dip,gb}}$: dipole height (spacing of glide planes); ϕ : angle between the slip plane and the grain boundary surface.	17

2.4	Schematic of the structure of extrinsic grain boundary dislocations. (a) a grain boundary between grain 1 and 2; (b) schematic dislocation picture of (a); (c) stress-free grain boundary ledge after recombination of steps by dislocation climb in grain boundary.	18
2.5	Schematic of the microstructure with dislocations described by: ρ_f : density of free dislocations in grain interior; N_{gb} : areal density of dislocations at grain boundaries; d : grain size; δ_{gb} : the width of grain boundary. Dashed ellipses mark dislocations in a dipolar configuration.	19
2.6	Schematic of the comparison between the slipped area (gray region) and the cross section of a grain. a) the dislocation loop is completely stored in the grain interior; b) most part of the dislocation loop is stored at the grain boundary.	22
2.7	Schematic of dislocation loops in a) a large and b) a small grains, and c) the probability of loops getting stored within grains as a function of dislocation spacing δ and grain size at the same deformation condition.	23
2.8	Relation between length of dislocations generated per slipped area and spacing of free dislocations δ . $2/\Lambda_{\rho,d}$ (Eq. (2.12)) and $2/\Lambda_\rho$ (Eq. (2.10)): length of free dislocations generated in grain interiors per slipped area; $2/\Lambda_{tot}$: total length of dislocations generated in grain interiors and at grain boundaries per slipped area (Eq. (2.15)); The line marked by $\dot{\rho}_f^+ = \dot{\rho}_f^{-,spon}$ is derived by equating the rate of generation (2.9) and the rate of spontaneous annihilation (2.16) of free dislocations. The symbols $<$ and $>$ mark the area as where the generation rate $\dot{\rho}_f^+$ is smaller or larger than the annihilation rate $\dot{\rho}_f^{-,spon}$, respectively.	25
2.9	Formation of dipoles by mutual attraction of free dislocations with Burgers vectors of opposite sign within slip planes of d_{dip} apart. Within the spacing d_{spon} , the dipole disappears spontaneously; Beyond the spacing d_{spon} but within d_{dip} , the dipole constituents overcome the distance of d_{dip} through mutual climb. Vacancy debris (open squares) are left after annihilation. . .	27
2.10	Schematic of the thermally activated process of a dislocation overcoming local obstacles. λ : the mean spacing of thermal obstacles along the dislocation line; Δx : the width of obstacle; shadowed area: the activation area.	32
2.11	Logical structure of the model.	33
3.1	Example of curves for the evolution of stress and dislocation densities with strain for cg ($d = 50 \mu m$) at 298 K. (a) flow stress σ , athermal stress σ_G , and effective stress: σ^* ; (b) dislocation spacing $\rho_f^{-0.5}$, $\rho_{gb}^{-0.5}$ and s_{gb} . The quantities d and d_{spon} are the grain size and the critical spacing for spontaneous annihilation, respectively. (c) rates of evolution of dislocation density. Deriving from Eq. (2.15) the <i>total</i> rate of generation of dislocations $d\rho_{tot}^+/d\epsilon$ equals $d\rho_f^+/d\epsilon + dN_{gb}^+/d\epsilon \cdot 2/d$	40
3.2	As Fig. 3.1 for ufg Cu.	41
3.3	As Fig. 3.1 for 418 K.	42

3.4	As Fig. 3.2 for 418 K.	43
3.5	Calculated steady state deformation resistance of cg (grain size $d = 50 \mu\text{m}$) and ufg ($d = 0.2 \mu\text{m}$) at 298 and 418 K. Simulations were done at strain rates ranging from 10^{-3} to 10^{-8} s^{-1} separated by one order of magnitude. Open and full Circles mark strain rates at the shear modulus normalized stress σ/G for cg and ufg Cu, respectively.	44
3.6	Stress exponent $n \approx \Delta \ln \dot{\epsilon} / \Delta \ln \sigma$ (derived from neighbouring points of Fig. 3.5) of the steady state deformation rate and strain rate sensitivities $m = 1/n$ of the steady state flow stress as function of shear modulus normalized stress.	45
3.7	σ^*/σ versus $\dot{\epsilon}$ in steady state deformation of cg and ufg Cu at 298 and 418 K.	46
3.8	Strain rate dependence of dislocation spacings for cg Cu at 298 and 418 K. The horizontal lines mark $d_{\text{spn,gb}}$ and the grain size.	47
3.9	As Fig. 3.8 for ufg Cu. The densities ρ_f are obtained from the calculations at $\epsilon = 0.5$ where the flow stresses have already saturated.	48
3.10	Rates of generation and annihilation of grain boundary dislocations as function of strain rate at 298 K.	49
3.11	As Fig. 3.10 for 418 K.	50
3.12	Steady state deformation resistance $\dot{\epsilon}-\sigma$ of pure Cu at room temperature calculated from the model as function of grain size.	52
3.13	Steady state stresses and dislocation densities as function of grain size at ambient temperature and $\dot{\epsilon} = 10^{-3} \text{ s}^{-1}$ for Cu. (a) stress σ and athermal stress components; σ_G : total athermal stress (Eq. (2.30)); $\sigma_{G,\text{gb}} = \alpha M G b \sqrt{f_{\text{gb}} \rho_{\text{gb}}}$ and $\sigma_{G,f} = \alpha M G b \sqrt{\rho_f}$ characterize the athermal stress contributions due to ρ_{gb} and ρ_f alone. (b) dislocation densities; $\rho_{\text{tot}} = \rho_f + \rho_{\text{gb}}$ is the total dislocation density. The density ρ_f is obtained from the calculations at $\epsilon = 0.5$	53
3.14	(a) Stored dislocation length per slipped area in the grain interior and (b) mean free path of free dislocations as function of $d^{-0.5}$. Data are derived from Fig. 3.13(b).	54
3.15	Steady state deformation resistance $\dot{\epsilon}-\sigma$ of pure Cu at elevated temperature of 418 K calculated from the model as function of grain size.	55
3.16	Data from Fig. 1.2 in double log scale. Line from Fig. 3.13 and Eq. (3.3).	58
3.17	Temperature-normalized relation between steady state stress σ_∞ and strain rate $\dot{\epsilon}$ in compression for cg ($d = 50 \mu\text{m}$) and ufg ($d = 0.35 \mu\text{m}$) Cu. The dashed line from the simulation with $d_{\text{dip,gb}} = 10 s_{\text{gb}}$. The experimental data from Fig. 1.1.	59
4.1	Estimated local stresses as a function of grain size. The data are taken from Fig. 3.13.	63
4.2	Schematic of a grain boundary consisting of a network formed by nonparallel dislocations of one one glide system from neighbouring grains.	64

4.3	Schematic of annihilation of edge dipoles in a hair-needle configuration. b : Burgers vector, t : sense vector; d_{dip} : the average separation between dipole constituents, l_c : the length of the dipole segment needed to be overcome by the curved-end through climb at velocity v_c	64
4.4	Comparison of normalized relation between $\dot{\epsilon}$ and σ for ufg Cu predicted by the mutual climb and lateral climb processes. The experimental data are from Fig. 3.17.	67
4.5	Steady-state deformation resistances of ufg Cu from [6]. Large symbols: isothermal tests at constant $\dot{\epsilon}$ or σ , small symbols: additional data from changes of deformation conditions, dashed lines: prediction for Coble creep.	69
4.6	Normalized relation between stress and strain rate for steady-state deformation resistance of ufg and cg Cu. Symbols from Fig. 3.17, lines for coble creep calculated with $d/\mu = 0.3$ and 1.	70
A.1	Geometrical relationship between average radius of grain sections r' and the measured grain size d	95
A.2	Storage of dislocations at grain boundaries in one grain in 1-Dimension schematic. X : the spacing between the slip planes; gb: grain boundary being perpendicular to the paper.	99
A.3	Configuration of (a) dislocation dipoles (marked by A and B) and (b) the normal stress σ_{yy} in the center of the dipole at the grain boundary.	101

Tables

- 3.1 Material parameters for Cu. 36
- 3.2 Model variables. 36
- 3.3 Initial state of microstructure. 37

Bibliography

- [1] M.A. Meyers, A. Mishra, and D.J. Benson. Mechanical properties of nanocrystalline materials. *Prog. Mater. Sci.*, 51:427–556, 2006. ix, 2, 4
- [2] N. Hansen. Hall-Petch relation and boundary strengthening. *Scripta Mater.*, 51:801–806, 2004. ix, 2, 5
- [3] M.A. Meyers, A. Mishra, and D.J. Benson. Mechanical properties of nanocrystalline materials. *Progr. Mater. Sci.*, 2005. ix, 2
- [4] W. Blum, Y.J. Li, J. Chen, X.H. Zeng, and K. Lu. On the Hall-Petch relation between flow stress and grain size. *Z. Metallkd.*, 2006. submitted. ix, 2, 3, 4, 5, 74, 75, 79
- [5] Y.J. Li, X.H. Zeng, and W. Blum. *Acta Mater.*, 52(17):5009–5018, 2004. ix, 2, 3, 4, 8, 14, 68, 74, 75, 76, 77, 79, 100
- [6] W. Blum and Y. Li. Influence of grain boundaries on steady-state deformation resistance of ultrafine-grained Cu. *phys. stat. sol. (a)*, 201(13):2915–2921, 2004. 69, 82
- [7] Y. J. Li, R. Valiev, and W. Blum. Deformation kinetics of ultrafine-grained Cu and Ti. *Mater. Sci. Eng. A*, 410-411:451–456, 2005.
- [8] Y. J. Li. *Deformation behavior of ultrafine-grained copper*. PhD thesis, University of Erlangen-Nürnberg, 2006. ix, 2, 3, 4, 8, 14, 79
- [9] I.A. Ovidka. Superplasticity and ductility of superstrong nanomaterials. *Rev. Adv. Mater. Sci.*, 10:89–104, 2005. ix, 8, 31
- [10] Y. M. Wang and E. Ma. Three strategies to achieve uniform tensile deformation in a nanostructured metal. *Acta Mater.*, 52:1699–1709, 2004. ix, 8, 31
- [11] U.F. Kocks and H. Mecking. Physics and phenomenology of strain hardening: the FCC case. *Progr. Mater. Sci.*, 48(3):171–273, 2003. 2, 21, 28
- [12] H. J. Frost and M. F. Ashby. *Deformation-Mechanism Maps*. Pergamon Press, Oxford, 1982. 2, 36, 66, 68
- [13] H.W. Höppel, Z.M. Zhou, H. Mughrabi, and R.Z. Valiev. Microstructural study of the parameters governing coarsening and cyclic softening in fatigued ultrafine-grained copper. *Philos. Mag. A*, 82(9):1781–94, 2002. 3

- [14] J. Chen, L. Lu, and K. Lu. Hardness and strain rate sensitivity of nanocrystalline Cu. *Scripta Mater.*, 54:1913–1918, 2006. 3, 4, 79
- [15] W. Blum, P. Eisenlohr, and V. Sklenička. Creep of bulk nanostructured materials. In M. Zehetbauer and Y. T. Zhu, editors, *Bulk Nanostructured Materials*. Wiley-VCH, 2006. 3, 4, 79
- [16] A.H. Chokshi, A. Rosen, J. Karch, and H. Gleiter. On the validity of the Hall-Petch relationship in nanocrystalline materials. *Scripta Mater.*, 23:1679–1684, 1989. 4, 7, 68
- [17] T. G. Nieh and J. Wadsworth. Hall-Petch relation in nanocrystalline solids. *Scripta Mater.*, 25:955, 1991.
- [18] Fougere G. E., Weertman J. R., Siegel R. W., and Kim S. Grain-size dependent hardening and softening of nanocrystalline Cu and Pd. *Scripta Mater.*, 26:1879–1883, 1992.
- [19] Arzt E. Size effects in materials due to microstructural and dimensional constraints: a comparative review. *Acta Metall.*, 46:5611–5626, 1998.
- [20] Conrad H. and Narayan J. Grain-size dependent hardening and softening of nanocrystalline Cu and Pd. *Scripta Mater.*, 42:1025, 2000. 4
- [21] Hall E. O. The Deformation and Ageing of Mild Steel: III Discussion of Results. *Phys. Soc. B*, 64:747–753, 1951. 5
- [22] Petch N. J. The cleavage strength of polycrystals. *J. Iron Steel Inst.*, 174:25, 1953. 5
- [23] Armstrong R. W. *Yield, flow and fracture of polycrystals*, pages 1–31. Applied Science Publ., London, 1983.
- [24] M.J. Marcinkowski and R.M. Fisher. *Trans. TMS-AIME*, 233:293, 1965. 6, 31
- [25] J. C. M. Li. Petch relation and grain boundary sources. *Trans. Metall. Soc. AIME*, 277:239–247, 1963. 7
- [26] J. C. M. Li and Y. T. Chou. The role of dislocations in the flow stress grain size relationships. *Metall. Trans.*, 1:1145–1159, 1968. 5, 6, 7, 31
- [27] J.P. Hirth and J. Lothe. *Theory of dislocations*. John Wiley & Sons, New York, 2nd edition, 1982. 6, 28, 101, 103, 104
- [28] P.J. Worthington and E. Smith. The formation of slip bands in polycrystalline 3% silicon iron in the pre-yield microstrain region. *Acta Met.*, 12:1277–1281, 1964. 6
- [29] H. Conrad, S. Feuerstein, and L. Rice. Effects of grain size on the dislocation density and flow stress of niobium. *Mater. Sci. Eng.*, 2:157–168, 1967. 6

-
- [30] Crussard J. NPL Symp. Relation substructure and strength metals and alloys. *Scripta Mater.*, HMSO, London:548, 1963. 7
- [31] Crussard J. . *J. Austr. Inst. Metals*, 8:317, 1963. 7
- [32] E. Hornbogen. . *Trans. ASM*, 56:16, 1963. 7
- [33] Z. Budrovic, Van Petegem, S., B. Derlet, P.M. Schmitt, H Van Swygenhoven, Schafler E., and Zehetbauer. M. Footprints of deformation mechanisms during in situ x-ray diffraction: Nanocrystalline and ultrafine grained Ni. *Appl. Phys. Lett.*, 86:231910–231912, 2005. 7
- [34] Masumura R. A., Hazzledine P. M., and Pande C. S. Yield stress of fine grained materials. *Acta Metall.*, 46:4527–4534, 1998. 7
- [35] B. Cai, Q.P. Kong, P. Cui, L. Lu, and K. Lu. Creep behavior of cold-rolled nanocrystalline pure copper. *Scripta Mater.*, 45:1407–1413, 2001.
- [36] J.R. Weertman. Hall-Petch strengthening in nanocrystalline metals. *Mater. Sci. Eng. A*, 166:161–167, 1993. 7
- [37] R. Z. Valiev. Structure and mechanical properties of ultrafine-grained metals. *Mater. Sci. Eng. A*, 234-236:59–66, 1997. 7
- [38] L. Lu, M.L. Sui, and K. Lu. Superplastic Extensibility of Nanocrystalline Copper at Room Temperature. *Science*, 287:1463, 2000.
- [39] R. Z. Valiev, E. V. Kozlov, Yu. F. Ivanov, J. Lian, A. A. Nazarov, and B. Baudelet. Deformation behaviour of ultra-fine-grained copper. *Acta metall. mater.*, 42(7):2467–2475, 1994. 7, 68
- [40] R.Z. Valiev. Recent developments of SPD processing for fabrication of bulk nanostructured materials. In Y.T. Zhu, T.G. Langdon, R.S. Mishra, M.J. Saran, and T.C. Lowe, editors, *Ultrafine-Grained Materials II*, pages 313–322., Seattle, Washington, February 17-21 2002. TMS Publ., Warrendale, PA.
- [41] R.Z. Valiev, I.V. Alexandrov, Y.T. Zhu, and T.C. Lowe. Paradox of Strength and Ductility in Metals Processed by Severe Plastic Deformation. *J. Mater. Res.*, 17(1):5–8, Jan. 2002. 7, 68
- [42] R.Z. Valiev. Paradoxes of severe plastic deformation. *Adv. Eng. Mater.*, 5:296–300, 2003.
- [43] N.Q. Chinh, G. Vörös, P. Szommer, Z. Horita, and T.G. Langdon. Grain boundary sliding as a significant mechanisms of low temperature deformation in ECAP aluminum. *Mater. Sci. Forum*, 503-504:1001–1006, 2006. 7
- [44] T.G. Langdon. Grain boundary sliding revisited: Developments in sliding over four decades. *J. Mater. Sci.*, 41:597–609, 2006. 7

- [45] H. Van Swygenhoven and A. Caro. Plastic behavior of nanophase Ni: A molecular dynamics computer simulation. *Appl. Phys. Lett.*, 71:1652, 1997. 7
- [46] J. Schiøtz, F. D. Ditolla, and K. W. Jacobsen. Softening of nanocrystalline metals at very small grain sizes. *Nature*, 391:561–563, 1998.
- [47] H.v. Swygenhoven, M. Spaczer, and A. Caro. Microscopic description of plasticity in computer generated metallic nanophase samples: a comparison between Cu and Ni. *Acta Mater.*, 47(10):3117–3126, 1999.
- [48] H. Van Swygenhoven and P.M. Derlet. Grain-boundary sliding in nanocrystalline fcc metals. *Phys. Rev. B*, 64(224105):1–9, 2001.
- [49] K.S. Kumar, H. Van Swygenhoven, and S. Suresh. Mechanical behavior of nanocrystalline metals and alloys. *Acta Metall.*, 51:5743–5774, 2003. 7
- [50] S.X. McFadden, R.S. Mishra, R.Z. Valiev, A.P. Zhilyaev, and A.K. Mukherjee. Low-temperature superplasticity in nanostructured nickel and metal alloys. *Nature*, 398:684 – 686, 1999. 7
- [51] A. Vinogradov, S. Hashimoto, V. Patlan, and K. Kitagawa. Atomic force microscopic study on surface morphology of ultra-fine grained materials after tensile testing. *Mater. Sci. Eng. A*, 319-321:862, 2001.
- [52] Y. Huang and T.G. Langdon. Using atomic force microscopy to evaluate the development of mesoscopic shear planes in materials processed by severe plastic deformation. *Mater. Sci. Eng. A*, 358:114, 2003.
- [53] R.Z. Valiev, A. Sergueeva, and A.K. Mukherjee. The effect of annealing on tensile deformation behaviour of nanostructured SPD titanium. *Scripta Mater.*, 49:669–674, 2003.
- [54] R. Z. Valiev. Nanostructuring of metals by severe plastic deformation for advanced properties. *Nature Materials*, 3:511–516, 2004. 7, 12
- [55] C.Y. Yu, P.W. Kao, and C.P. Chang. Transition of tensile deformation behaviors in ultrafine-grained aluminum. *Acta Mater.*, 53:4019–4028, 2005.
- [56] Z. Horita, K. Ohashi, T. Fujita, K. Kaneko, and T.G. Langdon. Achieving High Strength and High Ductility in Precipitation-Hardened Alloys. *Adv. Mater.*, 17:1599–1602, 2005. 7
- [57] N.Q. Chinh, P. Szommer, Z. Horita, and T.G. Langdon. Experimental Evidence for Grain-Boundary Sliding in Ultrafine-Grained Aluminum Processed by Severe Plastic Deformation. *Adv. Mater.*, 18:34–39, 2006. 7
- [58] V. Sklenička, J. Dvořák, P. Kral, Z. Stonawska, and M. Svoboda. Creep processes in pure aluminium processed by equal-channel angular pressing. *Mater. Sci. Eng. A*, 410-411:408–412, 2005. 7

-
- [59] H.S. Kim and S.I. Hong. A model of the ductile-brittle transition of partially crystallized amorphous Al-Ni-Y alloys. *Acta Metall.*, 47:2059–2066, 1999. 7
- [60] H.S. Kim, Y. Estrin, and M.B. Bush. A phase mixture model of a particle reinforced composite with fine microstructure. *Mater. Sci. Eng. A*, 276:175–185, 1999.
- [61] H.S. Kim, Y. Estrin, and M.B. Bush. Plastic deformation behaviour of fine-grained materials. *Acta Metall.*, 48:493–504, 2000. 7
- [62] M. F. Ashby and R. A. Verrall. Diffusion-accommodated flow and superplasticity. *Acta Metall.*, 21:149–163, 1973. 8, 68
- [63] O.D. Sherby and J. Wadsworth. Superplasticity—Recent advances and future directions. *Prog. Mater. Sci.*, 33:169–221, 1989. 8, 68
- [64] H.W. Höppel and R.Z. Valiev. On the possibilities to enhance the fatigue properties of ultrafine-grained metals. *Z. Metallkd.*, 93:641–648, July 2002. 8
- [65] R. W. Hayes, D. Witkin, F. Zhou, and E. J. Lavernia. Deformation and activation volumes of cryomilled ultrafine-grained aluminum. *Acta Mater.*, 52:4259–4271, 2004. 8
- [66] Y.J. Li, W. Blum, and F. Breutingger. Does nanocrystalline Cu deform by Coble creep? *Mater. Sci. Eng. A*, 387-389:585–589, 2004. 8
- [67] Y. J. Li and W. Blum. Strain rate sensitivity of Cu after severe plastic deformation by multiple compression. *phys. stat. sol. (a)*, 202(11):R119– R121, 2005. 8
- [68] S.V. Raj and G. Pharr. A compilation and analysis of data for the stress dependence of the subgrain size. *Mater. Sci. Eng.*, 81:217–237, 1986. 12
- [69] W. Blum. High-Temperature Deformation and Creep of Crystalline Solids. In H. Mughrabi, editor, *Plastic Deformation and Fracture of Materials*, volume 6, pages 359–405, Weinheim, 1993. VCH Verlagsgesellschaft. 12, 28, 31, 57, 74, 76
- [70] E. Nes. Modelling work hardening and stress saturation in FCC metals. *Progr. Mater. Sci.*, 41(3):129–193, 1998. 20, 21, 28, 32, 36, 96
- [71] X.H. Zeng and W. Blum. Modelling the Influence of Microstructure on Creep Strength of G-X12CrMoWVNbN. In E. Roos, editor, *29th MPA Seminar, Safety and Reliability in Energy Technology*, volume 2, page 51, Stuttgart, 2003. 12, 74, 76
- [72] X. Molodova, S. Bhaumik, M. Winning, and G. Gottstein. ECAP processed copper during deformation and subsequent annealing. In Z. Horita, editor, *Proc. of 3rd Int. Conf. on Nanomaterials by Severe Plastic Deformation NANOSPD3, Fukuoka, Japan*, Materials Science Forum 503-504, pages 469–474, Uetikon, Switzerland, 2005. Trans Tech Publications. 12

- [73] Y. J. Li, R. Kapoor, J. T. Wang, and W. Blum. Deformation resistance of ultrafine-grained copper at elevated temperature. Poster at TMS annual meeting, San Antonio, USA, 2006. 13
- [74] R. Kapoor, Y.J. Li, J.T. Wang, and W. Blum. Creep transients during stress changes in ultrafine-grained copper. *Scripta mater.*, 54:1803–1807, 2006. 13
- [75] J. Weertman and J.R. Weertman. *Elementary dislocations theory*. Oxford University Press, New York, 2nd edition, 1992. 13
- [76] R.J. Amodeo and N.M. Ghoniem. Dislocation dynamics. I. A proposal methodology for deformation micromechanics. *Phys. Rev. B*, 41:6958–6967, 1990. 13
- [77] R.Z. Valiev, V.Yu. Gertsman, and O.A. Kaibyshev. Grain boundary structure and properties under external influences. *Phys. stat. sol. (a)*, 97:11, 1986. 14
- [78] Huang. J.Y., Y.T. Zhu, H. Jiang, and T.C. Lowe. Microstructures and dislocation configurations in nanostructured Cu processed by repetitive corrugation and straightening. *Acta Metall.*, 49:1497–505, 2001. 14, 31
- [79] Y.T. Zhu, J.Y. Huang, J. Gubicza, T. Ungar, Y.M. Wang, E. Ma, and R.Z. Valiev. Nanostructures in Ti processed by severe plastic deformation. *J. Mater. Res.*, 18:1908, 2003. 14, 31
- [80] M.F. Ashby. *Strengthening Methods in Crystals*, chapter The deformation of plastically non-homogeneous materials, pages 137–190. Elsevier, Amsterdam, 1971. 15, 31
- [81] X. H. Zeng, P. Eisenlohr, and W. Blum. Modelling the transition from hardening to softening by high-angle grain boundaries. *ICSMA 14*, 2006. 18
- [82] F. Roters, D. Raabe, and G. Gottstein. Work hardening in heterogeneous alloys - a microstructural approach based on three internal state variables. *Acta Mater.*, 48(17):4181–4189, 2000. 20, 26, 29, 32
- [83] W. Blum, P. Eisenlohr, and F. Breutinger. Understanding creep – a review. *Metall. Trans.*, 33A:291–303, 2002. 20, 26, 28, 29, 31, 32
- [84] E. Nes, K. Marthinsen, and Y. Brechet. On the mechanisms of dynamic recovery. *Scripta Materialia*, 47:607–611, 2002. 20, 66
- [85] E. Nes and K. Marthinsen. Modeling the evolution in microstructure and properties during plastic deformation of f.c.c.-metals and alloys - an approach towards a unified model. *Mater. Sci. Eng. A*, 322(1-2):176–193, 2002. 20, 21
- [86] U. F. Kocks. In *Proc. of the Conf. at the 50th Anniversary Meeting on Dislocations and Properties of Real Materials*, pages 125–143, London, 1985. The Institute of Metals. 21

-
- [87] U.F. Kocks. Laws for work-hardening and low-temperature creep. *J. Eng. Mater. Tech. (ASME-H)*, 98:76–85, 1976. 26
- [88] U. Essmann and H. Mughrabi. Annihilation of dislocations during tensile and cyclic deformation and limits of dislocation densities. *Phil. Mag.*, 40:731–756, 1979. 26
- [89] J. Weertman. Dislocation Climb Theory of Steady-State Creep. *Trans. ASM*, 61:681–694, 1968. 26
- [90] J. Weertman. High temperature creep produced by dislocation motion. In J. C. M. Li and A. K. Mukherjee, editors, *Rate Processes in Plastic Deformation of Materials*, pages 315–336. American Soc. for Metals, 1975.
- [91] W. D. Nix and B. Ilshner. Mechanisms controlling creep of single phase metals and alloys. In P. Haasen, V. Gerold, and G. Kostorz, editors, *Proc. 5th Int. Conf. on the Strength of Metals and Alloys (ICSMA 5)*, pages 1503–1530, Oxford, 1980. Pergamon Press. 26
- [92] P. Eisenlohr. *On the role of dislocation dipoles in unidirectional deformation of crystals*. Dr.-Ing. thesis, Universität Erlangen-Nürnberg, 2004. 28, 29, 36, 37
- [93] P. Haasen. *Physikalische Metallkunde*. Springer-Verlag, 1974, Berlin, Heidelberg, New York. 28
- [94] F.R.N. Nabarro. Steady-state diffusional creep. *Phil. Mag.*, 16:231–237, 1967. 28
- [95] A.S. Argon and W.C. Moffatt. Climb of extended edge dislocations. *Acta Metall.*, 29(2):293–299, 1981. 29
- [96] A. Seeger. In *Rept. Conf. on Defects in Crystalline Solids*, page 391, London, 1955. Physical Society. 29
- [97] A.J. Ardell, H. Reiss, and W.D. Nix. Statistics of Jogs on Dislocations at Equilibrium. *J. Appl. Phys.*, 36(5):1727–1732, 1965. 29
- [98] F. Roters. *Realisierung eines Mehrebenenkonzeptes in der Plastizitätsmodellierung, Von der Versetzungsdynamik zur Finite-Elemente-Simulation*. Berichte aus der Werkstofftechnik, D 82 (Diss. RWTH Aachen). Shaker Verlag, Aachen, 1999. 29
- [99] E. Orowan. Problems of plastic gliding. *Proc. Phys. Soc.*, 52(1):8–22, 1940. 31
- [100] R. Lagneborg, B.H. Forsén, and J. Wiberg. In *Creep Strength in Steels and High Temperature Alloys*, page 1, London, 1974. Iron and Steel Institute, Metals Society. 31
- [101] R. Gasca-Neri and W.D. Nix. A model for the mobile dislocation density. *Acta Metall.*, 22(3):257–264, 1974.

- [102] F. Roters. A new concept for the calculation of the mobile dislocation density in constitutive models of strain hardening. *phys. stat. sol. (b)*, 240(1):68–74, 2003. 31
- [103] O. D. Sherby and P. M. Burke. Mechanical Behaviour of Crystalline Solids at Elevated Temperature. *Progr. Mater. Sci.*, 13:323–390, 1968. 32
- [104] U. F. Kocks, A. S. Argon, and M. F. Ashby. Thermodynamics and Kinetics of Slip. *Progr. Mater. Sci.*, 19:1–291, 1975. 32, 36
- [105] R. Sedláček and W. Blum. Microstructure-based Constitutive Law of Plastic Deformation. *Comp. Mater. Sci.*, 25(1-2):200–206, 2002. 32
- [106] S.D. Cohen and A.C. Hindmarsh. CVODE, a stiff/nonstiff ODE solver in C. *Computers in Physics*, 10(2):138–143, 1996. 32
- [107] W. Schatt, editor. *Einführung in die Werkstoffwissenschaft*. VEB Deutscher Verlag für Grundstoffindustrie, Leipzig, 6th edition, 1987. 36
- [108] F. Dalla Torre, R. Lapovok, J. Sandlin, P.F. Thomson, C.H.J. Davies, and E.V. Pereloma. Microstructures and properties of copper processed by equal channel angular extrusion for 1-16 passes. *Acta Mater.*, 52:4819–4832, 2004. 37
- [109] H. Mughrabi. Dislocation wall and cell structures and long-range internal stresses in deformed metal crystals. *Acta Metall.*, 31(9):1367–1379, 1983. 62
- [110] Blum W. *Gleitung und Erholung während plastischer Verformung kristalliner Stoffe bei hoher Temperatur*. Habilitationsschrift, Universität Erlangen-Nürnberg, 1978. 63
- [111] E. Nes, T. Pettersen, and K. Marthinsen. On the mechanisms of work hardening and flow-stress saturation. *Scripta Mater.*, 43(1):55–62, 2000. 63, 65
- [112] R.L. Coble. A Model for Boundary Diffusion Controlled Creep in Polycrystalline Materials. *J. Appl. Phys.*, 34:1679, 1963. 68
- [113] W.G. Johnston and J.J Gilman. Dislocation velocities, dislocation densities, and plastic flow in lithium fluoride crystals. *J. Appl. Phys.*, 30(2):129–144, 1959. 71
- [114] E. Arzt, M.F. Ashby, and R.A. Verrall. Interface controlled diffusional creep. *Acta Metall.*, 31:1977–1989, 1983. 101, 102

A Appendix

A.1 Average radius of grain sections

The grains are assumed to be spheres with a radius of r . Consider a cross section through P parallel to plane XOY (Fig. A.1(a)). The average area \bar{A} of the cross sections parallel to plane XOY reads

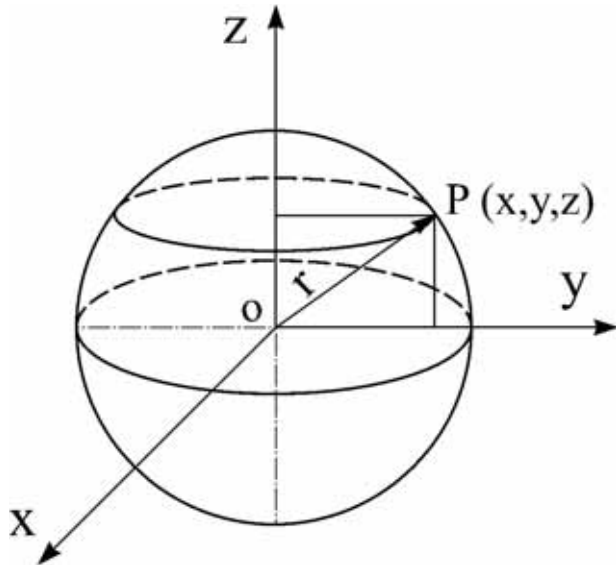
$$\begin{aligned}
 \bar{A} &= \frac{1}{r} \int_0^r \pi y^2 dz \\
 &= \frac{1}{r} \int_r^0 \pi y^2 d\sqrt{r^2 - y^2}, \quad \text{with } z = \sqrt{r^2 - y^2} \\
 &= \frac{1}{r} \int_r^0 -\frac{\pi y^3}{\sqrt{r^2 - y^2}} dy \\
 &= \frac{2\pi}{3} r^2.
 \end{aligned} \tag{A.1}$$

The radius of the average cross section r' equals $\sqrt{\bar{A}/\pi}$. Thus

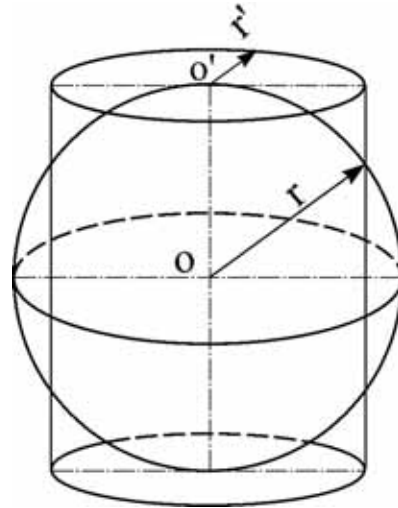
$$r = \sqrt{\frac{3}{2}} r'. \tag{A.2}$$

The relation between r' and the grain size d measured by line intersection (Heyn's size) is given by $2r'd = \pi r'^2$ (see Fig. A.1(c)), namely,

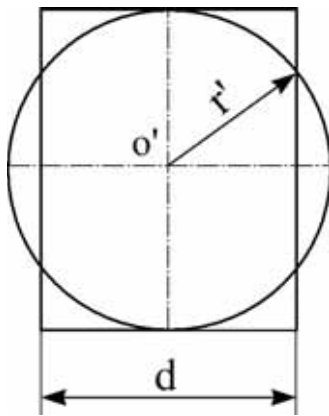
$$r' = \frac{2}{\pi} d. \tag{A.3}$$



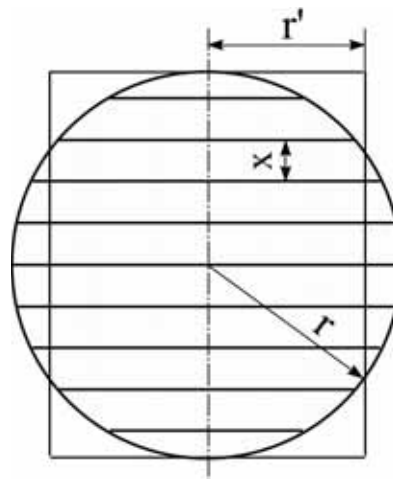
(a) Idealized grains being spheres with a radius of r .



(b) Determination of the average grain section by equating the volumes of the sphere and the cylinder with $\pi r'^2$ in cross section and $2r$ in height.



(c) Determination of the average grain size by equating the areas of the average grain section and the rectangle with d and $2r'$ in width and height, respectively.



(d) Two-dimension view of (b). Horizontal thick lines: slip planes; X : the spacing between slip planes.

Figure A.1: Geometrical relationship between average radius of grain sections r' and the measured grain size d .

A.2 Generation rate of dislocations in grain interiors

Nes [70] considers there are dN_m small loops generated per volume in the shear strain interval $d\gamma$, an increasing fraction of the loops is getting immobilized according to a certain probability p (for a dislocation loop expanding on its slip plane to be stored per dislocation encountered), as the radius r of the loops increases. It is assumed that the loop fraction dN/dN_m has been immobilized by reaction with other dislocations while the loop radius was growing to r so that only $dN_m - dN$ mobile loops are remaining to be further expanding. If r grows further by dr , the area $2\pi r dr$ is slipped and the volume density of mobile loops further decreases by the fraction:

$$\frac{d^2 N}{dN_m - dN} = -d \ln (dN_m - dN) = p \cdot \rho \cdot 2\pi r dr = p \cdot \rho \cdot \pi dr^2. \quad (\text{A.4})$$

Integration yields the increase of volume density dN of stored loops in the interval $d\Delta\gamma$:

$$\int_0^{dN(r)} \frac{d^2 N}{dN_m - dN} = \int_0^{dN(r)} -d \ln (dN_m - dN) = \int_0^r p \cdot \rho \cdot 2\pi r dr = p \cdot \rho \cdot \pi dr^2, \quad (\text{A.5})$$

namely,

$$dN(r) = dN_m (1 - \exp(-p\rho\pi r^2)). \quad (\text{A.6})$$

Eq. (A.6) was originally derived by [70]. Based on this equation, the storage rate of dislocations in a confined volume may be derived.

Consider a grain with size d (measured by line intersection), the fraction of loops which is stored in the grain interior is $dN(r')/dN_m$, where $dN(r')$ is the number of the stored loops per volume; and r' is the average radius of grain sections which is proportional to the grain size d (see Appendix A.1). The average radius \bar{r} of the $dN(r')$ loops stored in the grain interior reads

$$\bar{r} = \frac{1}{dN(r')} \int_0^{dN(r')} r d^2 N. \quad (\text{A.7})$$

Inserting Eq. (A.6) into Eq. (A.7) leads to

$$\begin{aligned} \bar{r} &= p\rho\pi \frac{dN_m}{dN(r')} \int_0^{r'} (r^2)^{\frac{1}{2}} \exp(-p\rho\pi r^2) dr^2 \\ &= \frac{0.5 (p\rho)^{-0.5} \operatorname{erf}(\sqrt{p\rho\pi} r') - r' \exp(-p\rho\pi r'^2)}{1 - \exp(-p\rho\pi r'^2)}. \end{aligned} \quad (\text{A.8})$$

In the limiting case of $r' \rightarrow \infty$, \bar{r} approaches $0.5 (p\rho)^{-0.5}$ which is the mean free path of dislocations of density ρ [70].

The remaining fraction of loops which reaches the grain boundaries is $1 - dN(r')/dN_m$. The shear strain increment $d\gamma$ connected to $dN(r')$ loops stored in the grain interiors and $dN_m - dN(r')$ loops stored in the grain boundaries per unit volume is thus given:

$$d\gamma = b dN(r') A(\bar{r}) + b (dN_m - dN(r')) A(r'), \quad (\text{A.9})$$

where $A(\bar{r}) = \pi \bar{r}^2$ and $A(r') = \pi r'^2$ are the average slipped area of each loop stored in the grain interior and boundary, respectively. Inserting Eq. (A.6) into (A.9) yields

$$\frac{d\gamma}{dN_m} = b \pi \left(\bar{r}^2 + (r'^2 - \bar{r}^2) \exp(-p \rho \pi r'^2) \right). \quad (\text{A.10})$$

The increase in dislocation density within the grain of radius r' in an interval $d\gamma$ at the shear strain γ is directly proportional to the increase of number of dislocation loops stored in the grain interiors generated in $d\gamma$:

$$d\rho = 2 \pi \bar{r} dN(r'). \quad (\text{A.11})$$

Combining Eqs. (A.10)-(A.11) one gets:

$$\frac{d\rho}{d\gamma} = \frac{2 \bar{r} \left(1 - \exp(-p \rho \pi r'^2) \right)}{b \left(\bar{r}^2 + (r'^2 - \bar{r}^2) \exp(-p \rho \pi r'^2) \right)} \quad (\text{A.12})$$

A.3 Storage rate of dislocations at grain boundaries

The rate equation will be derived through three different approaches in terms of the choices of the grain geometries. The intention is to check whether the rate equation to be derived is sensitive to the choice of grain geometry.

Approach I According to Fig. A.1(a), consider a cross section through P parallel to plane XOY , the specific dislocation length (length per slipped area), which is stored at the grain boundary, is:

$$\frac{1}{\Lambda_P} = \frac{2\pi y}{\pi y^2}. \quad (\text{A.13})$$

It is seen that $1/\Lambda_P$ varies with the location of the cross section. Its average value is:

$$\begin{aligned} \frac{1}{\Lambda'_P} &= \frac{1}{r} \int_0^r \frac{1}{\Lambda_P} dz = \frac{1}{r} \int_0^r \frac{2\pi y}{\pi y^2} dz \\ &= \frac{1}{r} \int_r^0 \frac{2\pi y}{\pi y^2} d\sqrt{r^2 - y^2}, \quad \text{with } z = \sqrt{r^2 - y^2} \\ &= \frac{1}{r} \int_r^0 -\frac{2}{\sqrt{r^2 - y^2}} dy \\ &= \frac{\pi}{r}. \end{aligned} \quad (\text{A.14})$$

Combining Eqs. (A.14) and (A.3) leads to:

$$\frac{1}{\Lambda'_P} = \frac{\pi^2}{\sqrt{6}} \frac{1}{d}. \quad (\text{A.15})$$

The average dislocation density ρ_{gb} can be derived as:

$$\rho_{\text{gb}} = \frac{\text{dislocation length}}{\text{slipped area}} \cdot \frac{\text{slipped area}}{\text{volume}}. \quad (\text{A.16})$$

The ratio of slipped area/volume equals $\frac{1}{2} \frac{2\pi r'}{2\pi r' x} = \frac{1}{2x}$, where r' is the average radius of the grain sections (see Fig. A.1 and Eq. (A.2)). The factor of 1/2 means that only half of the grain boundary (consisting of two grain surfaces) must be counted. x is the mean spacing between the slip planes (see Fig. A.1(d)). A relative displacement by b along slip planes at spacing x causes a crystal to shear by

$$\gamma = \frac{b}{x}. \quad (\text{A.17})$$

Inserting the ratio given above into (A.16) and combining (A.17) yield

$$\rho_{\text{gb}} = \frac{1}{b k_{\text{gb}} d} \cdot \gamma \quad (\text{A.18})$$

with $k_{\text{gb}} \doteq 0.5$. Differentiating both sides of Eq. (A.18) leads to the storage rate of grain boundary dislocations of one glide system

$$\dot{\rho}_{\text{gb}}^+ = \frac{1}{b k_{\text{gb}} d} \cdot \dot{\gamma}. \quad (\text{A.19})$$

Approach II The ratio of the average length of dislocations to the surface area of the sphere is $\frac{2\pi r'}{4\pi r'^2} = \frac{r'}{2r'^2}$, where r' is the average radius of the slip planes (see Fig. A.1(d)). According to the definition of areal density N_{gb} (length per area), consider there are $2r/x$ slip planes (see Fig. A.1(d)), N_{gb} reads,

$$N_{\text{gb}} = \frac{r'}{2r'^2} \cdot \frac{2r}{x} = \frac{r'}{r} \cdot \frac{2}{x}. \quad (\text{A.20})$$

Combining (A.2), (A.17) and (A.21) leads to

$$N_{\text{gb}} = \sqrt{\frac{2}{3}} \frac{1}{b} \cdot \dot{\gamma}. \quad (\text{A.21})$$

Combining (A.21) and (2.4) yields the expression of the storage rate of dislocation length per volume $\dot{\rho}_{\text{gb}}^+$ of

$$\dot{\rho}_{\text{gb}}^+ = \dot{N}_{\text{gb}}^+ \cdot \frac{2}{d} = \frac{1}{b k_{\text{gb}} d} \cdot \dot{\gamma} \quad (\text{A.22})$$

with $k_{\text{gb}} \doteq 0.6$.

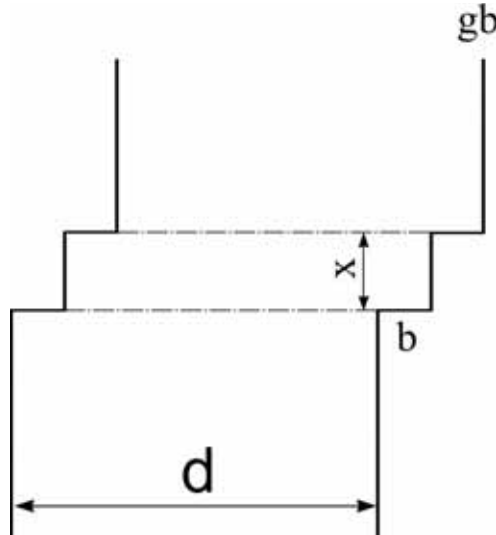


Figure A.2: Storage of dislocations at grain boundaries in one grain in 1-Dimension schematic. X : the spacing between the slip planes; gb: grain boundary being perpendicular to the paper.

Approach III In the one dimension model proposed in [5], it is assumed that grain boundaries are infinite planes in parallel separated by the grain size of d (Fig. A.2). Suppose the length of a dislocation lying in the grain boundary is L , then the area between two dislocation lines is Lx where x is the spacing between dislocation lines. Consider there are two dislocations coming from neighboring grains, the areal density N_{gb} reads

$$N_{\text{gb}} = 2 \frac{L}{Lx} = \frac{2}{x}. \quad (\text{A.23})$$

Combining (A.17) leads to

$$N_{\text{gb}} = \frac{2}{b} \gamma. \quad (\text{A.24})$$

The area of grain boundary per volume in the one dimension model is $1/d$. The storage rate of dislocation length per volume $\dot{\rho}_{\text{gb}}^+$ in the one dimension case can be expressed as

$$\dot{\rho}_{\text{gb}}^+ = \dot{N}_{\text{gb}}^+ \cdot \frac{1}{d} = \frac{1}{bk_{\text{gb}}d} \cdot \dot{\gamma} \quad (\text{A.25})$$

with $k_{\text{gb}} \doteq 0.5$.

By comparing Eqs. (A.19), (A.22) and (A.25) it is concluded that no significant difference was found in the rate equations derived through the three approaches.

A.4 Climb velocity of grain boundary dislocations

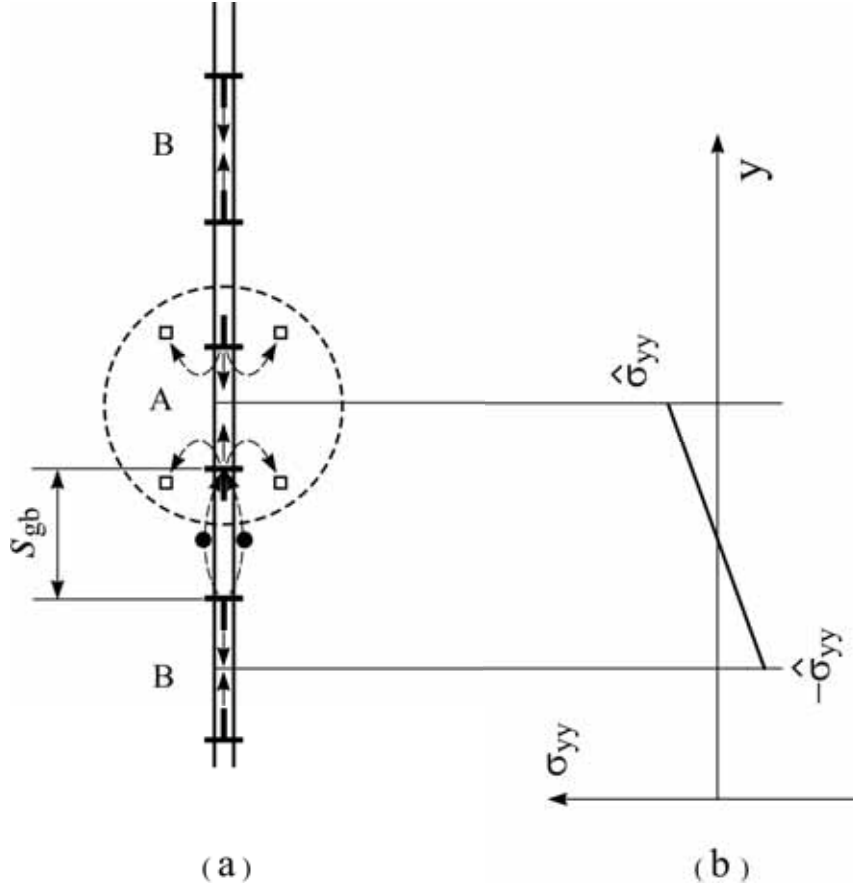


Figure A.3: Configuration of (a) dislocation dipoles (marked by A and B) and (b) the normal stress σ_{yy} in the center of the dipole at the grain boundary.

The grain boundaries contain an array of dislocation dipoles of opposite signs. When the constituents of dipole A (see Fig. A.3(a)) climb towards each other due to mutual attractive force, they need atoms or emit vacancies. On the contrary, dipole B emits atoms or absorbs vacancies when its constituents climb. If we assume that the core of a dislocation is a perfect source or sink for vacancies, grain boundary diffusion thus plays an essential role in annihilation of dipoles by transporting atoms from dipole B to dipole A. In addition, emission of vacancies (by dipole A) to the lattice and absorption of vacancies (by dipole B) from the lattice also contribute to dislocation climb. The climb velocity of dislocations of dipole A/B $v_{c,gb}$ is determined by the diffusion flux of atoms (atoms/second) arriving at/leaving the dislocation's core J_a [114] and by the diffusion flux of vacancies (vacancies/second) leaving/arriving at its core J_v [27]. Then

$$v_{c,gb} = \frac{b}{1/(J_a + J_v)}. \quad (\text{A.26})$$

The diffusion flux of atoms or vacancies J is the product of the flux of atoms/vacancies/area per (atoms or vacancies/second/area) j and the diffusion area A .

$$J = j \cdot A. \quad (\text{A.27})$$

Diffusion flux of atoms J_a From the first Fick's law the flux of atoms j_a reads

$$j_a = -\frac{1}{\Omega} \frac{D_{gb}}{k_B T} \nabla \mu, \quad (\text{A.28})$$

where $\nabla \mu$ is the gradient of chemical potential of vacancies. The assumption of the core of a dislocation being a perfect source or sink of vacancies implies that the chemical potential of vacancies in the immediate vicinity of a dislocation is that which is in equilibrium with the core of a straight dislocation, acted on by the local stress σ_1 [114]:

$$\mu - \mu_v = \mu_0 - \sigma_1 \Omega, \quad (\text{A.29})$$

where μ_v is the chemical potential of vacancies and μ_0 that of vacancies in a standard, stress-free crystals. It is the gradients of $\mu - \mu_v$ which drive the diffusive flux of vacancies. Thus one gets

$$\nabla \mu = -\nabla \sigma_1 \Omega. \quad (\text{A.30})$$

The stress gradient $\nabla \sigma_1$ can be derived from the normal stresses perpendicular to y -axis at annihilation sites of the dipoles. The middle points between dipole A and B correspond to the sites where the dipoles annihilate. The stresses at these sites are represented by a tensile stress $\hat{\sigma}_1$ for dipole A and a compressive stress $-\hat{\sigma}_1$ (see Fig. A.3(b)). Consider the limit case where the climb velocity is described by minimum stress gradient which is determined by minimum stresses at the annihilation sites and maximum spacings between the two annihilation sites. One may approximately linearize the stress gradient by

$$\nabla \sigma_1 = \frac{2 \hat{\sigma}_1}{2 s_{gb}}. \quad (\text{A.31})$$

The stress $\hat{\sigma}_1$ is described by superimposing stresses caused by each dislocations in the array as shown in Fig. A.3(b):

$$\hat{\sigma}_1 = 2 \frac{G b}{2 \pi (1 - \nu)} \frac{1}{0.5 s_{gb}} + 2 \frac{G b}{2 \pi (1 - \nu)} \frac{1}{1.5 s_{gb}} - 2 \frac{G b}{2 \pi (1 - \nu)} \frac{1}{2.5 s_{gb}} + \dots \quad (\text{A.32})$$

The factor 2 before the fractions is appropriate as the dislocations are mirrored about the annihilation site. The number of the terms is determined by $d/(2 s_{gb})$. As the dislocations in the array alternatively change their signs, the terms in Eq. (A.32) alternatively change their sign accordingly. A minimum stress can be obtained by remaining only the first term and eliminating the rest terms of Eq. (A.32). When there are five terms in the series, this approximation will cause an error less than 20%.

The cross section A of diffusion flux (per atom's width) through the boundary reads

$$A = \delta_{gb} b. \quad (\text{A.33})$$

Combining Eqs. (A.27) to (A.33) and taking into account the approximation in local stress (Eq. A.32), one gets yields

$$J_a = \frac{2}{\pi(1-\nu)} \frac{G\Omega}{b k_B T} \delta_{gb} D_b \frac{1}{s_{gb}^2}. \quad (\text{A.34})$$

Diffusion flux of vacancies J_v According to the first Fick's law the flux of vacancies j_v reads

$$j_v = -D_v \nabla C, \quad (\text{A.35})$$

where D_v is diffusion coefficient of vacancies in the lattice, C is concentration of vacancies (vacancies/volume). The local equilibrium concentration of vacancies near the dislocation reads [27]

$$C = C_0 \exp\left(\frac{\sigma_{c,gb} \Omega}{k_B T}\right), \quad (\text{A.36})$$

where $\sigma_{c,gb}$ (see Eq. A.37) is the mutual attractive stress between the dipole constituents [27] of dislocations of average $(d_{dip,gb} + d_{spon,gb})/2$ apart:

$$\sigma_{c,gb} = \frac{G b}{2\pi(1-\nu)} \frac{1}{(d_{dip,gb} + d_{spon,gb})/2}, \quad (\text{A.37})$$

which is treated identical to an equally wide dipole formed by interior dislocations. Taking into account that the stress field of grain boundary dislocations will relax, the climb stress is somewhat overestimated.

Consider a dipole locating in the center of a cylinder with a radius R as marked by the circle in Fig. A.3. Both dislocations tend to establish the same vacancy concentration near their cores. For a cylinder with a radius r the cross section for vacancy flux (per atom's width) reads,

$$A = 2\pi r b \quad \text{with} \quad r_c \leq r \leq R, \quad (\text{A.38})$$

where $r_c \approx b$ is the radius of the dislocation core. According to Eqs. (A.28) and (A.27) one can obtain the diffusion flux of vacancies J_v . In steady state of diffusion of vacancies J_v becomes constant, thus

$$J_v = j \cdot 2\pi r b = -2\pi b D_v \frac{r dC}{dr} = const. \quad (\text{A.39})$$

By integrating the concentration C ,

$$\int_{C(r)}^{C_0} dC = -\frac{const}{2\pi b D_v} \int_r^R \frac{r}{dr}, \quad (\text{A.40})$$

one gets the concentration of vacancies at radius r of each dipole constituent $C(r)$,

$$C_0 - C(r) = -\frac{const}{2\pi b D_v} \ln\left(\frac{R}{r}\right), \quad (\text{A.41})$$

By superposition, the two terms of Eq. (A.41) for each dipole constituent give the vacancy distribution with both dislocations present. At $r = r_c$, namely, in the vicinity of each dislocation core, one gets,

$$C_0 - C(r_c) = -\frac{const}{2\pi b D_v} \left[\ln\left(\frac{R}{b}\right) + \ln\left(\frac{R}{s_{gb}}\right) \right], \quad (\text{A.42})$$

To determine *const*, one may combine Eqs. (A.36) and (A.42) and replace r_c with b , thus

$$const = C_0 \left[\exp\left(\frac{\sigma_{c,gb}\Omega}{k_B T}\right) - 1 \right] 2\pi b D_v / \ln\left(\frac{R^2}{b s_{gb}}\right). \quad (\text{A.43})$$

Inserting *const* into Eq. (A.41) yields

$$C(r) = C_0 + C_0 \left[\exp\left(\frac{\sigma_{c,gb}\Omega}{k_B T}\right) - 1 \right] \frac{\ln(R/r)}{\ln[R^2/(b s_{gb})]}. \quad (\text{A.44})$$

Now the gradient ∇C of concentration of vacancies can be determined:

$$\nabla C = \frac{1}{r} C_0 \left[\exp\left(\frac{\sigma_{c,gb}\Omega}{k_B T}\right) - 1 \right] \frac{1}{\ln[R^2/(b s_{gb})]}. \quad (\text{A.45})$$

Combining Eqs. (A.35), (A.39) and (A.45) yields

$$J_v = D_v c_0 b \left[\exp\left(\frac{\sigma_{c,gb}\Omega}{k_B T}\right) - 1 \right] \frac{2\pi}{\ln[R^2/(b s_{gb})]}. \quad (\text{A.46})$$

Invoking the definition of the atomic self-diffusion coefficient D_{sd} [27]

$$D_{sd} = \Omega c_0 D_v, \quad (\text{A.47})$$

and combining Eq. (A.46) yields

$$J_v = \frac{D_{sd}}{b^2} \left[\exp\left(\frac{\sigma_{c,gb}\Omega}{k_B T}\right) - 1 \right] \frac{2\pi}{\ln[R^2/(b s_{gb})]}. \quad (\text{A.48})$$

Acknowledgments

I would like to thank all of the colleagues and friends in the *Department of Materials Science and Engineering, Institute I: General Materials Properties WWI, University of Erlangen-Nürnberg* for their help during my doctoral work.

Especially I wish to thank to

- Prof. Dr. W. Blum, who has kindly agreed to supervise my work, for his patience, critical encouragements and valuable advises, which are necessary to my doctoral work.
- Prof. A. Hartmaier for helpful discussions.
- Profs. M. Göken and H. Mughrabi for their kind hospitality.
- Dr. P. Eisenlohr for many intensive discussions and valuable suggestions.
- My colleagues and friends: P. Sadrabadi, S. Mekala, H. Chilukuru, and Y. J. Li for their helps and cooperation during my work; and J. Müller for his help in translation into English.
- Dr. P. Eisenlohr, Dr. W. H. Höppel and Mr. R. Nützel for dealing with my computer problems.
- Frau. Graham, secretary of the institute for very timely help. Many thanks to everybody whoever gave me help and support in the institute.
- My former directors, colleagues and friends, especially Profs. J. T. Wang, W.L. Tang, S.J. Zhao and X. R. Yang from *Xi'an University of Architecture & Technology*, for their generous helps and supports.
- My parents, my sisters and my brother, for their love and encouragement.
- my wife Y. J. Li and my daughter Y. Zeng for their love, support, and understanding in dealing with all the challenges I have faced.

Curriculum vitae

Personal

Name	Xiaohui Zeng
Date of Birth	Sep 17, 1970
Place of Birth	Shaanxi, China
Nationality	P.R. China

Education

1978 – 1983	Elementary school, Shaanxi
1986 – 1989	Secondary school, Shaanxi
1986 – 1989	Fengxiang Gymnasium, Shaanxi
May 1989	Abitur

University Education

1989 – 1993	Xi'an Institute of Metallurgy & Construction Engineering, Xi'an, China
Jul. 1993	Bachelor
1993 – 1996	Xi'an University of Architecture & Technology, Xi'an, China
Apr. 1996	Master

Work Experience

1996 – 2002	Lecture, Xi'an University of Architecture & Technology, Xi'an, China
Dec. 2002 – Oct. 2006	Research Associate, University of Erlangen-Nürnberg, Erlan- gen, Germany

